



MINISTÉRIO DA CIÊNCIA, TECNOLOGIA, INOVAÇÕES E COMUNICAÇÕES  
**INSTITUTO NACIONAL DE PESQUISAS ESPACIAIS**

sid.inpe.br/mtc-m21b/2016/12.24.01.22-TDI

**ON THE INFLUENCE OF NONLOCAL HEAT FLUX ON  
ENERGY TRANSPORT AND BALANCE IN THE  
SOLAR ATMOSPHERE. (SOBRE A INFLUÊNCIA DO  
FLUXO DE CALOR NÃO LOCAL SOBRE O  
TRANSPORTE E BALANÇO DE ENERGIA NA  
ATMOSFERA SOLAR)**

Suzana de Souza e Almeida Silva

Doctorate Thesis of the Graduate  
Course in Space Geophysics,  
guided by Drs. Maria Virginia  
Alves, Jean Carlo Santos, and Jörg  
Artur Erick Büchner, approved in  
January 24, 2017.

URL of the original document:

<<http://urlib.net/8JMKD3MGP3W34P/3N3M6F8>>

INPE  
São José dos Campos  
2017

**PUBLISHED BY:**

Instituto Nacional de Pesquisas Espaciais - INPE

Gabinete do Diretor (GB)

Serviço de Informação e Documentação (SID)

Caixa Postal 515 - CEP 12.245-970

São José dos Campos - SP - Brasil

Tel.:(012) 3208-6923/6921

Fax: (012) 3208-6919

E-mail: pubtc@inpe.br

**COMMISSION OF BOARD OF PUBLISHING AND PRESERVATION  
OF INPE INTELLECTUAL PRODUCTION (DE/DIR-544):****Chairperson:**

Maria do Carmo de Andrade Nono - Conselho de Pós-Graduação (CPG)

**Members:**

Dr. Plínio Carlos Alvalá - Centro de Ciência do Sistema Terrestre (CST)

Dr. André de Castro Milone - Coordenação de Ciências Espaciais e Atmosféricas (CEA)

Dra. Carina de Barros Melo - Coordenação de Laboratórios Associados (CTE)

Dr. Evandro Marconi Rocco - Coordenação de Engenharia e Tecnologia Espacial (ETE)

Dr. Hermann Johann Heinrich Kux - Coordenação de Observação da Terra (OBT)

Dr. Marley Cavalcante de Lima Moscati - Centro de Previsão de Tempo e Estudos Climáticos (CPT)

Silvia Castro Marcelino - Serviço de Informação e Documentação (SID) **DIGITAL**

**LIBRARY:**

Dr. Gerald Jean Francis Banon

Clayton Martins Pereira - Serviço de Informação e Documentação (SID)

**DOCUMENT REVIEW:**

Simone Angélica Del Ducca Barbedo - Serviço de Informação e Documentação (SID)

Yolanda Ribeiro da Silva Souza - Serviço de Informação e Documentação (SID)

**ELECTRONIC EDITING:**

Marcelo de Castro Pazos - Serviço de Informação e Documentação (SID)

André Luis Dias Fernandes - Serviço de Informação e Documentação (SID)



MINISTÉRIO DA CIÊNCIA, TECNOLOGIA, INOVAÇÕES E COMUNICAÇÕES  
**INSTITUTO NACIONAL DE PESQUISAS ESPACIAIS**

sid.inpe.br/mtc-m21b/2016/12.24.01.22-TDI

**ON THE INFLUENCE OF NONLOCAL HEAT FLUX ON  
ENERGY TRANSPORT AND BALANCE IN THE  
SOLAR ATMOSPHERE. (SOBRE A INFLUÊNCIA DO  
FLUXO DE CALOR NÃO LOCAL SOBRE O  
TRANSPORTE E BALANÇO DE ENERGIA NA  
ATMOSFERA SOLAR)**

Suzana de Souza e Almeida Silva

Doctorate Thesis of the Graduate  
Course in Space Geophysics,  
guided by Drs. Maria Virginia  
Alves, Jean Carlo Santos, and Jörg  
Artur Erick Büchner, approved in  
January 24, 2017.

URL of the original document:

<<http://urlib.net/8JMKD3MGP3W34P/3N3M6F8>>

INPE  
São José dos Campos  
2017

## Cataloging in Publication Data

---

Si38i Silva, Suzana de Souza e Almeida.  
On the influence of nonlocal heat flux on energy transport and balance in the solar atmosphere. (sobre a influência do fluxo de calor não local sobre o transporte e balanço de energia na atmosfera solar) / Suzana de Souza e Almeida Silva. – São José dos Campos : INPE, 2017.  
xviii + 85 p. ; (sid.inpe.br/mtc-m21b/2016/12.24.01.22-TDI)

Thesis (Doctorate in Space Geophysics) – Instituto Nacional de Pesquisas Espaciais, São José dos Campos, 2017.

Guiding : Drs. Maria Virginia Alves, Jean Carlo Santos, and Jörg Artur Erick Büchner.

1. Solar corona. 2. Heat flux. 3. Heat transfer. 4. Plasma heating. 5. Magnetohydrodynamics. I.Title.

CDU 523.947:536.24

---



Esta obra foi licenciada sob uma Licença [Creative Commons Atribuição-NãoComercial 3.0 Não Adaptada](#).

This work is licensed under a [Creative Commons Attribution-NonCommercial 3.0 Unported License](#).



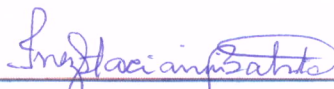
Aluno (a): *Suzana de Souza e Almeida Silva*

Título: " ON THE INFLUENCE OF NONLOCAL HEAT FLUX ON ENERGY TRANSPORT AND BALANCE IN THE SOLAR ATMOSPHERE. (SOBRE A INFLUÊNCIA DO FLUXO DE CALOR NÃO LOCAL SOBRE O TRANSPORTE E BALANÇO DE ENERGIA NA ATMOSFERA SOLAR)".

Aprovado (a) pela Banca Examinadora em cumprimento ao requisito exigido para obtenção do Título de *Doutor(a)* em

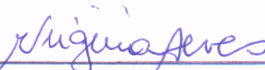
*Geofísica Espacial/Ciências do Ambiente Solar-Terrestre*

Dra. Inez Staciari Batista



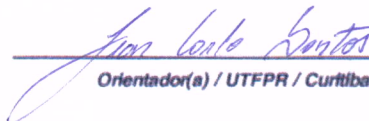
Presidente / INPE / SJCampos - SP

Dra. Maria Virginia Alves



Orientador(a) / INPE / SJCampos - SP

Dr. Jean Carlo Santos

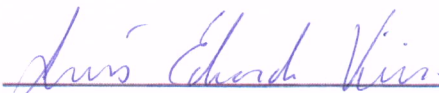


Orientador(a) / UTFPR / Curitiba - PR

Dr. Jörg Artur Erick Büchner

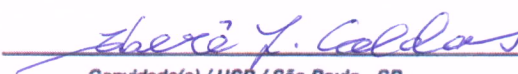
Orientador(a) / MAX Planck / Alemanha - DE

Dr. Luis Eduardo Antunes Vieira



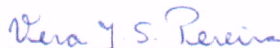
Membro da Banca / INPE / São José dos Campos - SP

Dr. Iberê Luiz Caldas



Convidado(a) / USP / São Paulo - SP

Dra. Vera Jatenco Silva Pereira



Convidado(a) / IAG/USP / São Paulo - SP

Este trabalho foi aprovado por:

( ) maioria simples

(x) unanimidade

São José dos Campos, 24 de Janeiro de 2017



## ACKNOWLEDGEMENTS

First, I would like to thank God for this incredible opportunity to be a scientist. There is nothing like to live to investigate and discover new things!

I am grateful for all the love and support I have received from my family. My mother Sylene, thank you for always believing in me and for showing me the pleasures of reading, studying and having discipline in life. Thank you for doing everything in your reach to give me the best education and opportunities. To my father Daniel, I am grateful for your financial help through college and graduate studies and for your example on how much hard work and dedication can change someone's future. My siblings, Danilo and Adriana, thank you for your friendship and presence in my life. I am grateful for my grandparents Sylvio and Maria Elisa. My late grandfather Sylvio incentivated my scientific curiosity during my childhood and my grandmother Maria Elisa has never failed to put a smile on my face. I admire and love all my family very much!

A deeply thank you goes to CAPES funding, which has allowed me to dedicate myself fully to this work. I am especially grateful for the funding to experience one year of research abroad which has improved my skills as a scientist and was essential to my research project. I am grateful to INPE and MPS for receiving me as Ph. D. student. Those two institutes have made a considerable change in my formation. A special mention to Dr. Sonja Schuh, for the amazing opportunity of being part of IMPRS. I am also thankful to MPG and CESUP for letting me use their computational resources, the HYDRA and GAUSS clusters, respectively.

To my supervisors, Prof. Dr. Virginia Alves, Dr Jean C. Santos and Prof. Dr. Jörg Büchner, I am thankful for your belief in my capacity and for the opportunity to carry out this work. Thank you also for ensuring good opportunities during my Ph.D. and for giving me access to the physical structure necessary for the development of my research.

I am grateful for have had the opportunity to learn from my college professors, Dr. Clovis Maia, Dr. Leonardo Ferreira, Dr. Marcos Maia and Dr. Vanessa Carvalho, during my undergraduate and master studies. Their support was essential for my scientific development and career.

A special thanks to all my dear friends for our conversations over life and/or science. You made life funnier even when the deadlines are just around the corner. Germany

would be a cold place without all the coffee and conversations I have enjoyed with my friends Borys, Iulia, Kinga, and Ricardo! I am also thankful to my other colleagues at MPS for their friendship and discussions, specially Ankit, Fátima, Kok Leng, Patricio and Patrick. To my colleagues at INPE, thank you for all the discussions during the classes. I would like to thank my friends Manuel, Manilo, Régia and Siomel for all the movies and barbecues in our free time which helped me to relax and enjoy life. I am grateful for all the funny and profound moments with my friends Carol, Clarissa, Diego, Hellen, Karina, Leila, Mary and Mayara (in person or over the phone), you were always an essential part of my life.

I would like to thank the support of my dogs, Jessie, Mel and Lua. Their companionship has brought me smiles even after a long and hard day of work. And I am sorry for not being able to spend as much time with them as they deserved!

For last, I would like to thank Luiz for always be there for me. You are my best friend and partner in life and love. Thank you for all of our time together, for all the talks, movies and tours in parks and cities! Your support was essential to get through the difficult moments in my research. I love and admire you deeply.

## ABSTRACT

In the solar corona, heat flux is one of the key processes of energy transport. Since the coronal plasma can be described as weakly collisional, classical formulation for the heat flux might no longer be the most accurate description. In a medium with fewer collisions, the heat flux will have contributions not only from neighboring particles, but also from particles coming from other regions along the magnetic field line. Hence, a better description of the heat flux in this context might be offered by a nonlocal formulation. We have implemented a non local heat flux in a 3D MHD model and we investigated its effects on the thermal evolution of the system. We simulate the evolution of plasma and magnetic field using this model and considering two different formulations for heat flux: classical (local) and nonlocal one. The initial magnetic field was obtained from a potential extrapolation of the observed line-of-sight component of photospheric magnetic field for AR11226. We evolved the system by imposing a field velocity at the bottom of the simulation box which shifted footpoints of the magnetic field lines. Then we compared the differences in the evolution of plasma obtained using the two different formulations for the heat flux. The inclusion of a nonlocal formulation for heat flux leads to considerable differences in the average temperature profile of the lower atmosphere and transition region compared to classical formulation. There are also remarkable differences concerning the contributions from energy transport and from source terms to the temperature depending on the formulation used. Our results suggest that a different heat flux formulation affects considerably the heating dynamics and temperature evolution of the plasma.

Keywords: Solar corona. heat flux. heat transfer. plasma heating. magnetohydrodynamics. simulation.



# **SOBRE A INFLUÊNCIA DO FLUXO DE CALOR NÃO-LOCAL SOBRE O TRANSPORTE E BALANÇO DE ENERGIA NA ATMOSFERA SOLAR**

## **RESUMO**

Na coroa solar, o fluxo de calor é um dos principais processos de transporte de energia. Uma vez que o plasma coronal pode ser descrito como fracamente colisional, a formulação clássica para o fluxo de calor pode não ser a descrição mais precisa. Em um meio com menos colisões, o fluxo de calor terá contribuições não apenas de partículas vizinhas, mas também de partículas provenientes de outras regiões ao longo da linha de campo magnético. Assim, uma melhor descrição do fluxo de calor neste contexto pode ser oferecida por uma formulação não-local. Implementamos um fluxo de calor não-local em um modelo 3D MHD e investigamos seus efeitos na evolução térmica do sistema. Nós simulamos a evolução do plasma e campo magnético usando esse modelo considerando as seguintes formulações para o fluxo de calor: clássico (local) e não-local. O campo magnético inicial foi obtido a partir de uma extrapolação potencial da componente observada da linha de visada do campo magnético fotosférico para AR11226. Nós evoluímos o sistema impondo deslocamento dos *footpoints* das linhas de campo magnético. Ao final, comparamos as diferenças na evolução do plasma obtido utilizando as distintas formulações para o fluxo de calor. A inclusão de uma formulação não-local para o fluxo de calor conduz a diferenças consideráveis no perfil de temperatura média da atmosfera inferior e da região de transição em comparação com a formulação clássica. Há também diferenças notáveis quanto às contribuições do transporte de energia e dos termos de origem para a temperatura dependendo da formulação utilizada. Nossos resultados sugerem que uma formulação de fluxo de calor diferente afeta consideravelmente a dinâmica de aquecimento e a evolução da temperatura do plasma.

Palavras-chave: Coroa Solar. Fluxo de calor. Transferência de calor. Aquecimento do plasma. Magnetohidrodinâmica. Simulação.





## LIST OF FIGURES

	<u>Page</u>
1.1 Illustration of the structure of the solar interior showing the density and the temperature in each of the four interior regions. . . . .	2
1.2 Granules in the photosphere. . . . .	4
1.3 Observations of chromosphere made by Hinode mission . . . . .	5
1.4 Solar corona observations. . . . .	6
1.5 The solar atmosphere. . . . .	7
1.6 Logarithmic distribution of the abundance of the elements relative to hydrogen where the elements found in corona are the ones labeled. . . . .	7
1.7 Plasma $\beta$ as a function of height for different regions of the solar atmosphere. . . . .	9
1.8 Observation of granules and sunspot in the photosphere. . . . .	10
1.9 Sun in EUV showing different classes of the solar corona. . . . .	10
1.10 Observations of a solar flare occurred on October 22th in 2012. . . . .	11
1.11 Comparison between (a) the drawing of a real observed corona field during an eclipse and (b) a current free corona model. . . . .	12
1.12 Coronal loops in soft X-ray observation. . . . .	13
1.13 First moments of a X-class flare in different wavelengths. . . . .	14
2.1 A compilation of radiative loss function for different elemental abundances.	21
2.2 Plot of kernel $w(x, x')$ where $x'$ goes from 0 to L with L being the total length of the loop. . . . .	27
2.3 Energy transport and temperature along a magnetic field line. . . . .	28
2.4 Log of temperature profile for (a)15s, (b)30s and (c)45s after the flare onset. . . . .	30
2.5 Log of temperature profile for the chromosphere and transition region for (a)15s, (b)30s and (c)45s after the flare onset. . . . .	30
2.6 Vertical velocity profile for (a)15s, (b)30s and (c)45 after the flare onset.	31
3.1 The graph displays how grid resolution in $z$ -direction varies with height $Z$ above photosphere layer. . . . .	35
3.2 Subdivision of the simulation domain for four processors with the variables colored according to the color of the processor. The black arrows represents the MPI communication between the partitions. . . . .	36
4.1 Active region number 11226 seen by AIA in SDO. . . . .	42
4.2 LOS magnetogram before and after applying Fourier Filtering. . . . .	42

4.3	Magnetic field extrapolation displayed in blue lines over the SDO image for magnetic field lines observed by AIA-171 due to emission in the AR 11226. . . . .	45
4.4	The vertical profiles for normalized temperature and density used as initial condition in the MHD model. . . . .	46
4.5	The initial pattern flow for AR11226 on the simulation box bottom modeled by a vortex located at $x = 10.0$ and $y = 12.5$ with $\phi_0 = 0.3$ and $l_1 = -l_0 = 2$ . The slice is colored by the $z$ -component of the field. . . . .	47
4.6	The tracing of the magnetic field for the whole domain starting at the yellow grid point and marching through the blue points. . . . .	48
4.7	The blue point along the magnetic field line between the green mesh points that have been MPI communicated. . . . .	49
4.8	A field line resulting from the integration of Eq. (4.19) for the grid point (i=70, j=70, k=100). . . . .	50
4.9	The initial temperature and density profile along the field line traced for the grid point (i=70, j=70, k=100). . . . .	51
4.10	Radiative loss function in terms of temperature in cgs units obtained for standard coronal abundance in CHIANTI code. . . . .	54
5.1	Average log of temperature in x-y plane as a function of height, $H$ . The dash-dot-dot red curves show the Spitzer-Härm (SH) results and dotted blue lines nonlocal (NL) the results by heat flux models. . . . .	56
5.2	Average log of temperature in x-y plane as a function of height for the interval $0 \text{ Mm} < H < 5 \text{ Mm}$ . The dash-dot-dot red curves show the Spitzer-Härm (SH) results and dotted blue lines nonlocal (NL) the results by heat flux models. . . . .	57
5.3	Relative percentage difference for the Temperature using SH values as reference. . . . .	58
5.4	Average vertical velocity, $U_z$ , in x-y plane as a function of height, $H$ . The dash-dot-dot black curves show the Spitzer-Härm (SH) results and dotted green lines nonlocal (NL) the results by heat flux models. . . . .	59
5.5	The averaged vertical velocity in meters per second as a function of time in seconds (horizontal axis) and height (vertical axis). . . . .	60
5.6	Averages contributions from heat flux to temperature evolution, $-(\gamma - 1)\nabla \cdot \mathbf{q}/(k_b n)$ , as a function of height for SH (black lines) and NL(red lines). . . . .	62
5.7	Averages contributions from plasma compression/expansion to temperature evolution, $-(\gamma - 1)\nabla T \cdot \mathbf{u}$ , as a function of height for SH (black lines) and NL(blue lines). . . . .	64

5.8	Averages contributions from radiative losses to temperature evolution, $-(\gamma - 1)R/(k_b\rho)$ , as a function of height for SH (black lines) and NL (orange lines). . . . .	65
5.9	Averages contributions from current dissipation to temperature evolution, $-(\gamma - 1)\eta J^2/(k_b\rho)$ , as a function of height for SH (black lines) and NL (orange lines). . . . .	66
5.10	Evolution of the maximum temperature found in corona as a function of time. . . . .	67
5.11	View for x-y plane of simulation box with the selected field line colored by the log of the temperature and the slice colored by the z-component of magnetic field. . . . .	68
5.12	Height of the loop apex, $H_a$ as a function of time. . . . .	68
5.13	The log of temperature as a function of time in seconds (horizontal axis) and the height of the loop normalized by the maximum height at time t (vertical axis). . . . .	69
5.14	The upwards and downwards flows along the field line in meters per second as a function of time in seconds (vertical axis) and the height of the loop normalized by the maximum height at time t (horizontal axis). . . . .	70
5.15	Contribution from current dissipation to temperature evolution as a function of time in seconds (vertical axis) and the height of the loop normalized by the maximum height at time t (horizontal axis). . . . .	71
5.16	Contribution from heat flux to temperature evolution as a function of time in seconds (vertical axis) and the height of the loop normalized by the maximum height at time t (horizontal axis). . . . .	72
5.17	Contribution from plasma compression/expansion to temperature evolution as a function of time in seconds (vertical axis) and the height of the loop normalized by the maximum height at time t (horizontal axis). . . . .	72
5.18	The total contribution from transport and sources terms to temperature evolution as a function of time in seconds (vertical axis) and the height of the loop normalized by the maximum height at time t (horizontal axis). . . . .	73



## LIST OF TABLES

		<u>Page</u>
2.1	ln $\Lambda$ and plasma resistivity for solar regions . . . . .	22
2.2	The ratio $\lambda_{mfp}/L_T$ for solar regions in both quiet and flaring conditions. The values for quiet Sun conditions were calculated from the initial data profile used in the code GOEMHD3D. Values resulting from numerical simulations of (ABBETT; HAWLEY, 1999) were used to compute $\lambda_{mfp}/L_T$ .	24



# CONTENTS

	<u>Page</u>
<b>1 INTRODUCTION . . . . .</b>	<b>1</b>
1.1 Solar interior and energy transport . . . . .	2
1.2 Solar Atmosphere . . . . .	4
1.3 Composition of solar atmosphere . . . . .	7
1.4 Plasma $\beta$ . . . . .	8
1.5 Solar magnetic fields . . . . .	8
1.5.1 Mathematical models for magnetic field extrapolation . . . . .	11
1.6 Heating in solar atmosphere: Nanoflares . . . . .	12
 <b>2 MODELING ENERGY TRANSPORT AND BALANCE IN A FLARING ATMOSPHERE . . . . .</b>	 <b>17</b>
2.1 MHD equations . . . . .	17
2.2 Energy loss function . . . . .	19
2.2.1 The radiation term . . . . .	19
2.2.2 Joule heating and anomalous Resistivity . . . . .	21
2.2.3 Heat flux formulation . . . . .	23
2.2.3.1 On the validity of classical thermal conductivity . . . . .	24
2.2.4 Nonlocal thermal transport . . . . .	25
2.3 Previous results on nonlocal heat fluxes . . . . .	29
 <b>3 NUMERICAL FORMULATION . . . . .</b>	 <b>33</b>
3.1 The GOEMHD3 code . . . . .	33
3.2 Grid properties . . . . .	34
3.3 Parallelization . . . . .	35
3.4 Numerical methods . . . . .	36
3.5 Null divergence condition . . . . .	39
 <b>4 METHODOLOGY . . . . .</b>	 <b>41</b>
4.1 Data selection . . . . .	41
4.1.1 Magnetic field extrapolation . . . . .	42
4.2 Boundary conditions . . . . .	45
4.3 Initial model configuration . . . . .	45
4.4 Implementation of the terms in energy loss function . . . . .	47

4.4.1	Nonlocal (NL) heat flux implementation . . . . .	47
4.4.2	Classical Spitzer-Härm (SH) . . . . .	52
4.4.3	Radiation terms . . . . .	53
<b>5</b>	<b>RESULTS . . . . .</b>	<b>55</b>
5.1	Temperature evolution and vertical velocities . . . . .	55
5.2	Energy transport and energy source contributions to the temperature . .	61
5.3	Heating dynamics along magnetic field line . . . . .	67
<b>6</b>	<b>CONCLUSIONS AND FUTURE WORK . . . . .</b>	<b>75</b>
	<b>REFERENCES . . . . .</b>	<b>79</b>



# 1 INTRODUCTION

The Sun is an ordinary star whose importance relies on its proximity to Earth and on its crucial role on the existence of life in this planet. For being the only star which is close enough to allow collecting data with sufficient detail, the Sun represents a unique opportunity to investigate stellar properties.

Other important fact about the Sun is that physical conditions in both solar interior and atmosphere have a direct impact on planetary outer atmospheres and magnetospheres. Those impacts are specially relevant when considering all technology that can be affected by solar activity. In fact, there is a research field called space weather dedicated solely to study the effects of energetic particles and fields from the Sun on ground and space technology, see for example (SCHWENN, 2006).

Phenomena like coronal mass ejection (CME), that may strongly interact with the environment of Earth, take place in the outer solar atmosphere, a region called solar corona. A good prediction model for solar activity requires studying how plasma dynamics is settled and evolved in the solar atmosphere. Hence, it is necessary to understand the role played by plasma processes and by electromagnetic fields in the plasma dynamics. Another important question regarding the Sun is about the mechanisms that sustain a million kelvin corona, known as the "coronal heating problem" (PARNELL; MOORTELE, 2012).

Magnetohydrodynamic (MHD) theory can be a powerful tool to perform numerical experiments and therefore have a better clue on the physical processes responsible for the phenomena observed in the solar atmosphere (GOMBOSI et al., 2004). The MHD simulations have been used to describe a myriad of events both in space plasmas and in the Sun. Depending on the nature of the plasma, some of the terms in the MHD equations may not be the most appropriate description of the physical properties of the medium. For example, the coronal plasma is weakly collisional and the classical theory prediction for plasma resistivity, derived under the assumption of a collisional medium, cannot reproduce the observed explosive phenomena (SCHRIJVER et al., 2011). Therefore, it is necessary to improve the description of the terms in the MHD equations in order to characterize more accurately the solar plasma behavior. This thesis is aimed at of improving the understanding of the processes of energy transport and balance in a weakly collisional plasma and how they could affect the evolution of a solar active region.

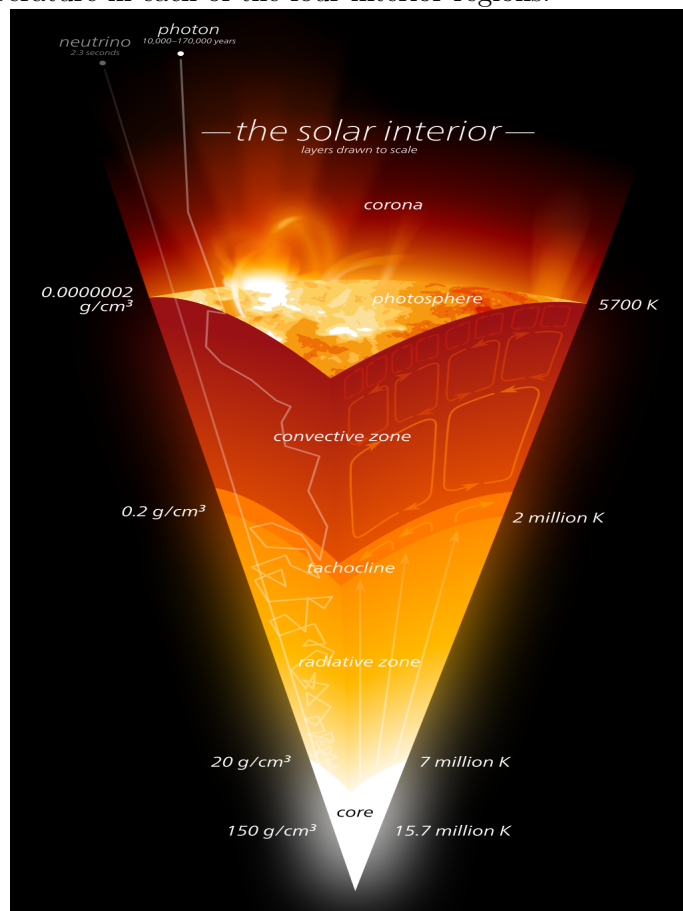
In the following sections, it is given a brief introduction on the structure of the Sun

with a particular focus on the solar atmosphere features.

## 1.1 Solar interior and energy transport

The interior of the Sun is not directly observed and its properties are studied using helioseismology (GIZON et al., 2010). The solar radius,  $R_{\odot}$ , is around 695 Mm and it is defined as the distance from the center of the Sun to its surface. The solar interior is usually divided into four regions: core, radiative zone, tachocline and convective zone (PRIEST, 2014). The classification relies on the processes happening in each layer and how the energy is transported outwards. The tachocline classification is different, it is a transition layer that plays an important role on magnetic field generation. In Fig. 1.1, the interior layers and their average properties like density and temperature are illustrated.

Figure 1.1 - Illustration of the structure of the solar interior showing the density and the temperature in each of the four interior regions.



Source: Kelvinsong (2013).

The core is the region in the center of the Sun with a radius about one quarter of solar radius ( $0.25R_{\odot}$ ). The standard model for the solar interior predicts that half of the mass of the Sun is concentrated in the core presenting a temperature of about 15 million K and a density around  $1.6 \times 10^5 \text{ kg/m}^3$ . This model assumes that variables like pressure, density and temperature drop as a function of the radial distance from the center of the Sun.

All solar energy is produced in the core by thermonuclear reactions that fuse Hydrogen into Helium releasing energy in the form of  $\gamma$  ray photons. The dense core is a highly collisional medium where the photons will bounce a million times before they can reach the next layer. [Mitalas and Sills \(1992\)](#) have estimated that the photon takes  $\sim 2 \times 10^4$  years to cover the distance from the center to the outer limit of the core.

At  $0.25R_{\odot}$  from the center of the Sun starts the radiative zone, with a temperature of about seven million K and  $\sim 87\%$  less dense than the core. Once the photons reach this layer they continue to be transported outwards by the process of absorption and re-emission and lose their energy. The radiative zone goes up to  $\sim 0.7R_{\odot}$  from the center where the density has dropped to only 0.1% of the initial density.

Around  $0.7R_{\odot}$ , the temperature has decreased to around two million Kelvin allowing part of the electrons and protons to recombine and form atoms again. That increases the opacity which in turn makes the energy transport by radiation no longer efficient. Thus, hot bubbles containing low density material are created and as they go up they get cooled down to 5700 K as they get close to the surface of the Sun. Therefore the energy is transported by the convective flux set by temperature gradients. Once the plasma reaches the surface, it finds a transparent region and photons can travel free outwards into space.

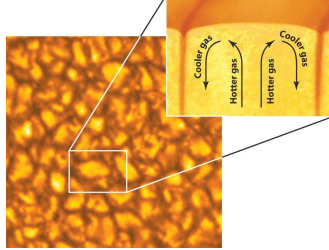
At the base of the convective zone the helioseismology predicts the existence of an interface layer where the solar magnetic field is believed to be generated by a dynamo mechanism ([CHARBONNEAU, 2014](#)). This region, called tachocline, is a thin layer ( $\sim 0.04R_{\odot}$ ) where the rotation changes from uniform in the radiative zone to a differential rotation in the convective zone. Therefore the tachocline presents strong shear velocities. That velocity field stretches the magnetic lines which intensifies the magnetic field before the field emerges due to plasma instabilities.

## 1.2 Solar Atmosphere

The convection motions in the threshold of the solar interior accelerate the plasma radially outwards and it ends up leaving the interior. As the plasma is carried out by the magnetic field, the solar atmosphere is settled. The plasma surrounding the interior of the Sun has different properties and therefore it is divided into four regions: photosphere, chromosphere, transition region and solar corona.

The photosphere is a thin layer of plasma (around 500km thick) that lies just above the convective region. Its plasma density is around  $\sim 10^{-3}\text{kg/m}^3$  and it is the atmospheric layer from where most of the visible light is emitted. The warm plasma that was accelerated into the atmosphere eventually cools down to around 5000 K and go into a descending motion. Therefore, one can see the top of those convective cells covering the entire solar surface. They are called granules and have a typical diameter of 1 Mm. (PRIEST, 2014). In visible light the granules are observed as shown in Fig. 1.2. The center of the granule is brighter because of the hotter plasma and the boundaries are darker as the plasma has cooled down.

Figure 1.2 - Granules in the photosphere.

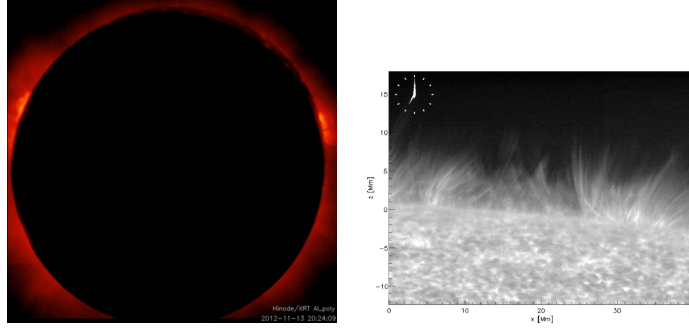


Source: Freedman et al. (2013).

The convective motions continue up in the solar atmosphere with larger convective cells ( $L \sim 20$  to  $70$  Mm) known as supergranules. Those larger scale cells are not observed in visible light, but rather tracked down by other methods like local correlation track and measurements of the Doppler shift. Just above the photosphere lies a rarer and highly non uniform medium, the chromosphere. The plasma temperature in chromosphere rises monotonically with height and at the top of this layer, the temperature starts to rise drastically. In the chromospheric temperature range,  $4400\text{K} \leq T \leq 2 \times 10^4 \text{ K}$ , the main emission process is the H-alpha emission which gives the chromosphere a red color in solar eclipses observations in visible light as seen in Fig. 1.3(a). The main structures observed in chromosphere are the spicules,

displayed in Fig. 1.3(b). The spicules are large jets of plasma that reach thousands of kilometers height and then fall down. The spicules originate in the boundaries of the supergranules and their mass flux is considerable large.

Figure 1.3 - Observations of chromosphere made by Hinode mission



(a) Solar eclipse displaying the chromosphere as a reddish ring. (b) Observation of spicules in chromosphere.

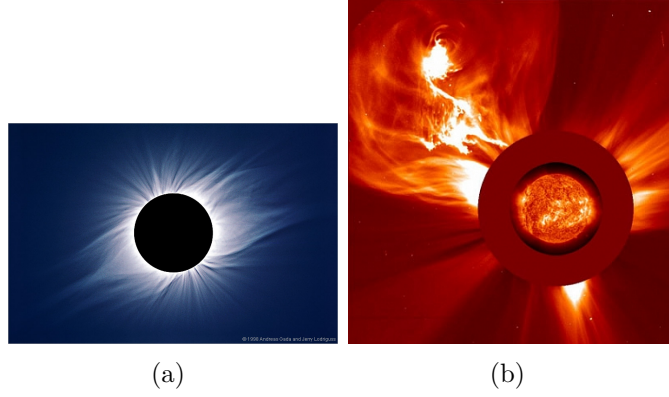
Source: (a) [Hinode \(2016\)](#), (b) [Judge and Carlsson \(2010\)](#).

Between the chromosphere and the corona there is the Transition Region (TR) layer. The main characteristic of this layer is that it presents high temperature and density gradients in a small height width. The TR can be subdivided into a lower transition region, where it shows a network structure similar to one found in chromosphere, and an upper transition region, which displays some features similar to the ones observed in the corona ([Priest, 1992](#)).

The outer solar atmosphere layer is called the solar corona. The plasma in this layer is very tenuous, hot and practically collisionless. The solar corona is always expanding in the form of a solar wind. The fluxtubes from photosphere have lost their confining pressure and emerge as individual flux tubes fulfilling the corona with a magnetized plasma. The solar corona can be observed in visible light during an eclipse as a tenuous halo surrounding the moon, Fig. 1.4(a). There are myriads of phenomena taking place in the corona due to the presence of magnetic fields there. An example of structure observed in the corona are the coronal mass ejections (CME). As the name suggests, CMEs consist of large amounts of plasma and magnetic field being ejected towards the interplanetary space. In Fig. 1.4(b) we see a coronal mass ejection leaving the Sun as captured by SOHO (Solar Heliospheric Observatory) spacecraft.

The solar atmosphere can be represented as a first approximation by the VAL (Vernazza, Avrett, Loeset) model ([Vernazza et al., 1981](#)). It is a standard one dimen-

Figure 1.4 - Solar corona observations.



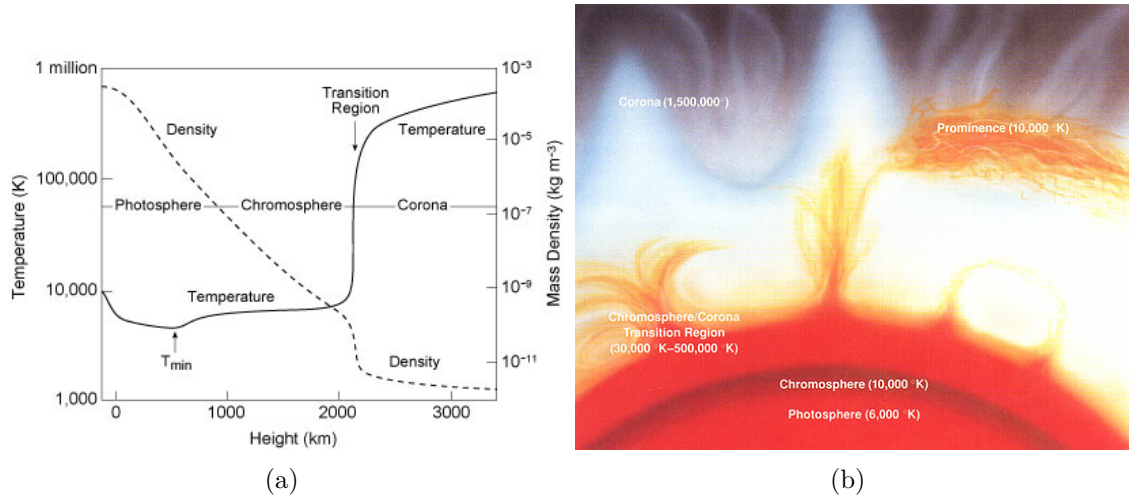
(a) Solar corona observed during the eclipse of November 13th of 2012. (b) A coronal mass ejection leaving the Sun.

Source: (a) [Emmanouilidi \(2012\)](#), (b) [SOHO \(2016\)](#).

sional model and based on a semi-empirical approach that describes the temperature (solid line) and density (dashed line) as a function of height as shown in Fig. 1.5(a). The VAL model predicts a fast density decrease in all layers except in the corona where it decreases slowly. The temperature presents a different behavior, with smooth variations in photosphere where it decreases to a minimum of 4400 K and then grows also slowly until it reaches  $2 \times 10^4$  K in the upper part of chromosphere. Then the temperature presents an exponential growing in the transition region which is around 100 km thicker in this model. In the corona the temperature gradients are smoother and the temperature reaches millions of Kelvin.

Although the VAL model is very useful to understand the general distribution of temperature and density as a function of height, it actually gives the wrong idea of a stratified atmosphere which it is not the true nature of the dynamic plasma surrounding the Sun. As the plasma is heated and cooled due to different processes, it leads to exchange of materials between the layers and then those layers might be going up or down. Also, because of the plasma confinement in the magnetic fluxtubes, one finds quite different thermal conditions across the solar atmosphere which also contributes for a non-stratified atmosphere. For example, in Fig. 1.5(b), we see that material with chromospheric properties can be found in coronal heights in the phenomena of prominences as the magnetic field isolates the material from the surrounding medium.

Figure 1.5 - The solar atmosphere.



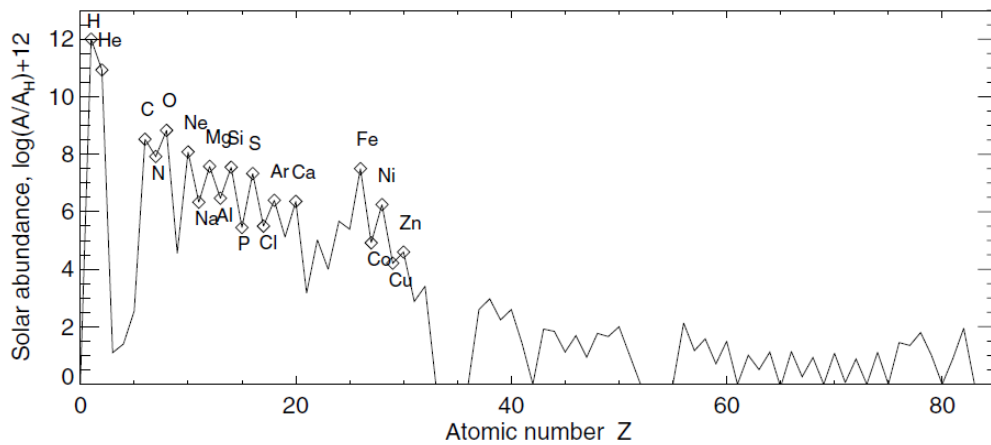
(a) VAL Model for the solar atmosphere. (b) Solar atmosphere layers process illustrated.

Source: (a) Priest (1992), (b) Garber (2013).

### 1.3 Composition of solar atmosphere

The solar atmosphere is basically composed by hydrogen and oxygen, 91.2 % and 8.7% respectively. Although the percentage of other elements are small, they actually have an important role in some aspects of the solar atmosphere such as thermal emissions and solar brightness variability.

Figure 1.6 - Logarithmic distribution of the abundance of the elements relative to hydrogen where the elements found in corona are the ones labeled.



Source: Aschwanden (2005).



Measurements of elemental abundances in the solar atmosphere are obtained through atomic spectroscopy and they indicate that the abundances for corona and photosphere are similar for most of the elements. However, due to the highly dynamic nature of corona, elements with low first ionization potential (FIP) (K, Na, Al, Ca, Mg, Fe, Si) can have enhanced coronal abundances with respect to photospheric ones (ASCHWANDEN, 2005; COOK et al., 1989). In Figure 1.6, a logarithmic distribution of the abundance of the elements relative to hydrogen is given as a function of the atomic number  $Z$ . As displayed in Figure 1.6, only elements with  $Z < 30$  have been detected in corona.

#### 1.4 Plasma $\beta$

The elements found in the corona are ionized and therefore show an effective interaction with magnetic fields. A very important feature of solar corona is the influence of the magnetic field on the plasma dynamics. This influence is described by the plasma  $\beta$  which gives the ratio between gas pressure ( $p$ ) and magnetic pressure ( $B^2/8\pi$ ),

$$\beta = \frac{8\pi p}{B^2}. \quad (1.1)$$

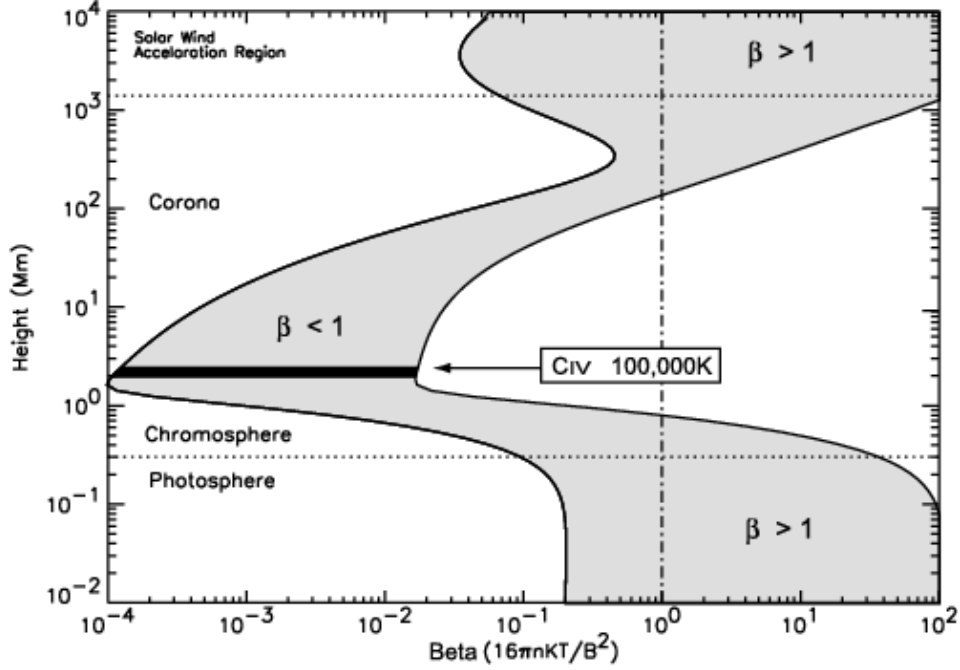
As shown in Figure 1.7, the plasma  $\beta$  changes with height. In the lower layers of the solar atmosphere, we see that the value predicted for plasma  $\beta$  is close to unit, indicating that the gas pressure value is around the same value as the magnetic pressure. In the corona, the plasma beta is usually smaller than unit which means that the magnetic field energy prevails against thermal energy for most coronal regions. In other words, low plasma  $\beta$  means that magnetic field dictates the plasma dynamics and particles are only allowed to move along field lines.

#### 1.5 Solar magnetic fields

The magnetic field that was created by dynamo action in the solar interior is carried out to the surface by magnetic buoyancy and convective motions. The fluid motion of the convective cells concentrates the magnetic field creating strong flux tubes at their boundaries. Therefore, photospheric magnetic fields are isolated in fluxtubes surrounded by free field or weak field plasma. As the fluxtube rises it encounters a rarer medium and expands, decreasing from thousands of Gauss in the base of photosphere to only a few hundred Gauss around the height of the temperature minimum close to the top of the photosphere.



Figure 1.7 - Plasma  $\beta$  as a function of height for different regions of the solar atmosphere.



Source: [Aschwanden \(2005\)](#).

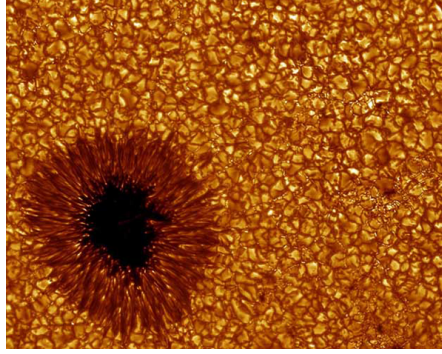
The magnetic field also presents different length scales and intensity. Depending on the magnetic flux carried out by the emerging magnetic field loop, one might have granular magnetic loops ( $10^{16}\text{Mx}^1$ ), ephemeral regions that appear in the interior of supergranules ( $10^{19}\text{Mx}$ ) and the active regions (up to  $10^{23}\text{Mx}$ ). The dynamics of the later is independent of supergranules and they are observed in visible light as dark regions in photosphere called sunspots. In Fig. 1.8 we see a sunspot, the darker region, surrounded by granules.

Depending on the dynamic and nature of magnetic field lines, the solar atmosphere can be subdivided into three different classes: quiet sun, active regions and coronal holes. In figure 1.9, the wavelength of the observation allows to have a clear image of the coronal holes (darker regions) and active regions (brighter).

The quiet regions are defined as the regions presenting ephemeral or granular fields and closed field lines. The coronal holes main feature is to display open field lines that allow the plasma to be ejected from the solar corona as a high speed solar wind. This kind of process leads to a lower plasma density which in turn is observed as darker areas on images made in extreme ultraviolet (EUV) or X-ray frequencies.

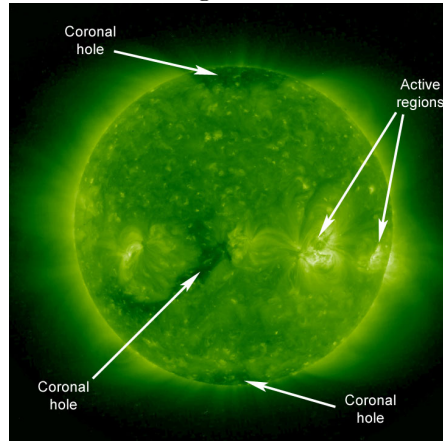
<sup>1</sup> 1 Maxwell(Mx)= $10^{-8}$ Weber(Wb)

Figure 1.8 - Observation of granules and sunspot in the photosphere.



Source: Scharmer and Langhans (2003).

Figure 1.9 - Sun in EUV showing different classes of the solar corona.

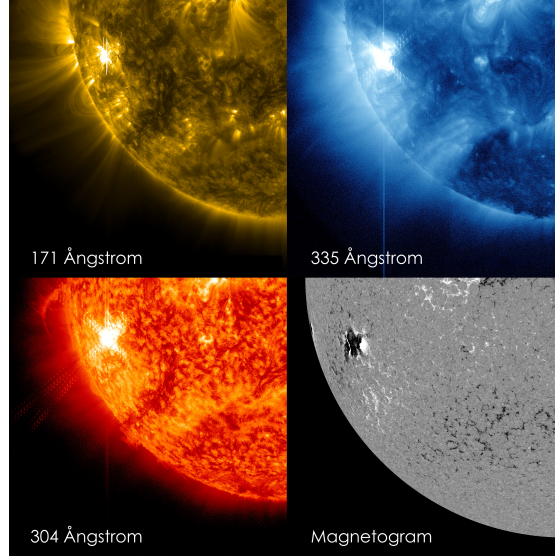


Source: STEREO (2012)

Finally, we have the Active Regions (AR), which present a high magnetic flux and are extremely dynamical regions where several solar phenomena take place. The magnetic fields of the active regions are so strong that actually interfere in the convection cells, as depicted in Fig. 1.8, and inhibits the convection leading to a cooler plasma in that region. The sunspots actually appear in pairs as the opposite polarities of the magnetic field.

In UV images, the sunspots are seen as brighter regions connected by emitting plasma trapped in magnetic field lines. Figure 1.10 displays the observations of a flare that occurred in an active region in three different wavelengths (171, 304 and 335 Ångströms) and also the associated photospheric magnetogram. In the image on the top left, we see the Sun in 171 Å and in that wavelength it is possible to identify clearly the structure of the loops as the plasma emits along the field

Figure 1.10 - Observations of a solar flare occurred on October 22th in 2012.



The top left is the Sun in 171 Å wavelength; the top right is light in 335 Å. On the bottom left is the Sun for light in the 304 Å wavelength and on the bottom right is the magnetogram.

Source: [SDO \(2012\)](#).

lines. The observation in 335 Å shows the active region brighter. The magnetogram, bottom right panel, displays the measurement of the line-of-sight (LOS) photospheric magnetic field. The white regions in the magnetogram have the field pointing towards the spacecraft observatory and the dark regions have the field directed away from the observer. The active region has stronger field and therefore is seen as a more concentrated field region.

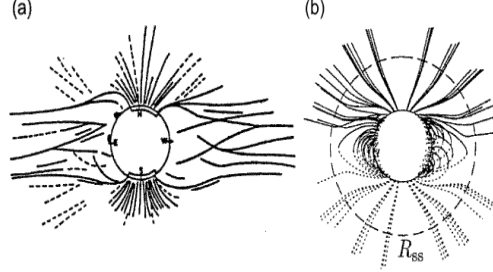
### 1.5.1 Mathematical models for magnetic field extrapolation

Comparisons between simulations and observations for coronal magnetic fields have shown that active region magnetic fields can be approximated by current free or potential field model,  $\nabla \times \mathbf{B} = 0$ , e.g. ([MACKAY; YEATES, 2012](#)). The choice of the model relies on the length scale of the phenomena being modeled and also on the computational cost. The potential field model is widely applied as it manages to describe the main features of the observed magnetic field and has a low computational cost. This model can be applied to describe some non global events as the magnetic loops.

Globally, potential field model fails as it can be seen from Fig. 1.11. Also, most of the observed EUV and X-ray structures cannot be reproduced by a potential field,

indicating that must exist a system of currents ( $\nabla \times \mathbf{B} \neq 0$ ).

Figure 1.11 - Comparison between (a) the drawing of a real observed corona field during an eclipse and (b) a current free corona model.



Source: [Mackay and Yeates \(2012\)](#).

Other common approach is to consider force free models for coronal regions,

$$\nabla \times \mathbf{B} = \kappa \mathbf{B}, \quad (1.2)$$

where  $\kappa$  is some scalar function that depends only on the local geometry of field lines. The expression presented in Eq. (1.2) can lead to a linear force free model if  $\kappa$  is a constant. A nonlinear scenario is obtained by solving the coupled equation system,

$$\vec{B} \cdot \nabla \kappa = 0, \quad (1.3)$$

$$\nabla \times \vec{B} = \kappa \vec{B}. \quad (1.4)$$

Obtaining solutions for this system is a mathematical challenge and there is no final word on whether there is an unique solution or not. Comparisons between simulations and observations shows that coronal field seems to have better fit with nonlinear force-free field model ([MACKAY; YEATES, 2012](#)).

## 1.6 Heating in solar atmosphere: Nanoflares

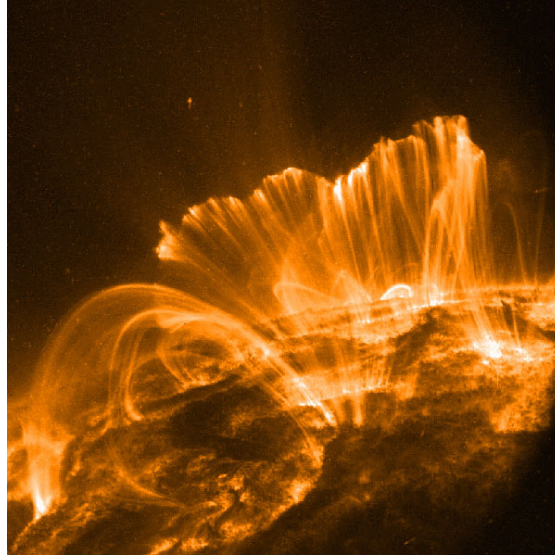
The solar magnetic field creates structures as the magnetic loops seen in Fig. 1.12. The footpoints<sup>2</sup> of the loops are continually shifted around by photospheric plasma motion. That process is called footpoint motion and it may forces parts of the loop

---

<sup>2</sup>The footpoint is defined as the intersection of the magnetic field with a given solar atmospheric layer. If there is no mention to the layer, the intersection occurs in photosphere.

with different polarity to interact. As a result, the magnetic field lines may reconnect, leading to the formation of new magnetic configurations. Magnetic reconnection can be defined as a quick change of the topology of magnetic field lines. Such process involves the creation of intense thin current sheets and the dissipation of those.

Figure 1.12 - Coronal loops in soft X-ray observation.



Source: SDO (2012)

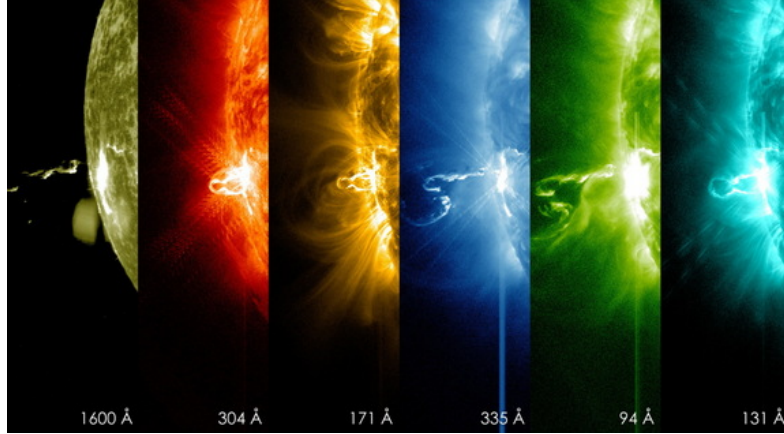
Solar flares are related to reconnection of large scale magnetic field lines which acts as a mechanism of converting non potential magnetic energy into other energy forms. A typical flare releases  $\sim 10^{21}$  up to  $10^{25} J$  of energy in form of emission (thermal and nonthermal <sup>3</sup>) and kinetic energy (SHIBATA; MAGARA, 2011; ASCHWANDEN, 2005). Part of that energy is also used to heat up the plasma, leading to plasma emitting in high frequencies. Observationally, flares are defined as an abrupt enhancement of emission in different wavelengths. In Fig. 1.13 we have the observation of an energetic flare in different wavelengths showing that the length scale of such phenomenon can be quite large.

The role of magnetic field lines in the heating of the solar atmosphere is important to explain the temperature profile observed in VAL model (Fig.1.5(a)). There we have a cooler photosphere, around 6000 K, that could not sustain a hotter upper atmosphere by heat flow. Comparisons between magnetograms from photospheric

---

<sup>3</sup>If the characteristics of the emitted radiation do not depend on the temperature of the source, the emission is known as 'non-thermal emission'.

Figure 1.13 - First moments of a X-class flare in different wavelengths.



Source: SDO (2014).

magnetic field and image in different wavelengths of the solar corona suggest hotter loops connect regions in photosphere having strong magnetic field region. Therefore, it is believed that the energy for heating the plasma comes from the magnetic energy. It is agreed that this magnetic energy is generated by shuffling and dragging the footpoints of the magnetic field lines. There are still open questions regarding the mechanism responsible for transporting that magnetic energy to upper atmosphere and also how it would be converted into thermal energy (PRIEST, 2014). Besides, there are discussions on where in the atmosphere the primary heating (the conversion from magnetic to thermal energy) would occur: corona or chromosphere and transition region (ASCHWANDEN et al., 2007). The problem of explaining how the upper atmosphere is heated is one of greatest problem in solar physics also referred to as "the coronal heating problem".

One plausible scenario to explain the higher temperatures found in solar atmosphere is to consider flares in smaller energy and size scales, known as nano or microflares (PRIEST, 2014). The nanoflares would release up to  $10^{17}$ J of energy in the atmosphere, locally heating the plasma. Part of that energy is then transported to other regions in the atmosphere by heat flux. An average active region would require around a thousand nanoflares in a time interval of 15 minutes in order to explain the observed temperatures (SCHRIJVER et al., 2011). Unfortunately, current solar observatories lack of the necessary spatial and temporal resolution to study directly the nano and microflares. The most recent evidence is based on the trace of such events found at the coronal footpoints (TESTA et al., 2014).

Understanding the process of plasma heating in the solar atmosphere implies in



describing properly the exchange of material and energy between the atmospheric layers. In this thesis we have considered the effect of low collisionality of coronal plasma on the energy transport. As there are considerable less collisions in the medium, the fast electrons are able to travel longer distances. Therefore, thermal evolution of the plasma is no longer determined by the thermal conditions in the vicinity regions but also by thermal energy brought by electrons coming from distant regions. In other words, the thermal evolution of a weakly collisional plasma is determined by nonlocal energy transport. Thus, we have implemented a nonlocal heat flux transport and also thermal emissions losses in the energy equation of MHD applied in the investigation of the thermal evolution problem of active regions. The form of the MHD equations used in this work, are presented in chapter 2. In this chapter we also introduce the formulations used for both classical heat flux and nonlocal heat flux and present previous work done by other authors ([KARPEN; DEVORE, 1987](#); [KARPEN et al., 1989](#); [CIARAVELLA et al., 1991](#)). The MHD equations were solved by numerical methods described in chapter 3. In chapter 4 we present the methodology followed in this work. The effects on plasma dynamic and thermal evolution from considering different heat flux models are presented in chapter 5. In the last chapter, we present our final thoughts on our numerical experiment.





## 2 MODELING ENERGY TRANSPORT AND BALANCE IN A FLARING ATMOSPHERE

### 2.1 MHD equations

Physical processes in space plasmas can usually be well described by MHD theory combined to appropriate boundary and initial conditions. This theory describes the existing mutual interaction between electromagnetic fields and the flow of a conductor fluid such as plasma. The fluid behavior is described by transport equations obtained by taking moments from the Boltzmann equation, see for example (BITTENCOURT, 2003). Those equations are quite similar to the Navier-Stokes ones except for the presence of currents and magnetic field. The properties regarding the magnetic field interacting with the plasma are described by induction equation, obtained from approximations<sup>1</sup> applied to Maxwell's equations and Ohm's law.

For the investigation of energy transport and balance, we have considered the following set of MHD equations:

$$\text{Mass conservation} \quad : \quad \frac{\partial \tilde{\rho}}{\partial t} = -\nabla \cdot \tilde{\rho} \tilde{\mathbf{u}}, \quad (2.1)$$

$$\text{Momentum equation} \quad : \quad \frac{\partial \tilde{\rho} \tilde{\mathbf{u}}}{\partial t} = -\nabla \cdot \tilde{\rho} \tilde{\mathbf{u}} \tilde{\mathbf{u}} - \nabla \tilde{h}^\gamma + \tilde{\mathbf{j}} \times \tilde{\mathbf{B}} - \tilde{\nu} \tilde{\rho} (\tilde{\mathbf{u}} - \tilde{\mathbf{u}}_0), \quad (2.2)$$

$$\text{Energy equation} \quad : \quad \frac{\partial \tilde{h}}{\partial t} = -\nabla \cdot (\tilde{h} \tilde{\mathbf{u}}) - \frac{(\gamma - 1)}{\gamma \tilde{h}^{\gamma-1}} \mathcal{L}, \quad (2.3)$$

$$\text{Induction equation} \quad : \quad \frac{\partial \tilde{\mathbf{B}}}{\partial t} = \nabla \times (\tilde{\mathbf{u}} \times \tilde{\mathbf{B}} - \tilde{\eta} \tilde{\mathbf{j}}), \quad (2.4)$$

where the variables  $\tilde{\rho}$ ,  $\tilde{\eta}$ ,  $\tilde{\mathbf{u}}$ ,  $\tilde{\mathbf{u}}_0$  and  $\tilde{\mathbf{B}}$  stand for normalized (and therefore dimensionless) density, resistivity, plasma velocity, neutral velocity (for chromosphere) and magnetic field. The variable  $h$  represents normalized enthalpy and it is related to thermal pressure  $p$  by  $h = (p/2)^{1/\gamma}$  with gamma standing for ratio of specific heats. Since we have considered a fully ionized hydrogen plasma, we have  $\gamma = 5/3$ . The variable  $\mathcal{L}$  is the energy loss function and is discussed in the following section.

Equations (2.1-2.4) are also known as resistive MHD equations because they consider

---

<sup>1</sup>The following approximations are made: the characteristic plasma velocity is considered to be non relativistic; assuming a non relativistic plasma allows neglecting the displacement current term in comparison with the term  $\nabla \times \mathbf{B}$  in Maxwell-Ampère Law; it is also considered that pressure dyad divergent are weak; density charge is assumed to not vary significantly with time and it is considered that Hall effects are unimportant.

dissipation effects on the induction equation. Typical values of plasma resistivity for coronal and chromospheric regions are, respectively,  $10^9 T^{-3/2}$  and  $8 \times 10^8 T^{-3/2}$  with  $T$  being the temperature of the plasma. The induction equation, Eq. (2.4), was obtained from Maxwell's equations and it couples magnetic fields to fluid dynamics through velocity field of the flow.

We have considered a velocity flow by neutrals,  $\mathbf{u}_0$ , in the bottom of chromosphere that produces the footpoints displacement. The dynamic in the rest of the atmosphere was settled by collisions between those neutral and ions as one can see by the term  $\tilde{\nu}\tilde{\rho}(\tilde{\mathbf{u}} - \tilde{\mathbf{u}}_0)$  in the momentum equation. The neutrals are only used to apply dynamic into the plasma. We also have not considered the gravity forces in order to simplify the problem.

The parameters for normalization used in this model are typical system values as:

- length scale:  $L_0 = 1\text{Mm}$ ;
- $\rho_0 = n_0 m_p$  with  $m_p$  being the proton mass and  $n_0 = 2.0 \times 10^{15} \text{m}^{-3}$  typical (number of particles)/volume;
- $B_0 = 1 \times 10^{-3} T$ , magnetic field strength;
- Velocity is normalized with Alfvén speed  $u_{A0} = B_0 / \sqrt{\mu_0 \rho_0} = 488 \text{km/s}$ ;
- Time scale is also normalized based in Alfvén speed,  $\tau_A = L_0 / u_{A0} = 2.05 \text{s}$ ;
- Resistivity is normalized with the parameter  $\eta_0 = \mu_0 L_0 u_{A0} = 3.066 \times 10^6 \Omega \text{m}$ .

Besides the above equations, it is also applied to the system the condition  $\nabla \cdot \mathbf{B} = 0$ , which assures that there is no magnetic monopoles in plasma. Other condition considered in order to have the necessary number of equations to solve for all variables is ideal gas law,

$$p = nk_b T \quad (2.5)$$

where  $k_b$  is the Boltzmann constant and it was considered a full H ionized plasma with particle density  $n$ . We considered both ions and electrons to have the same temperature and same particle density.

For the current density, we have considered

$$\tilde{\mathbf{j}} = \nabla \times \tilde{\mathbf{B}}. \quad (2.6)$$

Although a lot of assumptions were made in order to obtain Eqs. (2.1- 2.4), the equations are still nonlinear and cannot be analytically solved. Also, despite all the approximations, the equations thereby obtained are still very accurate to describe a lot of important processes.

This project was dedicated to working with Eq. (2.3), more specifically understanding the influence of energy transport by heat flux on the thermal evolution of the system. The solution of MHD equations considering two different heat flux formulations helped to evaluate the importance of finding a right heat flux formulation for the weakly collisional plasma found in the Sun.

## 2.2 Energy loss function

The energy loss function  $\mathcal{L}$  considers the energy sources, sinks and the transport by heat flux for the solar plasma. We have considered the following form:

$$\mathcal{L} = \nabla \cdot \mathbf{q} + E_r - \eta \mathbf{j}^2, \quad (2.7)$$

where the first term in Eq. (2.7) stands for energy transport by the heat flux ( $\mathbf{q}$ ), the second term ( $E_r$ ) is the total net radiation and the last term ( $\eta \mathbf{j}^2$ ) is the heating source due to current dissipation, also known as Joule heating. In the following subsections we will address each of those processes with a special focus on the heat flux formulation.

### 2.2.1 The radiation term

Electromagnetic emission can provide information about the physical processes taking place in the solar atmosphere. Part of the emission is due to thermal plasma radiation and it is the main way of observing heating signatures for solar atmospheric plasma.

Coronal plasmas can be approximated by an optically thin medium and thus all the energy radiated is practically lost. Therefore, radiation plays an important role in coronal plasma cooling. The solar corona is mostly composed by hydrogen and helium. The major cooling atomic processes due to radiation for H/He plasmas are collisional excitation, collisional ionization, recombination and free-free (bremsstrahlung emission) (WEINBERG, 2013). Both collisional excitation and ionization are mechanisms of radiation due to a free electron running into a bound electron. Recombination happens when a free electron recombines with an ion cre-

ating a neutral atom or ion in the next lower ionic state. In all those processes, part of the electron's energy is radiated after it interacts with an ion or a bound electron.

In the case of optically thin plasmas, a general loss rate for different thermal emission processes can be described by (COOK et al., 1989):

$$E_r = n_e n_p \alpha_{FIP} Q(T) \text{ J m}^{-3} \text{ s}^{-1}, \quad (2.8)$$

where  $n_e$  and  $n_p$  stands for electron and proton particle density, respectively. The  $\alpha_{FIP}$  term is a correction factor that takes in account the enhancement of FIP elements. The approximation for the loss rate in Eq. (2.8) is valid for  $T > 2 \times 10^4$  K. The function  $Q(T)$  is defined as "the power P per unit volume, per electron per unit volume and per hydrogen atom per unit of volume radiated by an equilibrium low-density optically thin plasma" (COOK et al., 1989).

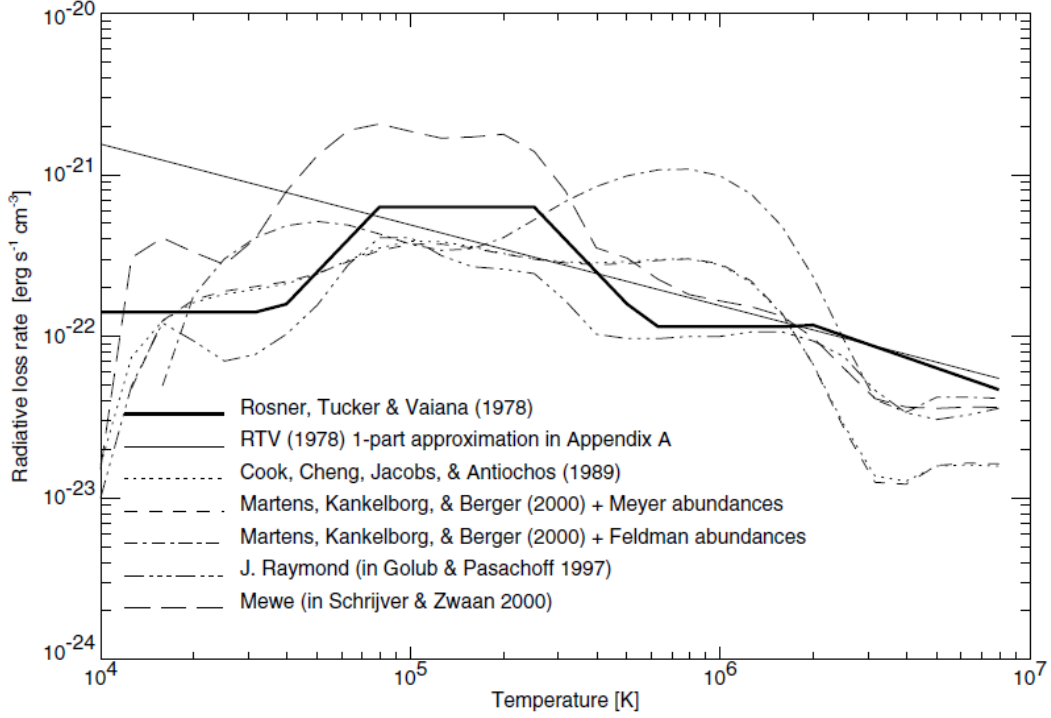
Therefore,  $Q(T)$  is called radiative loss function. Many authors have calculated  $Q(T)$  as a function of temperature (COOK et al., 1989; ASCHWANDEN, 2005) and its form depends on the elemental abundance estimation. Each curve in Fig. 2.1 shows how  $Q(T)$  varies with temperature for a certain estimation for elemental abundances. When considering the presence of iron, it is obtained for the region above  $\log T = 5$  an increase of the radiative loss function as shown by the dash-dot curve.

Most of the observed emission in microwaves and soft X-rays from chromosphere and corona are due to the free-free emission mechanism. During solar flares, free-free emission is also the major contributor to radiation observed in hard X-ray wavelengths (ASCHWANDEN, 2005). This emission results from the interaction of an electron with the micro electric field of an ion. For a collisionless plasma, the total power irradiated by a thermal free-free emission is approximated by (BOYD; SANDERSON, 2003):

$$P = \frac{8\pi}{3} \frac{Z^2 n_e n_i}{mc^3 \hbar} \left( \frac{e^2}{4\pi\epsilon_0} \right)^3 \left( \frac{k_B T_e}{m_e} \right)^{1/2} = 5.34 \times 10^{-37} Z^2 n_e n_i T_e^{1/2} (\text{keV}) \text{ W m}^{-3}. \quad (2.9)$$

The total irradiated power is proportional to the plasma density and temperature. Comparing Eq. (2.8) with Eq. (2.9), we see that in the free-free emission case  $Q(T) = 5.34 \times 10^{-37} Z^2 T_e^{1/2}$  if we consider  $\alpha_{FIP} \sim 1$ . An important aspect is that since  $P \propto Z^2$ , impurities in the coronal plasma may contribute to radiative losses despite of their concentrations. This is the reason for the different curves obtained for radiative

Figure 2.1 - A compilation of radiative loss function for different elemental abundances.



Source: [Aschwanden \(2005\)](#).

loss function for  $\log T > 5$ . That part of the curve is where free-free emission starts to prevail ([WEINBERG, 2013](#)) and, from Eq. (2.9), it is possible to verify that the coronal abundance assumed will considerably affect the curve for the radiative loss function.

### 2.2.2 Joule heating and anomalous Resistivity

The main existing model for heating of the solar corona is based on the dissipation of currents given by  $\eta j^2$ . The classical plasma resistivity for a collisional hydrogen plasma was obtained by [Spitzer \(1956\)](#) and can be written as

$$\eta = 65.36 \frac{\ln \Lambda}{T^{3/2}} \Omega \cdot \text{m}, \quad (2.10)$$

where  $\ln \Lambda$  is the Coulomb logarithm, see for example ([BITTENCOURT, 2003](#); [HELANDER; SIGMAR, 2002](#); [GOEDBLOED; POEDTS, 2004](#)). For a electron-ion collision,  $\Lambda$  may be written as ([BITTENCOURT, 2003](#))

$$\Lambda = 12\pi n_e \lambda_D^3.$$

Thus,

$$\ln \Lambda \sim 1.24 \times 10^{10} \frac{T^{3/2}}{n_e^{1/2}}.$$

The approximate values for the Coulomb logarithm and the classical resistivity for the conditions found in the solar atmosphere are displayed in Table 2.1. The low

Table 2.1 -  $\ln \Lambda$  and plasma resistivity for solar regions

	$\ln \Lambda$	$\eta(\Omega.m)$
Solar Corona	30 – 37	$10^{-6} - 10^{-7}$
TR	20	$10^{-6}$
Chromosphere	15	$10^{-3}$

values obtained for plasma resistivity in the solar corona are not enough to justify the observed energy release by current dissipation. One of the reasons the classical value for resistivity is so low is that in a weakly collisional plasma, the particles collisions are not an effective interaction. Therefore the value given by (2.10) might be no longer accurate. In fact, the values predicted by [Spitzer \(1956\)](#) for plasma resistivity are not able to reproduce the features observed in active regions and flares. Therefore, it is believed that other interactions like particles and electromagnetic fields might enhance the value predict by the Spitzer -Braginsky theory returning the so called "anomalous resistivity" ([PRIEST, 2014](#)).

An appropriate description for  $\eta$  would require a kinetic treatment at the length scale of the dissipation which is  $10^7$  smaller then the length scale of coronal features that are resolved by MHD simulations. This gap between scales imposes the problem of finding a correct parametrization for the resistivity. Simulations by [Peter et al. \(2004\)](#), [Peter et al. \(2006\)](#) using MHD models as described by [Gudiksen and Nordlund \(2002\)](#), [Gudiksen and Nordlund \(2005\)](#) have shown that  $\eta j^2$  can match the observed heating rate if much higher resistivity values are used then the ones predicted by classical transport theory. Since in the length scales where dissipation occurs the magnetic Reynolds number is close to one, [Bingert and Peter \(2011\)](#) have established that  $\eta$  can be set to provide a  $R_m \sim 1$ . We applied the resistivity values as described by [Bingert and Peter \(2011\)](#). Their parametrization do not rely on density or pressure as other existing models for enhancing the plasma resistivity. Therefore, the only variable determining the quantity of energy being deposited is the electric current. For typical length scales and velocities found in our simulations, establishing  $R_m = 1$  gives  $\eta \sim 10^4 \Omega.m$ . This higher anomalous resistivity provides

the amount of heating expected from the nanoflare heating model. The only issue with this approach is that the magnetic fields are being considerably more dissipated in our MHD model.

### 2.2.3 Heat flux formulation

Heat flux is by definition the flux of thermal energy across a surface and it is described in plasma kinetic theory as (BITTENCOURT, 2003):

$$\mathbf{q}_\alpha = \int_v \frac{m_\alpha v^2}{2} f_\alpha(v) d^3v , \quad (2.11)$$

where  $f(v)$  is the distribution function and the subscript  $\alpha$  represents the types of particle species.

The classical description for heat flux was first computed by Spitzer and Härm (1953). They considered an electronic distribution function which consisted in a Maxwellian distribution function,  $f^0$ , plus a perturbation  $f^1$

$$f = f^0 + f^1. \quad (2.12)$$

The distribution function of Eq.(2.12) was then substituted into Boltzmann equation with collision term of Fokker-Planck type. The higher order terms of perturbation function were neglected and a second order differential equation was obtained for  $f^1$ . Since the solar corona has a very small plasma beta, one can ignore the contributions from heat diffusion across magnetic field lines given by ions-ions collisions. Using the result obtained for  $f^1$ , Spitzer and Härm (SH) found an expression similar to the Fourier law:

$$\mathbf{q}_{sh} = -\kappa_{||} \nabla_{||} T , \quad (2.13)$$

where  $T$  is the plasma temperature and  $\kappa_{||}$  is the parallel component of thermal conduction tensor,

$$\kappa_{||} = 1.8 \times 10^{-10} \frac{T^{5/2}}{\ln \Lambda}.$$

The expression in Eq. (2.13) is purely local, describing the heat flux  $q_{sh}$  at a given point in terms of the temperature gradient in that point. It is a suitable description of thermal transport in collisional plasmas where the energetic electrons are not free to travel long distances.

### 2.2.3.1 On the validity of classical thermal conductivity

The collisionality of plasma can be described through the ratio between the electron mean free path ( $\lambda_{mfp}$ ) and the thermal length scale ( $L_T$ ). Using the collisional time as giving by [Helander and Sigmar \(2002\)](#) and applying quasineutrality condition,  $Zn_i \sim Zn_e$ , the electron mean free path can be written as

$$\lambda_{mfp} = \frac{12\pi^{3/2}\epsilon_0^2 k_b^2}{Ze^4} \frac{T_e^2}{n_e \ln \Lambda}. \quad (2.14)$$

Although classical thermal diffusion description is valid for a considerable range of plasmas, [Gray and Kilkenny \(1980\)](#) showed that the linear approximation in Eq. (2.12) for the distribution function fails in the limit of weak collisionality, i.e. :

$$\frac{\lambda_{mfp}}{L_T} \geq 10^{-3}, \quad (2.15)$$

Experimental data has shown that whenever the condition defined in Eq. (2.15) is obeyed, heat flux values are much smaller than the one predicted by the classical expression in Eq. (2.13), a process called inhibition of heat, see for example ([BRANTOV; BYCHENKOV, 2013](#); [GRAY; KILKENNY, 1980](#)). Another issue concerning Spitzer- Härm model is that it fails to predict plasma pre heating by hot electrons with large mean free path.

Values for the ratio  $\lambda_{mfp}/L_T$  in quiet sun and flare conditions are summarized in table 2.2. As expected, the dense and collisional plasma of chromosphere is within the limit for classical treatment. However, for upper transition region and corona, Spitzer-Härm approach may already be out of its validity range.

Table 2.2 - The ratio  $\lambda_{mfp}/L_T$  for solar regions in both quiet and flaring conditions. The values for quiet Sun conditions were calculated from the initial data profile used in the code GOEMHD3D. Values resulting from numerical simulations of ([ABBETT; HAWLEY, 1999](#)) were used to compute  $\lambda_{mfp}/L_T$ .

	Quiet Sun	Flare
Solar Corona	$10^{-3}$	$10^{-2}$
TR	$10^{-3}$	$10^{-2}$
Chromosphere	$10^{-9} \sim 10^{-6}$	$10^{-13}$



### 2.2.4 Nonlocal thermal transport

The possible inaccuracy of classical Spitzer-Härm heat flux when describing thermal transport in regions where  $\lambda_{mfp}/L_T \geq 10^{-3}$  imposes the problem of finding an alternative description for heat flux. Results from fusion plasma experiments have demonstrated that other approaches to physically justify heat flux inhibition, such as turbulent transport and generation of suprathermal electrons, do not explain the observed heat flux (BRANTOV; BYCHENKOV, 2013).

The main problem of classical thermal transport theory is that it ignores contributions from electrons having large mean free path which would naturally occur in a weakly collisional plasma. The lack of collisions leads energetic electrons to travel longer distances and to contribute to heat flux on distant regions along the magnetic field line. Therefore, a good description for heat flux in coronal plasma would have to consider a nonlocal treatment. In the nonlocal treatment, the contributions of energetic electrons are computed and the heat flux is no longer solely determined by the local gradients of temperature as described in Eq. (2.11).

Unfortunately, a nonlocal transport theory is not yet available. Thus, as an approximated approach, it is considered a linear method of perturbation to higher orders in the kinetic theory in order to mimic a nonlocal behavior. From results of kinetic simulations, Luciani et al. (1983) were able to approximate a nonlocal heat flux by a convolution integral. That expression describes the desirable properties of a nonlocal heat flux and can be applied to a fluid description of the plasma. In this approach the nonlocal expression for the electron heat flux is

$$q(x) = \int_{-\infty}^{+\infty} dx' q_{sh}(x') w(x, x'). \quad (2.16)$$

This expression tells that the heat flux computed at the point  $x$  is calculated by taking into account that the thermal condition in  $x$  might be affected by the condition in a point  $x'$  along the magnetic field line. The kernel,  $w(x, x')$ , acts by weighting the influence of the  $x'$  points on  $x$ . Equation (2.16) describes the desirable properties of a nonlocal heat flux such as limiting heat flux and pre heating of certain regions of the plasma. Another advantage of Eq. (2.16) is that it can be applied to a fluid description of the plasma. There are different delocalization kernels available in the literature (BRANTOV; BYCHENKOV, 2013). Most of the expressions for the kernels were obtained assuming conditions for the plasma that would not be applicable for the upper solar atmosphere. The one that has a better fit to Fokker-Planck simula-

tions in conditions closer to the ones found in the plasma of the solar atmosphere is the one presented in [Luciani et al. \(1983\)](#):

$$w(x, x') = \frac{1}{2\lambda(x')} \exp \left[ - \left| \int_{x'}^x dx'' \frac{n(x'')}{\lambda x' n(x')} \right| \right], \quad (2.17)$$

where  $\lambda(x')$  is the effective distance electrons of temperature  $T(x')$  can travel. It can be written in terms of the electron mean free path as:

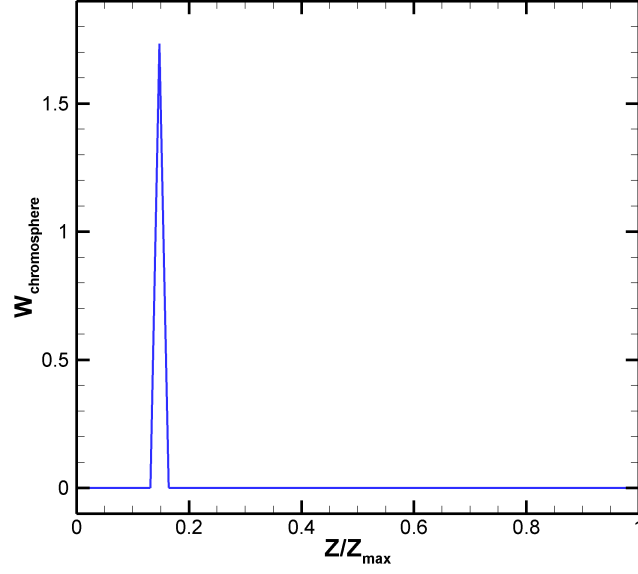
$$\lambda(x') = a(Z + 1)^{1/2} \lambda_{mp}(x') \quad (2.18)$$

with  $Z$  being the atomic number and the constant  $a$  being  $\sim 32$  in order to better fit the results from Fokker-Planck simulations. Since the main contribution for heat flux is from electrons with velocity at least three times larger than the thermal velocity, one has that  $\lambda(x') > \lambda_{mp}(x')$ . The term  $(z + 1)^{1/2}$  is due to the scattering collisions before those electrons lose their energy. Therefore, delocalization kernel acts weighting the points  $x'$  that will influence the thermal conditions in the point  $x$  where the heat flux is being computed. The influence region has an approximated size of  $2\lambda$ .

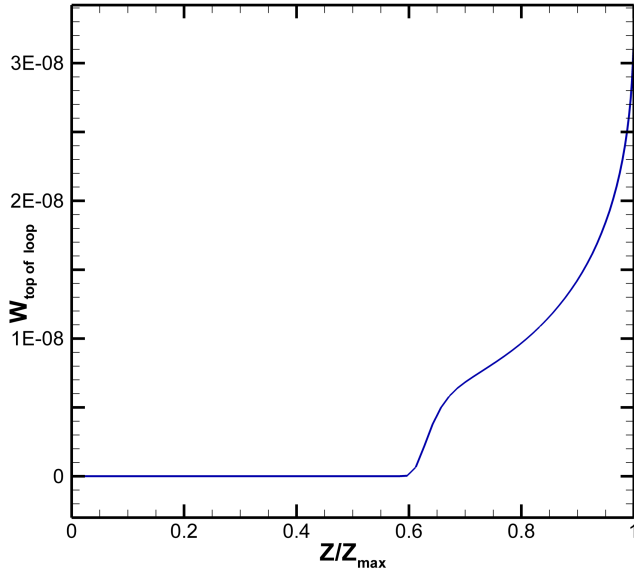
Figure 2.2 displays the kernel curves for two different regions of the loop:  $x = 0.15Z/Z_{max}$  and  $x = Z/Z_{max}$ . The horizontal axis displays the values for the points  $x'$  and in both plots this axis is normalized by the maximum loop height,  $Z_{max}$ . The vertical axis displays the values for  $w(x, x')$  and it is in SI units,  $1/m$ . In the plot of Fig. 2.2(a), we see that the kernel presents a similar behavior of a  $\delta$ -function for when the influencing point,  $x'$ , coincides with the point where the thermal conditions are evaluated, i.e,  $x' = x = 0.15Z/Z_{max}$ . Thus, there are no other points influencing the thermal conditions at  $x = 0.15Z/Z_{max}$ . In other words, in a medium with a small mean free path and low temperature and density gradients such as the chromosphere, the Eq. (2.16) will provide nonlocal heat flux values very close to the one obtained by the Spitzer-Härm (SH) expression. In Fig. 2.2(b), the kernel curve for coronal plasma is shown. We see that the influencing points  $x'$  that are important for the point  $x = Z/Z_{max}$  are in the interval range  $x' > 0.6Z/Z_{max}$ . This is expected since the large coronal mean free paths implies in broader influence regions. The larger mean free paths also causes the values of  $w$  to become considerably smaller and we may have an inhibition of the heat flux.

In Fig. 2.3(a) the divergence of classical (SH) and nonlocal heat flux are plotted for the first half of the loop with a temperature profile given by 2.3(b). Again, the height

Figure 2.2 - Plot of kernel  $w(x, x')$  where  $x'$  goes from 0 to  $L$  with  $L$  being the total length of the loop.



(a)



(b)

(a) Kernel in the upper

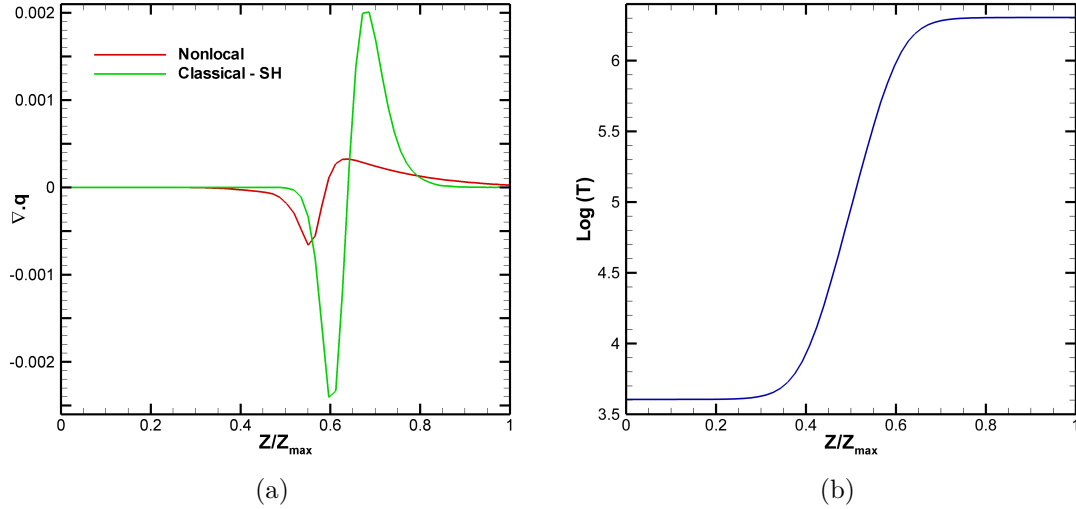
chromosphere,  $x = 0.15Z_{max}$ . (b) Kernel at the loop top,  $x = Z_{max}$

Source: Produced by the author.

of the loop is normalized by its maximum height ( $Z_{max}$ ) and the values in vertical axis are in international system of units, W/m. Figure 2.3(a) indicates that nonlocal heat flux gives significantly different values than SH model for both transition region

and corona. In the beginning of the coronal part of the loop, around  $Z/Z_{max} = 0.65$ , classical heat flux values are considerably larger than nonlocal values. That occurs because in regions of high temperature gradient, the kernel leads to a suppression of the thermal conduction where classical formulation gives the maximum value. For regions where the temperature gradient is relatively smaller and the mean free paths are still large, the contributions of fluxes going from  $x$  to  $x'$  points will lead to higher values in nonlocal heat flux. Therefore, one has slightly higher values for the divergence of nonlocal heat flux in the coronal region,  $Z/Z_{max} \geq 0.7$ . In the lower transition region/ upper atmosphere,  $0.35 \leq Z/Z_{max} \leq 0.55$ , the kernel takes into account the contribution of the electrons coming from corona and thus the predicted value for  $\nabla \cdot \mathbf{q}$  is higher in the nonlocal case. Another interesting feature displayed by Fig. 2.3(a) is that both the maximum and minimum value of  $\nabla \cdot \mathbf{q}$  are slightly displaced to the left in the nonlocal case. The displacement implies that the heat transported by nonlocal heat flux is being transported from/to different regions compared to the classical model. Also, the narrow peaks obtained by using the classical formulation compared to the broader curve peaks in nonlocal shows that Spitzer-Härm heat flux predicts a narrower location for both input and output of heat.

Figure 2.3 - Energy transport and temperature along a magnetic field line.



(a) Divergent of heat flux for SH and NL model in SI for the first half of the loop as a function of normalized loop length. (b) Temperature profile for the magnetic field line as a function of normalized loop length.

Source: Produced by the author.

In summary, an interesting feature about the nonlocal expression, as given by Eq. (2.16) and Eq. (2.17), is that it allows to recover the SH expression in the chromosphere where the plasma is highly collisional at the same time that it describes adequately what it would be expected from the nonlocal properties of heat flux in the transition region and corona.

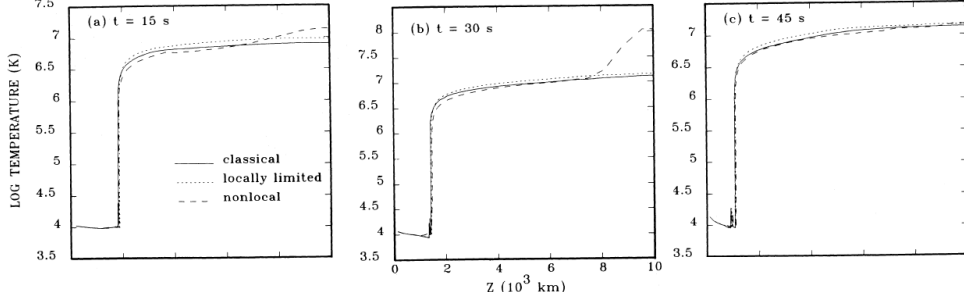
### 2.3 Previous results on nonlocal heat fluxes

A delocalised heat flux was applied to study the thermal evolution of a solar flare in (KARPEN; DEVORE, 1987) and (KARPEN et al., 1989). The authors performed an one dimensional two-fluid simulation where initially the system was in hydrostatic equilibrium. They considered an optically thin fluid and a volumetric heating function. They also took into account energy transport by convection processes. While for a quiet solar atmosphere the delocalization only gave a small difference in the base of transition region, for flaring conditions there were significant departures from temperature profile obtained when considering the SH heat flux expression as can be seen in Figs. 2.4 and 2.5 for the times  $t=15s$ ,  $30s$  and  $45s$ . Note that the scale in Fig. 2.5 varies in time because the TR is displaced to lower heights in time. The vertical velocity profile also presents considerable differences as shown by the curves in Fig. 2.6. Their results can be summarized as:

- Rise phase( $t = 15s$ ):  
nonlocal model predicts hotter/colder temperatures than classical heat flux at top/middle corona. As a consequence of the delocalised heat flux, upper chromosphere and transition region are hotter and therefore there is a smoothing of temperature gradients near the top of the loop. Also, nonlocal thermal conduction leads to an energy trapping in the upper part of the loop compared to SH model and consequently a weaker evaporation flow.
- Peak heating ( $t= 30s$ ):  
In that phase, the nonlocal results presented a temperature ten times higher than the one obtained through classical modeling. Also, in the non-local scenario the transition region is higher, while the upflow velocities are half of the ones obtained with of the SH model.
- Decay phase( $t= 45s$ ):  
Again, the nonlocal model produced a higher TR. Temperature and evaporation velocities were the same as when using classical heat flux. But evaporation of plasma last longer when applying nonlocal thermal conduc-

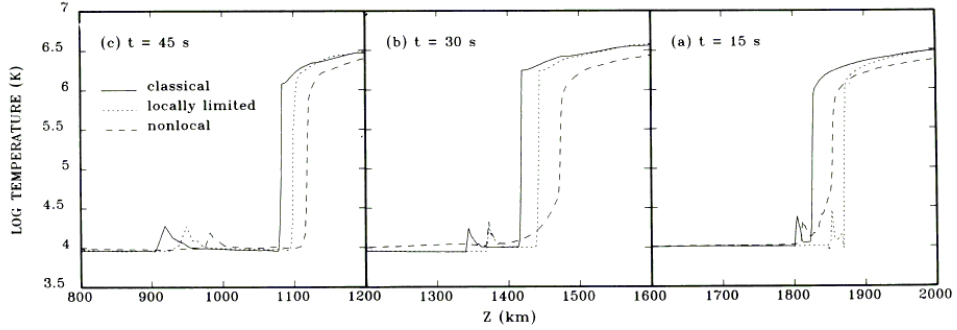
tion.

Figure 2.4 - Log of temperature profile for (a)15s, (b)30s and (c)45s after the flare onset.



Source: [Karpen and DeVore \(1987\)](#).

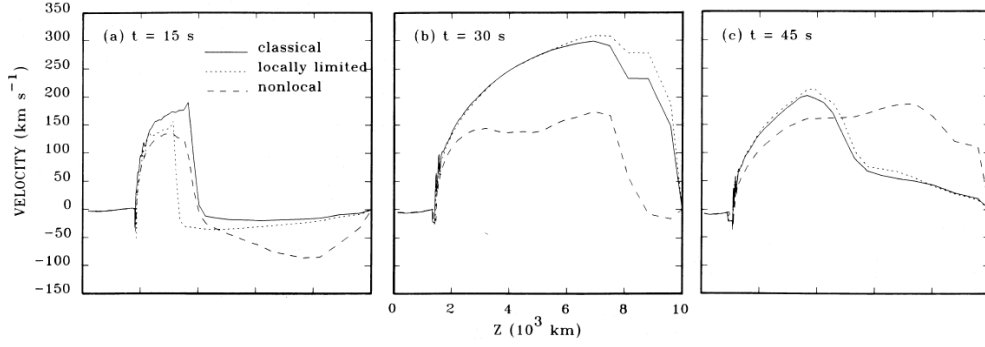
Figure 2.5 - Log of temperature profile for the chromosphere and transition region for (a)15s, (b)30s and (c)45s after the flare onset.



Source: [Karpen and DeVore \(1987\)](#).

In summary, their results showed that confined solar plasma responds differently to flare heating depending on the thermal conduction model applied. The most significant changes being in the preflare and peak heating phase when the conductive cooling dominates over radiative one. Applying the nonlocal thermal conduction gave a more accurate model for flares regarding the temperature values in corona and also provided a more eruptive heating. But there were still some discrepancies when comparing the nonlocal results to observations ([KARPEN et al., 1989](#)). A big issue is that the evaporation velocities predicted by nonlocal heat flux are significantly smaller than the observed up flow.

Figure 2.6 - Vertical velocity profile for (a)15s, (b)30s and (c)45 after the flare onset.



Source: [Karpen and DeVore \(1987\)](#).

Another work by [Ciaravella et al. \(1991\)](#) indicates that differential emission measures,  $D$ , can be increased by a factor of 2 in the temperature range of  $2 \times 10^4 K < T < 5 \times 10^4 K$  when considering a nonlocal heat flux. Also, the models obtained by them predict higher  $D$  values near the base of the loop. For the loop as a whole, they obtained that a delocalised heat flux leads to changes in  $D$  values both at the base as near the top of the loops.





### 3 NUMERICAL FORMULATION

Magnetohydrodynamics theory aims to describe the dynamics of a magnetized fluid. As presented in the previous chapter, the MHD equations are nonlinear and their solutions are obtained only by numerical analyses.

MHD have been successfully applied to investigate important processes in solar and space plasmas, *e.g.* (GOMBOSI et al., 2004; PRIEST, 2014). The main goal is to understand the physical events that occur in those environments. MHD simulation is an essential tool both to connect data and theory as well to provide data interpretation. When applied to problems in solar physics, MHD simulations can also help investigating problems that cannot be addressed experimentally because of limitations of the instruments and financial costs.

The choice of the numerical method to be applied to obtain an approximated solution relies mainly on the physical event being studied. As example of events that one may study using MHD simulations are dissipation, diffusion, convection, turbulence, shock waves and other processes. While turbulence demands high resolution methods, a study investigating physical dissipation needs low numerical dissipative methods.

A numerical method approximates continuum equations by discrete ones which are then solved. The form of those new equations and the accuracy of such approximation relies on the method applied. Regardless of the numerical tool, the solution obtained will never be an exact description of the physical phenomena because there will always be errors associated with the numerical approximation. In order to ensure that the simulation describes faithfully the physical processes, errors must be controlled and their effects on the solution understood. A good numerical method must give a reliable solution which is not compromised by the associated errors. In this chapter, the main features of the numerical aspects regarding the code used in this project are discussed.

#### 3.1 The GOEMHD3 code

The GOEMHD3 <sup>1</sup> is a three dimensional resistive MHD code which uses finite difference schemes that are second order accurate in space and time. This code was developed to give theoretical support to solar scientific investigations and its

---

<sup>1</sup>The name of the code is based on the city name acronymy where the Max-Planck Intitut für Sonnensystemforschung is located, Goettingen (GOE). The other part stands for MHD in 3 dimensions.

main properties are described by [Skála et al. \(2015\)](#). It is the third version of the MHD code created by the Theory and Simulation of Solar System Plasmas (TSSSP) group in the Max-Planck Intitut für Sonnensystemforschung. The first version of the code was called LINMOD3D <sup>2</sup> and it was used to investigate several different topics on solar physics such as:

- heating of the transition region ([BÜCHNER et al., 2004](#)) and coronal-X-ray points ([JAVADI et al., 2011](#));
- magnetic reconnection ([BÜCHNER et al., 2005](#)) and magnetic null points in the solar corona ([SANTOS et al., 2011](#));
- electrical currents ([SANTOS et al., 2008](#)) and current dissipation ([JAVADI et al., 2011](#));
- triggering of flares ([SANTOS et al., 2011](#)) and the role of helicity evolution on the dynamics of active regions ([YANG et al., 2013](#)).

The second version of the code, called MPSCORONA3D<sup>3</sup>, was parallelized using OpenMP (Open Multi-Processing). Parallelization enables using more resources, as for example a non uniform and more refined mesh, with a lower computational cost. A better resolution allowed the study of solar processes involving steep gradients. The MPSCORONA3D version was used to investigate the importance of the resistivity model for Joule heating in the corona ([ADAMSON et al., 2013](#)).

The last improvement implemented a MPI (Message Passing Interface) parallelization so that the code has now the option of running with hybrid parallelization. It has enabled the GOEMHD3 code to study problems in smaller scale as for example turbulence in current sheets ([WIDMER et al., 2016](#)).

### 3.2 Grid properties

The physical domain is discretized using a cartesian grid. The mesh can be uniform or with enhanced spatial resolutions as in [Fig. 3.1](#). The results presented in this thesis were obtained using an uniform grid in the  $x$  and  $y$  direction and a non

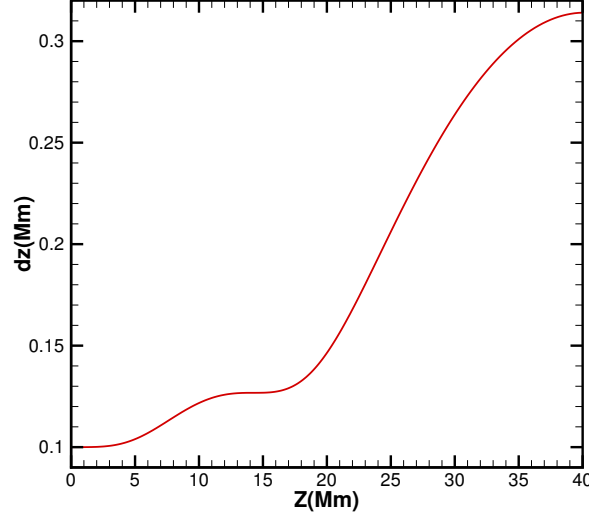
---

<sup>2</sup>The name of the code is based on the city name acronymy where theMax-Planck Intitut für Sonnensystemforschung was located, Lindau (LIN). The other part stands for module in 3 dimensions.

<sup>3</sup>The name of the code is based on the Max Planck for Solar System Research acronymy, MPS. The following part is the solar atmosphere layer that is studied by the code, Corona. The final part of the name of the code stands for 3 dimensions.

uniform grid in  $z$  (vertical) direction. The maximum resolution for  $z$  was close to the bottom of the simulation box in order to capture the strong gradients found in the transition region.

Figure 3.1 - The graph displays how grid resolution in  $z$ -direction varies with height  $Z$  above photosphere layer.



Source: Produced by the author.

The simulations used 258 grid points in  $z$ -direction covering 40Mm and  $146^2$  points in  $x$ - $y$  plane covering  $49.0^2$  Mm<sup>2</sup>. The grid spacing in  $x$ - $y$  plane was 342km and in  $z$ -direction the maximum resolution was of 100 km.

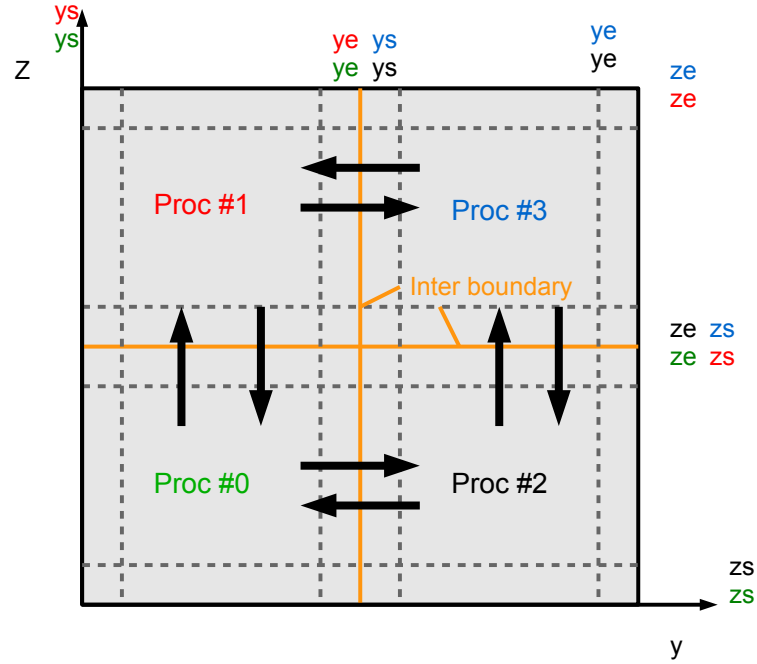
### 3.3 Parallelization

The GOEMHD3 has a hybrid parallelization scheme. This means that it can run on serial, OpenMP, MPI and hybrid (both MPI and OpenMP). For MPI and hybrid runs, the domain is partitioned in both  $y$  and  $z$  directions and distributed among the processors with the number of partitions depending on the number of available processors. For the hybrid parallelization each partition has the calculation of the loops parallelized with OpenMP.

Figure 3.2 illustrates the partition of the domain for the case when four processors are used. Each partition starts at  $ys+1$  ( $y$ -direction) and  $zs+1$  ( $z$ -direction) and finishes at  $ye-1$  and  $ze-1$ . The points  $ys, zs$  and  $ye, ze$  are along the yellow lines that represent the inter boundaries of the sub domains. Those points are called ghost

cells and they are created together with the mesh generation. At every time step, the variable values at those cells are MPI communicated. In z-direction, the upper partitions receive the values for their  $(y, z_s)$  ghosts from the  $(y, z_{e-1})$  points of the partition below. The bottom partitions receive the values for the  $(y, z_e)$  points from the  $(y, z_{s+1})$  points of the upper partition. As for the y-direction, it follows the same logic but the communication takes place between the bottom processors (#0 and #2) and between the upper processors (#1 and #3). The communication processes are illustrated by the black arrows in Fig3.2. The variables values points  $y_s, z_s, y_e$  and  $z_e$  outside the yellow line define the boundary of the domain and therefore are defined by the boundary conditions of the code. Due to the antisymmetric boundary conditions, all the subdomains must have the same dimensions,  $D = (z_e - z_s - 1)(y_e - y_s - 1)$ , for a given number of MPI tasks.

Figure 3.2 - Subdivision of the simulation domain for four processors with the variables colored according to the color of the processor. The black arrows represents the MPI communication between the partitions.



Source: Produced by the author.

### 3.4 Numerical methods

The MHD equations, Eqs. 2.1-2.4, can be re-written in terms of fluxes,  $\mathbf{F}$ , and sources,  $\mathbf{S}$ ,

$$\frac{\partial \varphi}{\partial t} + \frac{\partial F_x}{\partial x} + \frac{\partial F_y}{\partial y} + \frac{\partial F_z}{\partial z} = S, \quad (3.1)$$

where  $\varphi$  stands for a particular plasma variable. Thus, the MHD equations can be written in a matrix form as

$$\varphi = \begin{pmatrix} \rho \\ \rho \mathbf{u} \\ \mathbf{B} \\ h \end{pmatrix}, \quad \mathbf{F} = \begin{pmatrix} \rho \mathbf{u} \\ \rho \mathbf{u} \otimes \mathbf{u} - \mathbf{B} \otimes \mathbf{B} + \hat{\mathbf{I}}(p + B^2) \\ \hat{\epsilon}_{3 \times 3} \cdot \mathbf{E} \\ h \mathbf{u} \end{pmatrix} \quad S = \begin{pmatrix} 0 \\ \nu \rho (\mathbf{u} - \mathbf{u}_0) \\ -(\nabla \eta) \times \mathbf{j} \\ \frac{(\gamma-1)}{\gamma h^{\gamma-1}} \mathcal{L} \end{pmatrix}, \quad (3.2)$$

The derivatives are numerically solved by using finite difference. The first spatial derivatives in the interior points are approximately given by the following point difference operators:

$$\frac{\partial}{\partial x} \approx \delta_x = \frac{1}{\Delta x} [()_{i+1,j,k} - ()_{i-1,j,k}], \quad (3.3)$$

$$\frac{\partial}{\partial y} \approx \delta_y = \frac{1}{\Delta y} [()_{i,j+1,k} - ()_{i,j-1,k}], \quad (3.4)$$

$$\frac{\partial}{\partial z} \approx \delta_z = \frac{1}{\Delta z} [()_{i,j,k+1} - ()_{i,j,k-1}], \quad (3.5)$$

where

$$\Delta x = x_{i+1} - x_{i-1} \quad (3.6)$$

$$\Delta y = y_{j+1} - y_{j-1} \quad (3.7)$$

$$\Delta z = z_{k+1} - z_{k-1}. \quad (3.8)$$

After applying point difference operator on Eq. (3.1), it will take a form of an ordinary differential equation (ODE) that can be written in a general way by:

$$\frac{\partial \varphi}{\partial t} = f(\varphi, t), \quad (3.9)$$

where  $f(\varphi, t)$  represents the resulting expression from spatial discretization.

Solutions for  $\varphi$  are advanced in time by applying the Leapfrog time marching method to integrated Eq. (3.9). Leapfrog method uses two states to find a solution for vari-

able  $\varphi$  according to:

$$\varphi_{n+1} = \varphi_{n-1} + 2\Delta t \left[ S - \sum_{d=x}^z \delta_d F_d \right], \quad (3.10)$$

where the index  $n \pm 1$  denotes the future/past time level,  $\Delta t$  is the marching step and the index  $d$  stands for x,y and z.

Leapfrog is not a self-starting scheme. The code GOEMHD3 applies a Lax-Wendroff method to initialize the system. The Lax-Wendroff is a scheme that performs all partial derivatives together and is second order accurate. It is based in Taylor expansion series in time for a pure convective equation. For the  $\zeta$ -component of  $\varphi$ , Lax-Wendroff can be expressed in terms of point difference operators, Eqs. 3.3 - 3.5, as:

$$\varphi_j^{n+1} = \varphi_j^n - \vartheta \Delta t \delta_\zeta(\varphi_j^n) + \frac{(\vartheta \Delta t)^2}{2} \delta_{\zeta\zeta} \varphi_j^n, \quad (3.11)$$

where

$$\frac{\partial^2}{\partial \zeta^2} \approx \delta_{\zeta\zeta} = \frac{1}{\Delta \zeta^2} [(\cdot)_{i+1} - 2(\cdot)_i + (\cdot)_{i-1}]. \quad (3.12)$$

The diffusive terms are solved by using the DuFort-Frankel method. It is a second order accurate that approximates the second spatial derivatives and advance the solution in time as follow,

$$\varphi_i^{n+1} = \varphi_i^{n-1} + 2\Delta t \left[ \omega_1 \varphi_{i-1}^n + \omega_3 \varphi_{i+1}^n + \frac{1}{2} \omega_2 (\varphi_i^{n-1} + \varphi_i^{n+1}) \right], \quad (3.13)$$

where  $\omega_{1,2,3}$  are the coefficients for second order derivative in a non uniform grid,

$$\omega_1 = \frac{2}{\Delta d_b \Delta d}, \quad (3.14)$$

$$\omega_2 = \frac{-2}{\Delta d_b \Delta d_f},$$

$$\omega_3 = \frac{2}{\Delta d_f \Delta d}, \quad (3.15)$$

with "d" standing for x,y or z. The forward ( $\Delta d_f$ ) and backward ( $\Delta d_b$ ) calculations of the grid spacing are given by

$$\Delta d_f = d_{l+1} - d_l, \quad (3.16)$$

$$\Delta d_b = d_l - d_{l-1}, \quad (3.17)$$

where the index "l" can stand for  $i, j$  or  $k$  depending on if  $d=x, y$  or  $z$ , respectively.

Although the Dufort-Frankel method is an unconditionally stable scheme, its consistency relies on the condition that the time step is of the same order as the error associated with the discretizing equation.

The Leapfrog and Dufort-Frankel methods can be combined to obtain a general solution,

$$\varphi^{n+1} = \varphi^{n-1} + 2\Delta t[S^n + \sum_{d=x}^z(\chi H_l - \delta d_l F_d^n)], \quad (3.18)$$

where again the index " $l$ " can be i,j or k depending whether  $d=x,y$  or  $z$ , respectively. The diffusion term is

$$H_{i,j,k} = \sum_{l=i}^k \omega_1 \varphi_{l+1}^n + \omega_3 \varphi_{l-1}^n + \omega_2 \varphi_l^n, \quad (3.19)$$

and  $\chi$  is a coefficient that allows us to control the numerical dissipation. The former assure that the important physical processes in the simulation will not be smoothed by dissipation and that the numerical oscillations will be kept away.

### 3.5 Null divergence condition

In MHD simulation, a condition that needs special attention is magnetic field null divergence. There are truncation errors when calculating  $\vec{B}$  field and those errors are not controlled by the induction equation and, therefore, can accumulate. Thus, a nonphysical magnetic monopole can be created, breaking null divergence condition. In order to prevent this, a numerical mechanism is implemented in the code. Basically, in every time step, magnetic field divergent is computed and brought to machine zero.

In the GOEMHD3 code, the divergence null condition is granted by a projection scheme (CHORIN, 1967). At each time step, a projected field  $\mathbf{B}_{proj}$  is added to the magnetic field in a way to always have:

$$\nabla \cdot (\mathbf{B} + \mathbf{B}_{proj}) = 0. \quad (3.20)$$

To ensure that this new field  $\mathbf{B}_{proj}$  does not alter the dynamics of the plasma, the Lorentz's force due to the projected field must be null. Therefore  $\mathbf{B}_{proj}$  must be a potential field,

$$\mathbf{B}_{proj} = \nabla \phi, \quad (3.21)$$

where  $\phi$  is a scalar function.

The projection scheme requires the solution of Poisson's equation,  $\nabla^2\phi = \nabla \cdot \mathbf{B}$ , in the entire domain of simulation for each time step.



## 4 METHODOLOGY

An important and crucial aspect when studying phenomena through simulation is to properly model the physical process. In the solar corona, magnetic field modeling is a challenge due to its 3D nature and to the fact that coronal plasma is transparent to most of the available methods for measuring that field, *e.g.* (WIEGELMANN et al., 2014). Another important variable is the photospheric velocity field. In several of the existing theories on flares and coronal heating the motion of footpoint of magnetic field lines play an important role (PRIEST, 2014). In this thesis, the initial conditions applied to model the magnetic fields of an active region were obtained from observational data.

In this chapter, the initial and boundary conditions used in the model are presented. First we introduce the selected data from where the configuration for the magnetic fields was obtained. After, the methods for extrapolating the photospheric field are presented and discussed. It is also discussed the initial configuration for temperature and density used to mimic the conditions found in the solar atmosphere. Finally, we introduce the implementations made on the code regarding the nonlocal heat flux and radiation.

### 4.1 Data selection

We selected a solar active region where solar flares took place to extract data. The active region NOAA 11226 <sup>1</sup> was chosen due to the presence of small flares and a class-M flare <sup>2</sup>. Figure 4.1 shows an image obtained by AIA onboard of the SDO (Solar Dynamics Observatory) satellite for a wavelength of 171 Å.

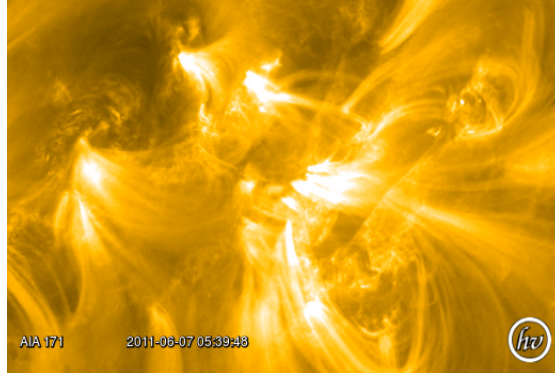
The active region was visible on the solar disk the first time on May 29th around 20:30:00 UT and we extracted the data from June 7th at 05:45:00 UT. We also used data from the line-of sight (LOS) component of the photospheric magnetic field obtained by Helioseismic and Magnetic Imager (HMI) aboard of the SDO. The LOS magnetograms were Fourier filtered retaining the first sixteen modes thus removing gradients that are not resolvable by the computational grid. In Fig. 4.2, the two panels display LOS magnetogram obtained for AR11226. The left panel displays the LOS magnetogram before being Fourier filtered and the right panel displays the

---

<sup>1</sup>The number of the active region is designated by NOAA(National Oceanic and Atmospheric Administration)

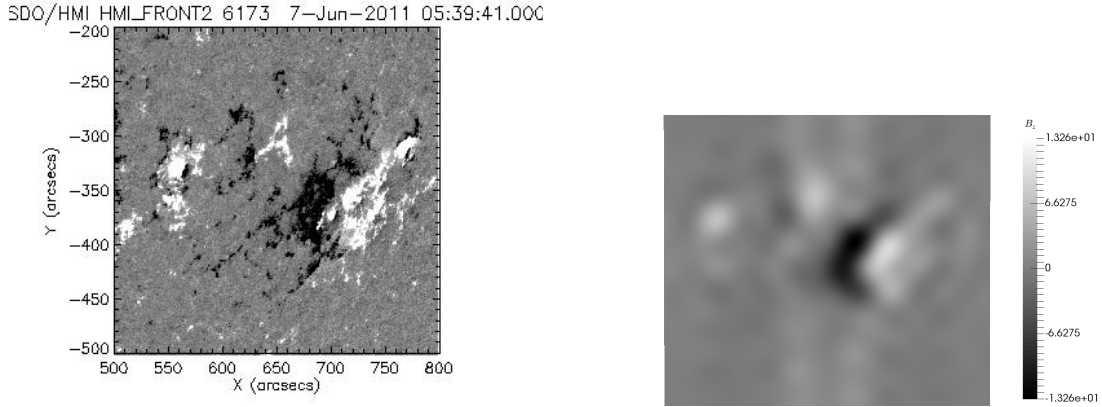
<sup>2</sup>According to the X-ray peak flux ( $Wm^{-2}$ ) measured near Earth by the GOES satellites, solar flare can be classified from the less intense peak flux (class A and B) to the most strong peak flux, class X (VANCANNEYT; et. al., 2014). There are five classes in total: A, B, C, M, X

Figure 4.1 - Active region number 11226 seen by AIA in SDO.



Source: SDO (2012)

Figure 4.2 - LOS magnetogram before and after applying Fourier Filtering.



Source: (a) SDO (2012). (b) Produced by the author.

result after Fourier filtering.

#### 4.1.1 Magnetic field extrapolation

It is a difficult task to try to replicate with high accuracy the properties of magnetic fields in corona since the coronal plasma is transparent to most of measurement techniques and it is hard to recover the magnetic field tridimensional topology, *e.g.* (WIEGELMANN et al., 2014; ASCHWANDEN, 2005). The photosphere is the only layer of the solar atmosphere where the magnetic field can be reliably measured. In this project, the coronal field was obtained by extrapolating photospheric magnetic field measurements for AR 11226.

The Fourier filtered photospheric magnetic field was assumed to be a potential field ( $\nabla \times \mathbf{B} = 0$ ) and it was extrapolated according to Otto et al. (2007). The first step in

the extrapolation process is preconditioning the data from the filtered magnetogram by imposing both line symmetry and corner field conditions:

$$\Psi_{mn}(-x, -y) = \Psi_{mn}(x, y) \quad x = x_{min} = 0, \quad (4.1)$$

$$\Psi_{mn}(L_x + x, -y) = \Psi_{mn}(L_x - x, y) \quad x = x_{max} = L_x. \quad (4.2)$$

Next, it is assumed that the  $z$ - component of magnetic field can be written as Fourier series:

$$\begin{aligned} \Psi_{mn} = & c_1 \sin\left(\frac{\pi m}{L_x}x\right) \sin\left(\frac{\pi n}{L_y}y\right) + c_2 \sin\left(\frac{\pi m}{L_x}x\right) \cos\left(\frac{\pi n}{L_y}y\right) \\ & + c_3 \cos\left(\frac{\pi m}{L_x}x\right) \sin\left(\frac{\pi n}{L_y}y\right) + c_4 \cos\left(\frac{\pi m}{L_x}x\right) \cos\left(\frac{\pi n}{L_y}y\right), \end{aligned} \quad (4.3)$$

where  $L_{x,y}$  is the size of computational domain in  $x, y$ -direction and  $c_{1,2,3,4}$  are coefficients to be determined.

Applying line symmetry to Eq. 4.3 leads to  $c_2 = c_3$ . Therefore, the  $B_z$  Fourier expansion is simplified as

$$\Psi_{mn} = c_{mn}^{(1)} \sin\left(\frac{\pi m}{L_x}x\right) \sin\left(\frac{\pi n}{L_y}y\right) + c_{mn}^{(2)} \cos\left(\frac{\pi m}{L_x}x\right) \cos\left(\frac{\pi n}{L_y}y\right), \quad (4.4)$$

where  $m$  and  $n$  are positive and the coefficients  $c_{mn}$  are given by:

$$c_{mn}^{(1)} = 2(d_{mn}^{(2)} - d_{mn}^{(1)}), \quad (4.5)$$

$$c_{mn}^{(2)} = 2(d_{mn}^{(2)} + d_{mn}^{(1)}). \quad (4.6)$$

The coefficients  $d_{mn}^{(2)}$  and  $d_{mn}^{(1)}$  are obtained from the filtered discrete magnetic field data,  $\Psi(ix, iy)$ , according to:

$$d_{mn}^{(1)} = \frac{1}{MN} \sum_{ix}^{M-1} \sum_{iy}^{N-1} \Psi(ix, iy) \exp\left(\frac{\pi k ix}{M} + \frac{\pi l iy}{N} - \frac{\pi l}{2}\right), \quad (4.7)$$

and

$$d_{mn}^{(2)} = \frac{1}{MN} \sum_{ix}^{M-1} \sum_{iy}^{N-1} \Psi(ix, iy) \exp\left(-\frac{\pi k ix}{M} - \frac{\pi l iy}{N} + \frac{\pi l}{2}\right), \quad (4.8)$$

where  $k$  and  $l$  are the expansion modes and  $M = L_x/\Delta_x$  and  $N = L_y/\Delta_y$ .

In order to find a solution to the force free configuration, it is considered an expansion

in the form,

$$B_x = \exp(-\lambda z)(c_{1x} \sin \alpha x \cos \beta y + c_{2x} \cos \alpha x \sin \beta y), \quad (4.9)$$

$$B_y = \exp(-\lambda z)(c_{1y} \sin \alpha x \cos \beta y + c_{2y} \cos \alpha x \sin \beta y), \quad (4.10)$$

$$B_z = c_1 \exp(-\lambda z) \sin \alpha x \sin \beta y + c_2 \exp(-\lambda z) \cos \alpha x \cos \beta y. \quad (4.11)$$

Applying the potential field condition, relationships between those new coefficients are found. Comparing with Eq. 4.4, the following general solutions for magnetic field components are obtained

$$\begin{aligned} B_x &= \sum_{m,n \text{ odd}} \frac{c_{mn}^{(1)}}{\lambda_{mn}^2} \exp(-\lambda_{mn} z) (-\alpha_m \lambda_{mn} \cos \alpha_m x \sin \beta_n y) \\ &+ \sum_{m,n \text{ odd}} \frac{c_{mn}^{(2)}}{\lambda_{mn}^2} \exp(-\lambda_{mn} z) (\alpha_m \lambda_{mn} \sin \alpha_m x \cos \beta_n y), \end{aligned} \quad (4.12)$$

$$\begin{aligned} B_y &= - \sum_{m,n \text{ odd}} \frac{c_{mn}^{(1)}}{\lambda_{mn}^2} \exp(-\lambda_{mn} z) (\alpha_m \lambda_{mn} \sin \alpha_m x \cos \beta_n y) \\ &+ \sum_{m,n \text{ odd}} \frac{c_{mn}^{(2)}}{\lambda_{mn}^2} \exp(-\lambda_{mn} z) (\alpha_m \lambda_{mn} \cos \alpha_m x \sin \beta_n y), \end{aligned} \quad (4.13)$$

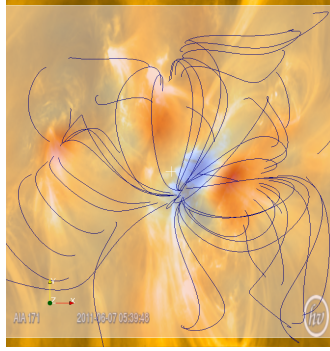
$$\begin{aligned} B_z &= \sum_{m,n \text{ odd}} c_{mn}^{(1)} \exp(-\lambda_{mn} z) (\alpha_m \lambda_{mn} \sin \alpha_m x \sin \beta_n y) \\ &+ \sum_{m,n \text{ odd}} c_{mn}^{(2)} \exp(-\lambda_{mn} z) (\alpha_m \lambda_{mn} \cos \alpha_m x \cos \beta_n y). \end{aligned} \quad (4.14)$$

Their solutions establish the initial configuration for coronal magnetic field.

The resulting extrapolation was re-sized to fit the simulation box. A 95% reduction of the  $x, y$ -plane area was required. This reduction was done in order to have enough resolution in the  $x, y$  plane without using a high number of grid points which would lead to high computational cost due to all the integrations performed in the nonlocal routine.

Figure 4.3 displays the result of the magnetic field extrapolation for AR11226. In blue are the extrapolated field lines against the field lines seen in 171 Å. As one can see by comparing the blue lines and the emitting lines, the potential magnetic field does not provide a perfect match to the magnetic field geometry of corona. But it certainly is able to reproduce the main features which is sufficient within the aims and goals established for this thesis.

Figure 4.3 - Magnetic field extrapolation displayed in blue lines over the SDO image for magnetic field lines observed by AIA-171 due to emission in the AR 11226.



Source: Adapted from SDO (2012).

## 4.2 Boundary conditions

The extrapolation method described previously demands that all the boundary conditions used to perform the extrapolation are consistent with the boundary conditions applied to the MHD model (OTTO et al., 2007). That forces line-symmetric boundary conditions to be applied to the lateral boundaries. Symmetric variables transforms as  $f(-x, y, x) = f(x, y, z)$  and antisymmetric ones as  $f(-x, y, z) = -f(x, y, z)$ .

Classical theory generates an unique solution for the potential function if its value on the boundary is specified or when its derivative normal to the boundary (Neumann boundary) is specified. The GOEMHD3 code has a Neumann boundary conditions on the bottom,

$$\frac{\partial f}{\partial n}|_{z_{min}, z_{max}} = 0, \quad (4.15)$$

to guarantee a unique solution for  $\mathbf{B}$ . The component of magnetic field normal to the bottom layer is considered to be a potential field, therefore  $j_x = j_y = 0$ . The upper boundary is open thus we consider flows through top layer in this model.

## 4.3 Initial model configuration

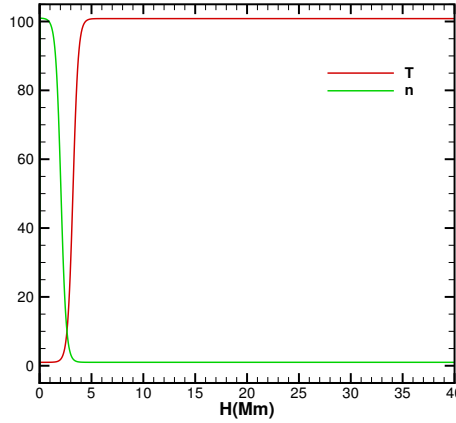
Although the model does not consider gravity, it mimics the height stratification observed in solar atmosphere by considering the following initial density profile:

$$\rho(z) = \frac{\rho_{chr}}{2}[1 - \tanh(2z - 2z_0)] + \rho_{cor}, \quad (4.16)$$

where  $\rho_{chr}$  is the chromospheric density and  $\rho_{cor}$  is the coronal density. Initially, the transition region is placed at 1.5Mm or  $z_0 = 3$ .

Pressure is assumed to be initially constant and homogeneously distributed in the simulation domain. Those conditions along with ideal gas law,  $T = p/k_b n$  gives the observed temperature profile. The initial density and temperature vertical profiles are given in Figure 4.4.

Figure 4.4 - The vertical profiles for normalized temperature and density used as initial condition in the MHD model.



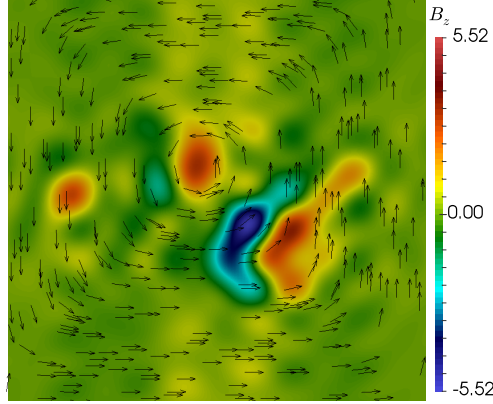
Source: Produced by the author.

The dynamic is set by imposing a velocity field for the plasma in the bottom of the simulation box. The velocity field,  $\mathbf{u}_0$ , was approximated by an incompressible vortex:

$$\mathbf{u}_0 = \nabla \times \left[ \frac{\phi_0}{\cosh\left(\frac{x-y+c_0}{l_0}\right) \cosh\left(\frac{x-y+d_0}{l_1}\right)} \right], \quad (4.17)$$

where  $\phi_0$ ,  $c_0$ ,  $l_0$ ,  $d_1$ ,  $l_1$  are parameters whose values relies on observations. The position  $(x_v, y_v)$  of the vortex gives the values of  $d_0 = -(x_v + y_v)$  and  $c_0 = -(2y_i + d_0)$ . The parameter  $\phi_0$  is the velocity intensity of the vortex, whereas  $l_1$  and  $l_0$  determine both size and shape of the vortex. Figure 4.5 displays the initial velocity field chosen for AR11226. The choice of a vortex to describe the velocity at the bottom of the simulation domain is due to the fact that a vortical flow would a priori favors the generation of currents in the system as it rotates the magnetic field lines. The vertical component of plasma velocity,  $u_z$ , can be found assuming that the photospheric magnetic field satisfies at least the vertical component of ideal MHD

Figure 4.5 - The initial pattern flow for AR11226 on the simulation box bottom modeled by a vortex located at  $x = 10.0$  and  $y = 12.5$  with  $\phi_0 = 0.3$  and  $l_1 = -l_0 = 2$ . The slice is colored by the  $z$ -component of the field.



Source: Produced by the author

induction equation:

$$\frac{\partial \mathbf{B}_z}{\partial t} = \nabla \times (\mathbf{v}_h \times \mathbf{B}_z + \mathbf{v}_z \times \mathbf{B}_h). \quad (4.18)$$

This velocity is imposed to the plasma via collision term in the momentum equation.

#### 4.4 Implementation of the terms in energy loss function

The terms for thermal conduction and plasma radiation have been implemented in the code to properly simulate energy transport in solar atmosphere. In this section, we present how the implementation was done for each one of those terms.

##### 4.4.1 Nonlocal (NL) heat flux implementation

The nonlocal heat flux expression, Eq. (2.16), demands computing quantities such as density and pressure along the magnetic field lines. In order to apply it in a three dimensional context, for each grid point a magnetic field line path  $l$  was traced by integrating the direction  $\hat{\mathbf{B}}$  of the magnetic field,

$$\frac{d\mathbf{l}(s)}{ds} = \hat{\mathbf{B}}(\mathbf{l}(s)). \quad (4.19)$$

The integration was solved by the trapezoidal rule,

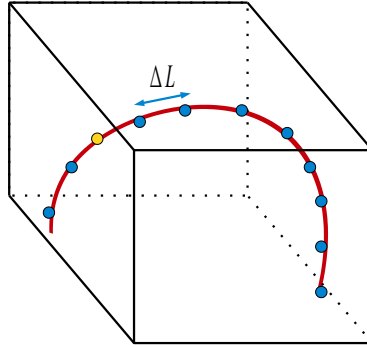
$$\int_{L_i}^{L_f} \mathbf{B}(\mathbf{l}(s)) ds \approx \sum_{ii=1}^N \frac{\Delta s}{2} [\mathbf{B}(l_{ii+1}) + \mathbf{B}(l_{ii})], \quad (4.20)$$

where the index  $ii$  refers to the one dimensional mesh along the field line and we have choosen  $\Delta l = 0.1dz_{min}$ . The tracing starts at the grid point and then first it goes forward ( $sg = +1$ ) and then backwards ( $sg = -1$ ) along the magnetic field line. In other words, a spatial march with a  $\Delta_s$  step is performed until the line reaches one of the boundaries,

$$\begin{aligned} x_l(ii) &= x_l(ii-1) + sg\Delta l \frac{B_{x_l}}{|\mathbf{B}|}, \\ y_l(ii) &= y_l(ii-1) + sg\Delta l \frac{B_{y_l}}{|\mathbf{B}|}, \\ z_l(ii) &= z_l(ii-1) + sg\Delta l \frac{B_{z_l}}{|\mathbf{B}|}. \end{aligned} \tag{4.21}$$

Figure 4.6 illustrates this process. We see the original grid point in yellow and the blue points that were obtained by integrating Eq. (4.19).

Figure 4.6 - The tracing of the magnetic field for the whole domain starting at the yellow grid point and marching through the blue points.



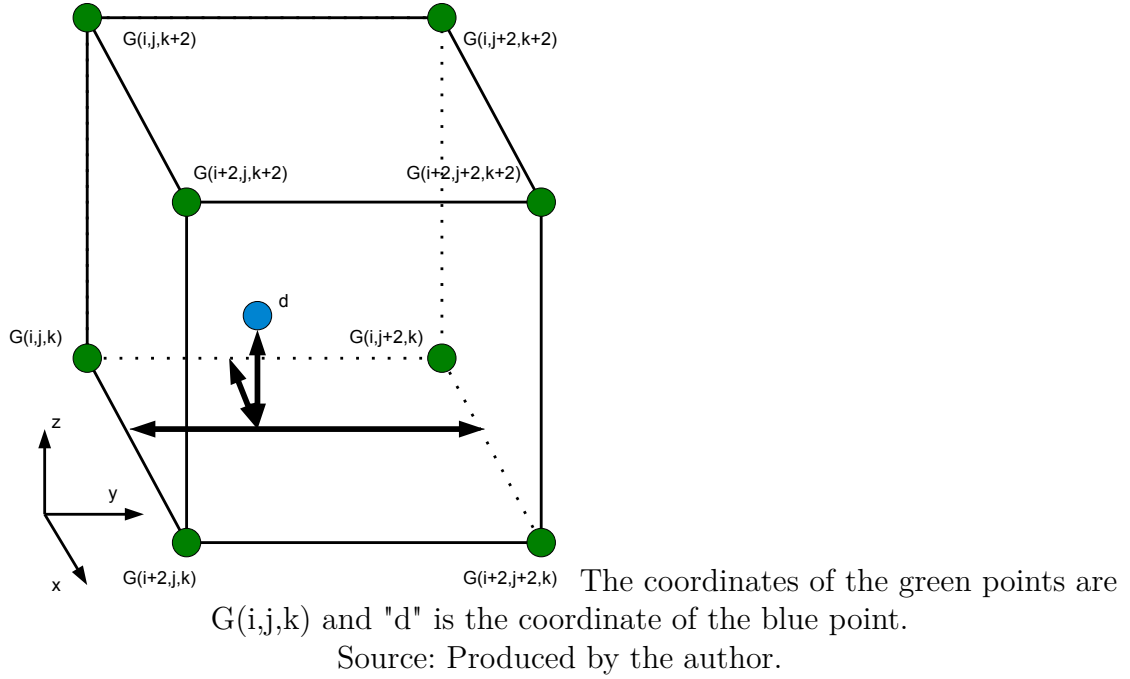
Source: Produced by the author.

The blue points are not necessarily defined by the mesh and thus the values of the variables at the points along the field line are obtained by a trilinear interpolation. Tracing a magnetic field line along a domain that it is MPI partitioned implies that the values in grid points from different partitions have to be MPI communicated to the partition where the integration is being performed. Due to computational costs,



the values of the variables needed for both integrating Eq. (4.19) and to do the heat flux computation along different MPI partitions were communicated only for every other point as illustrated in Fig. 4.7. The MPI communicated points are in green and each point has a position  $G$ . The point in blue is a point along the magnetic field line that is being traced and where the properties are going to be interpolated. The vector position  $\mathbf{d} = x_l\hat{x} + y_l\hat{y} + z_l\hat{z}$  denotes the distance of the blue point to the origin of the coordinate system.

Figure 4.7 - The blue point along the magnetic field line between the green mesh points that have been MPI communicated.



The value of the variable  $\varphi$  at the blue point is obtained by applying the following interpolation:

$$\begin{aligned}
 \phi(ii) &= ([\varphi_{i,j,k}(1 - \Delta_x) + \varphi_{i+1,j,k}\Delta_x](1 - \Delta_y) \\
 &+ [\varphi_{i,j+1,k}(1 - \Delta_x) + \varphi_{i+1,j+1,k}\Delta_x]\Delta_y)(1 - \Delta_z) \\
 &+ ([\varphi_{i,j,k+1}(1 - \Delta_x) + \varphi_{i+1,j,k+1}\Delta_x](1 - \Delta_y) \\
 &+ [\varphi_{i,j+1,k+1}(1 - \Delta_x) + \varphi_{i+1,j+1,k+1}\Delta_x]\Delta_y)\Delta_z,
 \end{aligned} \tag{4.22}$$

where

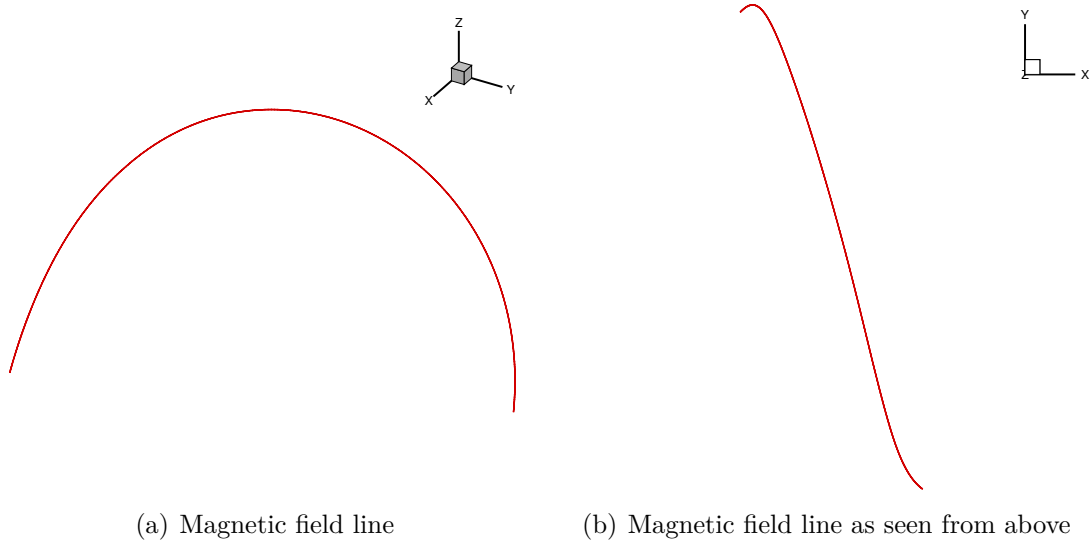
$$\Delta_x = \frac{(d_x(ii) - G(i, j, k))}{(G(i + 2, j, k) - G(i, j, k))}, \quad (4.23)$$

$$\Delta_y = \frac{(d_y(ii) - G(i, j, k))}{(G(i, j + 2, k) - G(i, j, k))}, \quad (4.24)$$

$$\Delta_z = \frac{(d_z(ii) - G(i, j, k))}{(G(i, j, k + 2) - G(i, j, k))}. \quad (4.25)$$

Thus, the interpolation (4.22) calculates the values of  $\phi$  by doing a weighted average of the values in the grid point using  $\Delta_{x,y,z}$  as the weights. Figure 4.8 displays a field line obtained as a result of integrating Eq. (4.19) using every other point to compute interpolated values.

Figure 4.8 - A field line resulting from the integration of Eq. (4.19) for the grid point (i=70, j=70, k=100).

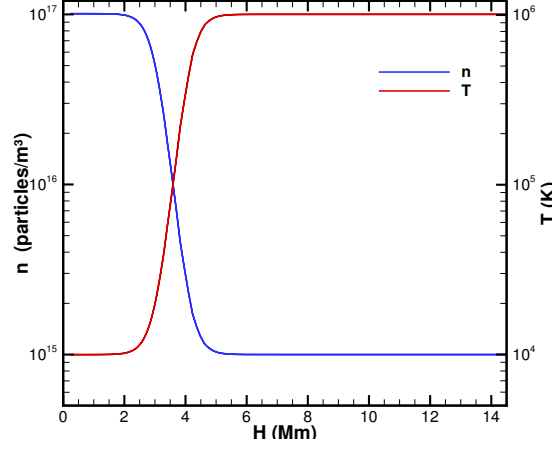


Source: Produced by the author.

The trilinear interpolation with just every other point was also able to replicate the profiles for density and temperature as it can be seen in Fig. 4.9.

Finally, to compute the nonlocal heat flux it was necessary to compute the kernel in Eq. (2.17) and the classical heat flux ( $q_{sh}$ ). For each spatial step, the interpolation in Eq. (4.22) was performed giving the values for density and pressure at the point  $(x_l(ii), y_l(ii), z_l(ii))$ . Then the values for temperature and Coulomb logarithm were computed so that all the variables needed for the integrations were available. In

Figure 4.9 - The initial temperature and density profile along the field line traced for the grid point (i=70, j=70, k=100).



Source: Produced by the author.

order to save memory and machine time, we only saved the values for the current interpolated point, index  $ii$ , and the previous point, index  $ii - 1$ . Again, the integrals in (2.17) and (4.22) were solved by trapezoidal method. At each interpolated point, the integral in (2.17),  $W$ , was done by performing again a spatial march, i.e, the values in the summation were added at each point  $ii$  along the line:

$$W(ii) = W(ii - 1)n(ii - 1)\lambda(ii - 1) + \frac{\Delta l}{2} \frac{n(ii) + n(ii - 1)}{n(ii)\lambda(ii)}$$

Then, at each of those points along the field line a spatial march was performed for the integral in the nonlocal heat flux,

$$q_{nl}(i, j, k) = \Pi(i, j, k) + \Delta s q_{sh}(ii - 1) \frac{1}{2\lambda(ii - 1)} e^{-|W(ii-1)|}. \quad (4.26)$$

where  $\Pi(i, j, k)$  is the array saving the information on  $q_{nl}(i, j, k)$  on the previous  $ii - 1$  point.

The x,y and z components of the nonlocal heat flux in the Cartesian grid were given by

$$(\mathbf{q}_{nl})_x = \mathbf{q}_{nl} \cdot \frac{\mathbf{B}_x}{|\mathbf{B}|} \mathbf{x}, \quad (4.27)$$

$$(\mathbf{q}_{nl})_y = \mathbf{q}_{nl} \cdot \frac{\mathbf{B}_y}{|\mathbf{B}|} \mathbf{y} \quad (4.28)$$

$$,(\mathbf{q}_{nl})_z = \mathbf{q}_{nl} \cdot \frac{\mathbf{B}_z}{|\mathbf{B}|} \mathbf{z}. \quad (4.29)$$

During the routine, we used non-normalized values for computation. In the end of the routine we normalized the values found for  $\mathbf{q}_{nl}$  with  $q_0 = 2p_0v_0$

#### 4.4.2 Classical Spitzer-Härm (SH)

The classical heat flux, Eq. (2.13), which we write again here:

$$\mathbf{q}_{sh} = -\kappa_{||}(\nabla T)_{||},$$

was also implemented in the GOEMHD3 code. First ,the temperature for each grid point is computed where again non normalized values were used. Then the gradient of the temperature is calculated in the mesh by applying the central differences:

$$(\nabla T)_x = \delta_x T, \quad (4.30)$$

$$(\nabla T)_y = \delta_y T, \quad (4.31)$$

$$(\nabla T)_z = \delta_z T. \quad (4.32)$$

As the gradient of the temperature was not computed along the line, the vector  $\nabla T$  can be written as

$$\nabla T = (\nabla T)_{||} + (\nabla T)_{\perp}, \quad (4.33)$$

where the subscript  $\perp$  stands for the perpendicular component of  $\nabla T$  comparing to the magnetic field. The parallel component of the vector can be obtained by its projection onto  $\mathbf{B}$ ,

$$(\nabla T)_{||} = \frac{(\nabla T) \cdot \mathbf{B}}{|\mathbf{B}|} \frac{\mathbf{B}}{|\mathbf{B}|}. \quad (4.34)$$

The heat flux was computed and its value was normalized using  $q_0$  before calculating the divergence of the heat flux. In both nonlocal and classical heat flux the divergence was not computed using points along the field line but in the mesh. Thus, using

central differences to approximate the derivatives, we obtain the heat flux divergence,

$$\nabla \cdot \mathbf{q} \approx \delta_x q_x + \delta_y q_y + \delta_z q_z. \quad (4.35)$$

The boundary conditions applied for the heat flux were the same as the ones applied to the other variables. The divergence and the  $z$ -component of the heat-flux are symmetrical variables and the  $x-y$  component of the heat flux are anti-symmetrical.

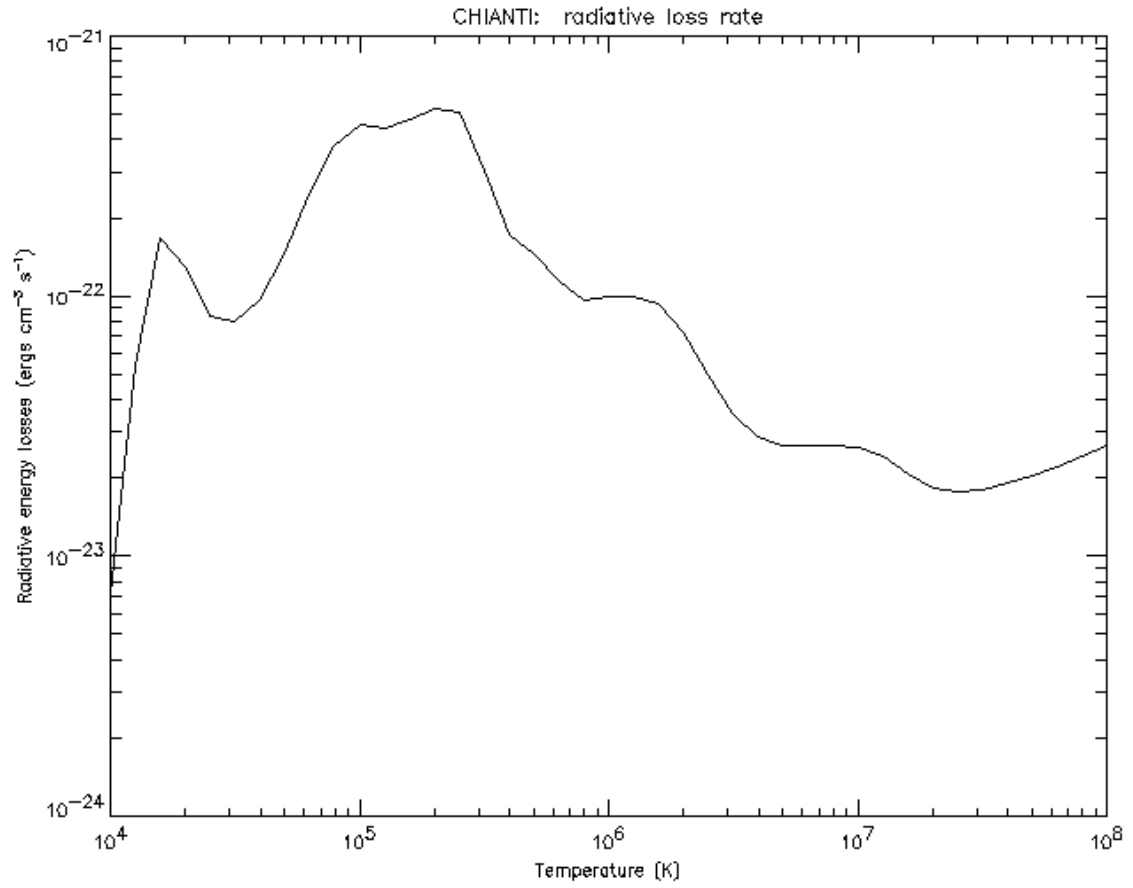
#### 4.4.3 Radiation terms

For the range of temperatures found in coronal plasma and due to its low collisionality, the most important emission process is free-free emission (ASCHWANDEN, 2005). However, there are other emission processes that, although prevail in other temperature intervals, are also important to coronal loss budget (COOK et al., 1989). At the time this thesis was written, the most precise model available for the radiative loss function is the one given by the CHIANTI code (ZANNA et al., 2015).

We choose 40 equally spaced points for the range  $2 \times 10^4 K \leq T \leq 10^8 K$  along the curve in Fig 4.10 and extracted the values for  $Q(T)$  and  $T$ . The radiative loss function in the code was calculated by performing a trilinear interpolation for temperatures among those values. We have only considered the radiative loss function for optically thin plasmas, *i.e.*, the temperature should be greater then  $2 \times 10^4$  K.

The model configuration hereby presented together with the implementations performed in GOEMHD3 allowed us to simulate the energy transport in a solar atmosphere with parameters for plasma and magnetic field similar to the ones found in an active region. The simulations were performed in the Max Planck Group cluster HYDRA and in the cluster GAUSS at the National Center of Super computation (CESUP) located in Porto Alegre, Brazil. The results obtained are presented and discussed in the following chapter.

Figure 4.10 - Radiative loss function in terms of temperature in cgs units obtained for standard coronal abundance in CHIANTI code.



Source: [Zanna et al. \(2015\)](#).

## 5 RESULTS

We investigated how different formulations of heat flux would affect the energy transport and balance in a modeled atmosphere with plasma parameters similar to the ones found in the solar corona and having a high gradient temperature defining a transition region. Two simulations were performed starting from exactly the same initial conditions, the difference being a different heat flux formulation (NL and SH).

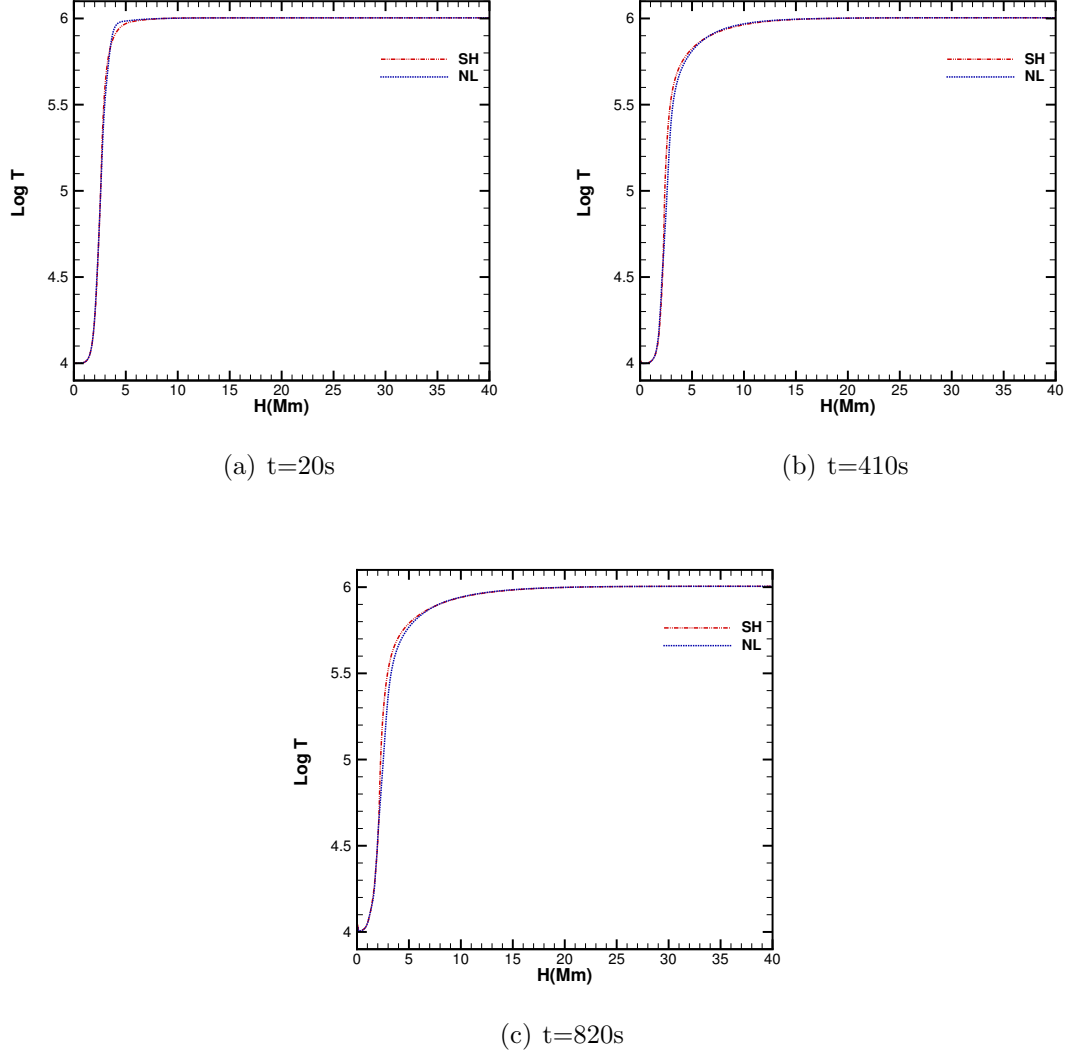
### 5.1 Temperature evolution and vertical velocities

First we have compared the evolution of the solar plasma as described by the MHD model used here with the results found by (KARPEN; DEVORE, 1987) for a hydrostatic 1D approach. They have simulated a flaring loop with both classical and NL model and their main results are concerned to differences found in the temperature profile and up/down flow velocities.

The vertical profile of the temperature averaged along x-y plane is displayed in Fig. 5.1 at three different instants of time (20 s, 410 s and 820 s) for the classical SH (dash-dot-dot red line) and for NL (dotted blue line) models. The evolution in Fig. 5.1 shows a heating front propagating from the base of the corona towards the base of TR, widening the transition region and smoothing the gradient of temperature there. As the energy is transported downwards, the base of the corona cools down. In general, both models were able to replicate the main characteristics of the standard temperature profile for solar atmosphere. As the base of TR is getting heated, it goes to lower heights moving from 3 Mm to around 2Mm. The base of the corona is also moved to in lower heights over time in both models.

From the results presented in Fig. 5.1, we see that the main differences between the models are found in the region comprised by the upper chromosphere, transition region and lower corona in the height range  $0 \text{ Mm} < H < 5 \text{ Mm}$ . Therefore, we choose to have a closer over view of that region as shown in Fig. 5.2. The main effect of NL heat flux formulation is to produce a both colder and smoother TR compared to classical heat flux. Due to the delocalization effect, the energy output from the corona is initially considerable smaller then the classical one, which in turn gives a hotter lower corona as it can be seen in Fig.5.2(a). Another consequence that comes from the features of nonlocal transport is the earlier start of rising in temperature for upper chromosphere for the NL simulation as depicted in the middle panel, Fig. 5.2(b). As the energy is being distributed more evenly compared to SH, the NL predicts a smoother TR meaning also a slower temperature rise. The tendencies

Figure 5.1 - Average log of temperature in x-y plane as a function of height,  $H$ . The dash-dot-dot red curves show the Spitzer-Härm (SH) results and dotted blue lines nonlocal (NL) the results by heat flux models.

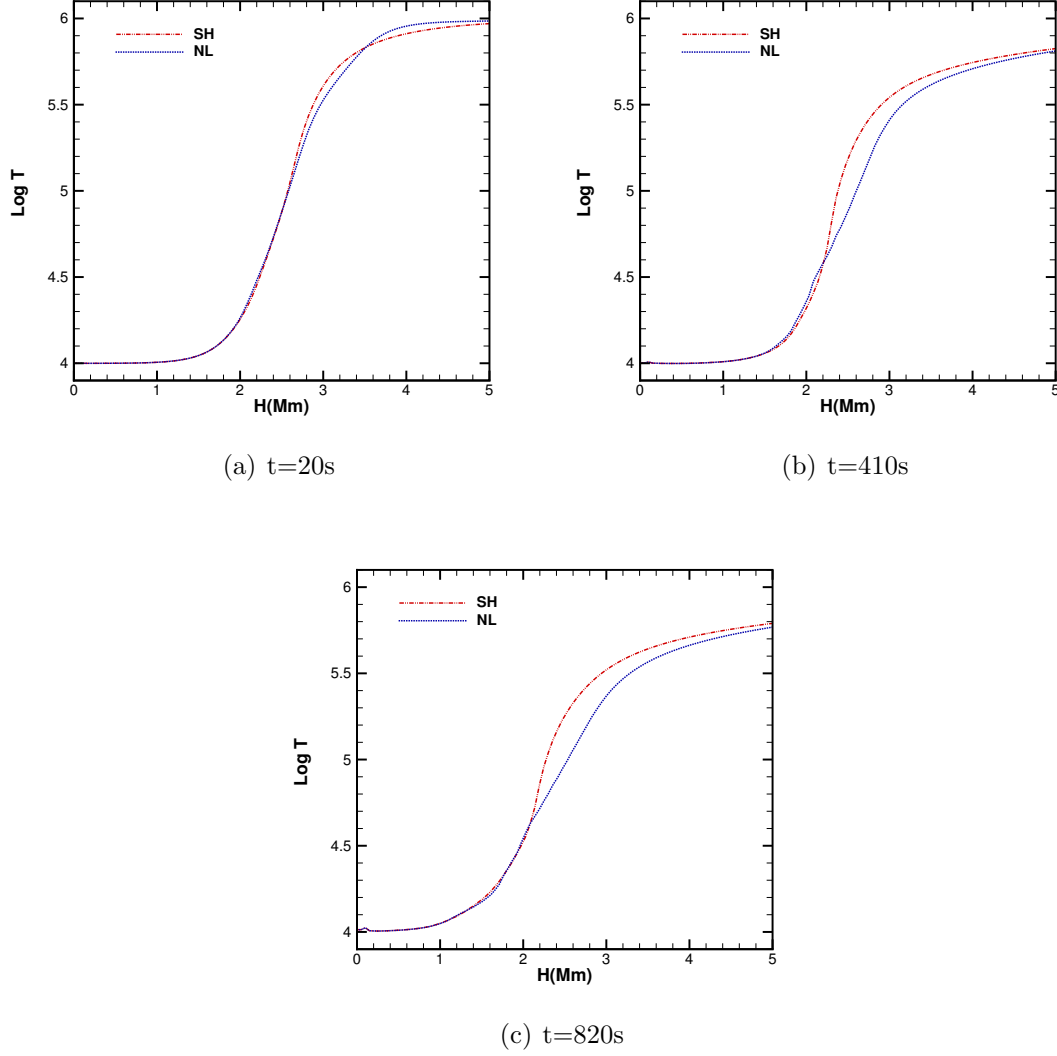


Source: Produced by the author.

observed in the middle of the simulation for TR and upper chromosphere are kept through the end of the simulation as it can be seen in Fig. 5.2(c). Although both model predicts that by the end of the simulations the TR would in average starts at same height,  $H \sim 2\text{Mm}$ , the nonlocal places the beginning of the corona around 500 km higher then the SH formulation. Therefore the delocalization kernel not only smooths the TR, it also expands the thickness of that layer as the nonlocal predicts a slower growing of temperature.



Figure 5.2 - Average log of temperature in x-y plane as a function of height for the interval  $0 \text{ Mm} < H < 5 \text{ Mm}$ . The dash-dot-dot red curves show the Spitzer-Härm (SH) results and dotted blue lines nonlocal (NL) the results by heat flux models.

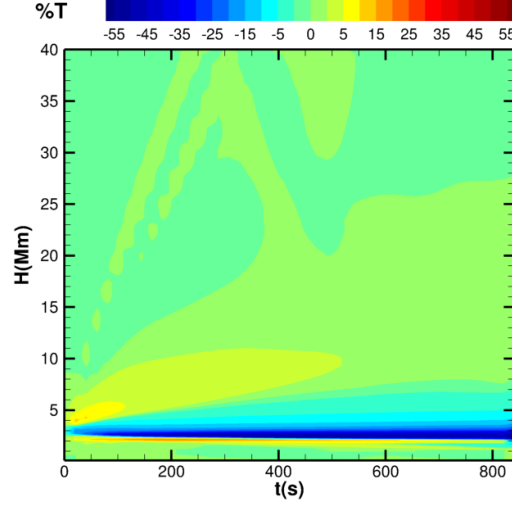


Source: Produced by the author.

The panel in Fig. 5.3 shows the relative percentage difference in the temperature values between NL and SH formulations using the classical heat flux values as reference. There we confirm that the main differences between the two formulations appear in the upper chromosphere-transition region-lower corona, with NL producing a hotter upper chromosphere, cooler transition region and slightly hotter temperatures for upper corona.

The heat flux sets pressure gradients in the simulation domain and the plasma

Figure 5.3 - Relative percentage difference for the Temperature using SH values as reference.



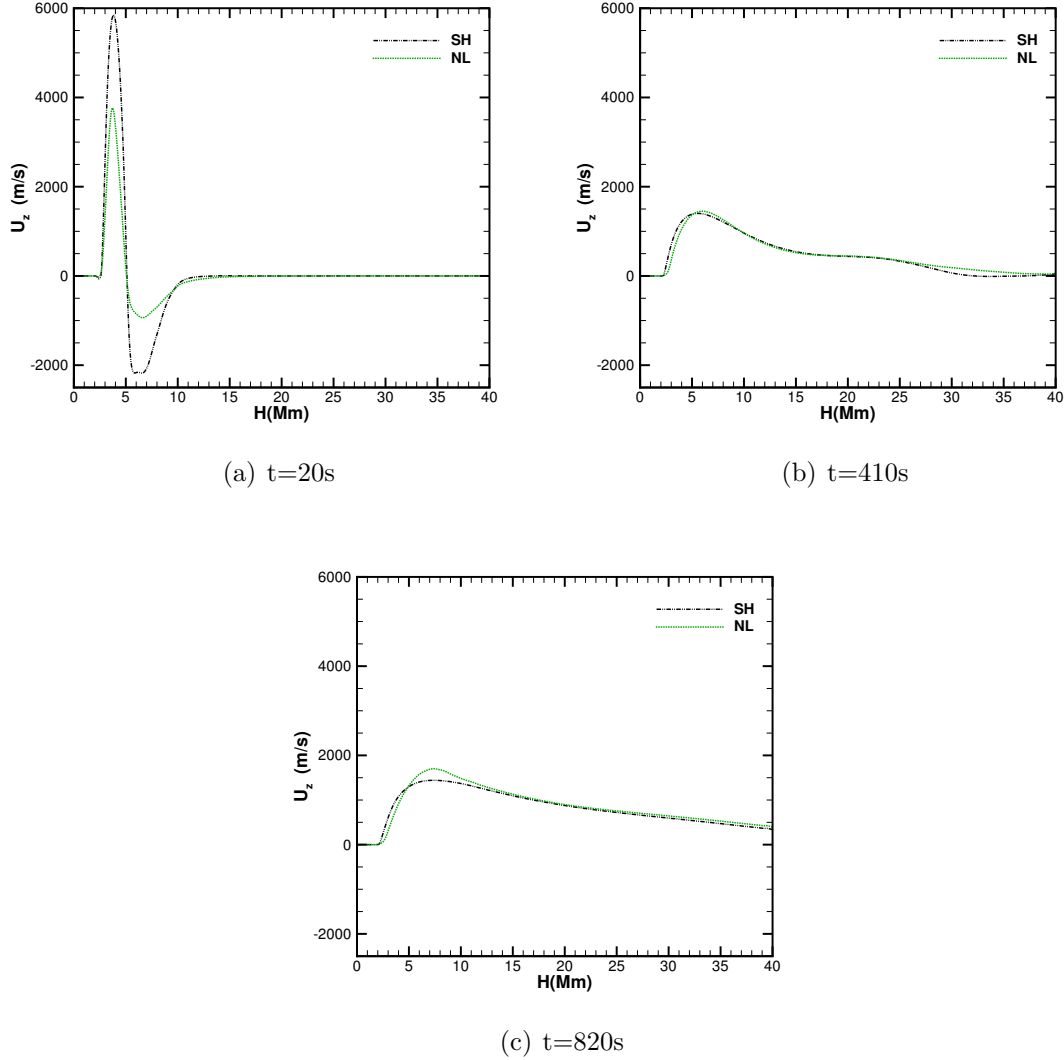
Source: Produced by the author.

responds with flows along the field lines. The averages for vertical velocities in the x-y plane as a function of height are displayed in Fig.5.4. The positive values for the vertical profile of the z component of the velocity indicates that plasma is moving upwards in the atmosphere and the negative sign denotes down flows. Both models present a quite similar behavior with the differences appearing in TR and corona. At  $t=20$  s there is a strong plasma upflow from upper chromosphere up to the transition region, and a strong plasma downflow in the lower corona. This velocity distribution makes a mix of plasma coming from both upper chromosphere and lower corona in the transition region. The SH predicts quite higher vertical velocities compared to NL, up to 50% higher.

Figures 5.4(b) and 5.4(c) show that for the selected later times there are lower values for upflows and no visible downflows with the highest values in the height range  $5 \text{ Mm} < H < 10 \text{ Mm}$ . We see that the differences between the models considerably diminishes and the NL gives slightly higher upflows velocities in corona. From the middle of simulation towards the end, the average vertical velocity is dominated by upflows above the TR and there are small upwards/downwards velocity flows in the chromosphere region.

The evolution in time of averaged vertical velocity for each model can be seen in the panels of Fig. 5.5. The results for classical heat flux are displayed in the left panel, Fig. 5.5(a), and the nonlocal in Fig. 5.5(b). The panels are colored by the averaged z-

Figure 5.4 - Average vertical velocity,  $U_z$ , in x-y plane as a function of height,  $H$ . The dash-dot-dot black curves show the Spitzer-Härm (SH) results and dotted green lines nonlocal (NL) the results by heat flux models.



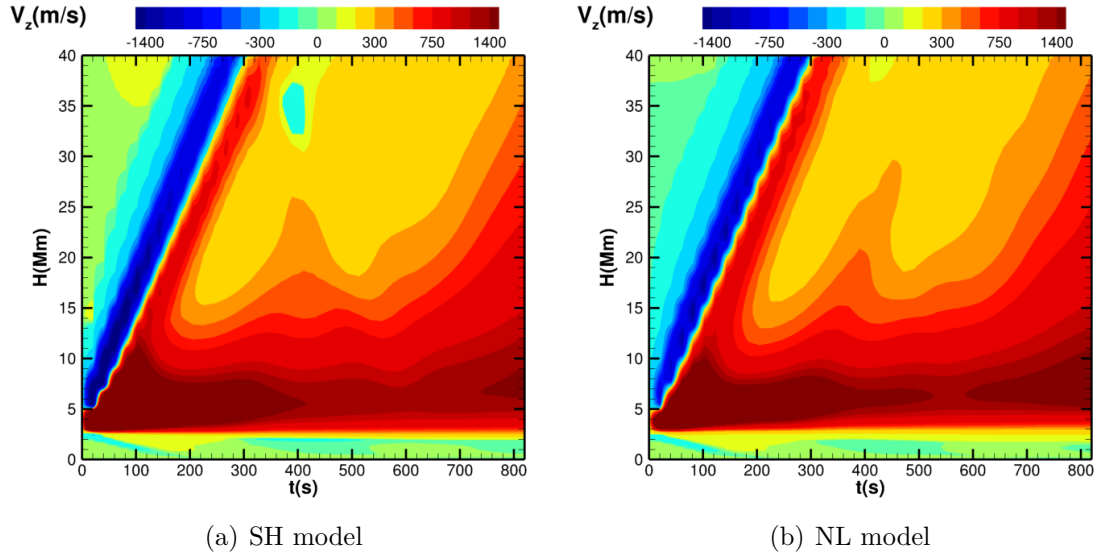
Source: Produced by the author.

component of velocity as a function of height, abscissa axis, and in function of time, coordinate axis. The panels confirm the tendency shown in Fig. 5.4 of a similar behavior for the models. In the corona, the nonlocal predicts some slow downflows from the upper part of atmosphere,  $H > 15$  Mm, earlier then the SH model. Both models predicts an initial adjustment of the system consisting of upflows and downflows seen in the panels initially at the upper TR and base of the corona and then going up until they reach the top of simulation box. After  $t=300s$ , the panels shows again the tendency in the corona for the averaged vertical velocity to be consisted

of upflows. The only exception would be some small downflows predicted by SH formulation around  $t=350s$  for  $33Mm < H < 38Mm$ . Since the results displayed in Figs. 5.4 and 5.5, are actually describing the average behavior for vertical velocities, the fact that the corona is dominated by upflows only indicates that when adding up the upwards velocities and the donwflows together, the contribution of the later is greater and prevails in the average.

The averaged temperature profiles are in agreement with the predictions made by (KARPEN; DEVORE, 1987) for a flaring loop. In our work the main differences regarding the models were found in lower atmosphere with the nonlocal predicting a smoother transition region. As for the averaged vertical velocities, the results for the velocities in corona and TR are also in agreement with the results from (KARPEN; DEVORE, 1987). The SH model gives higher upwards/downwards flow velocities initially and with NL model gives higher upflows coming from slightly different regions as different parts of the atmosphere are being heated. Therefore, the model we developed for the nonlocal calculation as described in chapter 4 is a valid approach. In the next section we investigate further the differences found in the models.

Figure 5.5 - The averaged vertical velocity in meters per second as a function of time in seconds (horizontal axis) and height (vertical axis).



Source: Produced by the author.

## 5.2 Energy transport and energy source contributions to the temperature

The differences found in temperature profile can be better understood by analyzing how the choice of the heat flux formulation may affect the processes of energy transport and losses in the plasma. In order to do that, we rewrote energy equation in terms of the plasma temperature:

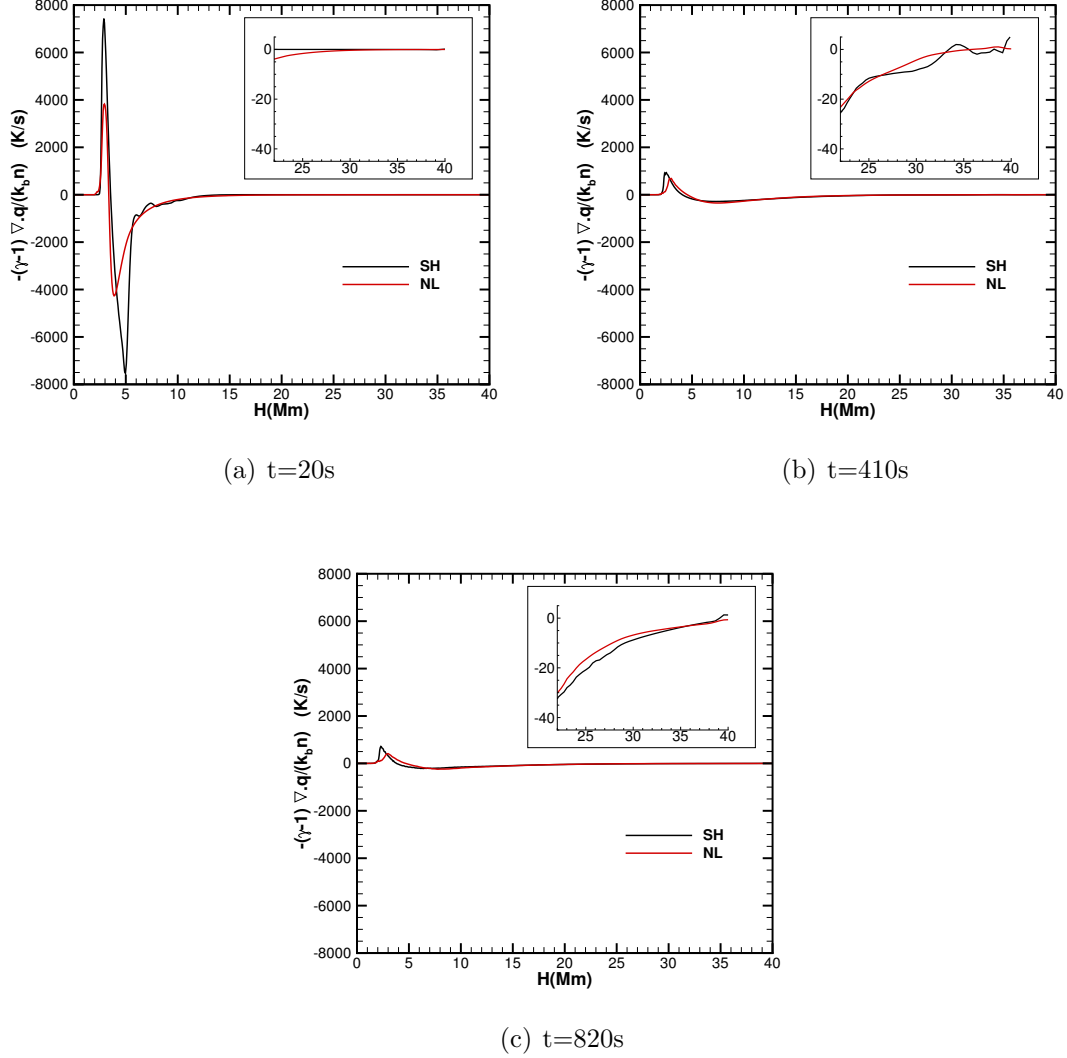
$$\frac{\partial T}{\partial t} - \nabla \cdot (T\mathbf{u}) = -(\gamma - 1)T\nabla \cdot \mathbf{u} + \frac{(\gamma - 1)}{k_b n}(\eta j^2 - \nabla \cdot \mathbf{q} + R). \quad (5.1)$$

As we did before, we compute the average vertical values for all the terms on the right side of Eq.( 5.1) along x-y plane.

The curves for energy transport by heat flux ( $\nabla \cdot \mathbf{q}$ ) and convection ( $\nabla \cdot \mathbf{u}$ ) are shown in Figs. 5.6 and 5.7, respectively, for the instants of time  $t=20s$ ,  $410s$  and  $820s$ . The high values for the curves in Fig. 5.6 compared to the values in Fig. 5.7 indicates that heat flux dominates the temperature evolution in both models. As the heat flux transports energy to the middle/low TR ( $3Mm \leq H \leq 4Mm$ ), part of that energy is used to heat the plasma which leads to plasma expansion and consequently local energy loss by the  $(\gamma - 1)\nabla T \cdot \mathbf{v}$  term. As for the coronal plasma in the upper part of the simulation box,  $H \geq 5Mm$ , the heat flux is transporting the energy outward and the plasma gets colder and compresses. The main differences of energy transport between the models appear in the lower solar corona, transition region and chromosphere as indicated by Fig. 5.6 and 5.7. The curves show again a similar behavior for the models in all instants of time.

Figure. 5.6(a) shows a considerable contribution from heat flux to the temperature. It comes from the corona/upper TR and goes to lower regions. The contribution gets smaller over time as displayed in Fig. 5.6(b) and 5.6(c). As the average contribution from the heat flux decreases, it starts to come from higher parts of the corona and to reach lower regions over time. Initially, the heat flux in SH model supplies twice the energy input for temperature increase in lower TR than NL model, as it is indicated by the peak around  $3.0 Mm$  in Fig. 5.6(a). In the following times, the difference between the models for the quantity of energy being transported to this area diminishes whereas the peaks are getting broader and displaced with respect to one model to another almost  $500 km$  as it can be seen in Fig. 5.6(c). As for the corona,  $5Mm \leq H \leq 40Mm$ , the average heat flux indicates that a small quantity of energy is being transported outwards and that quantity increases over time as

Figure 5.6 - Averages contributions from heat flux to temperature evolution,  $-(\gamma - 1)\nabla \cdot \mathbf{q}/(k_b n)$ , as a function of height for SH (black lines) and NL (red lines).



Source: Produced by the author.

indicated by the small plots on the right corner of the plots in Fig. 5.6. For the middle of the corona in our domain,  $7\text{Mm} \leq H \leq 18\text{Mm}$ , the lower temperature gradients together with great mean free paths lead NL model to predict higher values for temperature loss due to heat flux transport with values reaching 30% higher than the ones in SH formulation. That is due to delocalization of the heat flux that widens up the region from where the energy is coming from, reaching not only the lower corona, but having contributions also from higher regions. In the upper part of the simulation box, the temperature gradients get larger over time and therefore the contributions from SH model are greater.

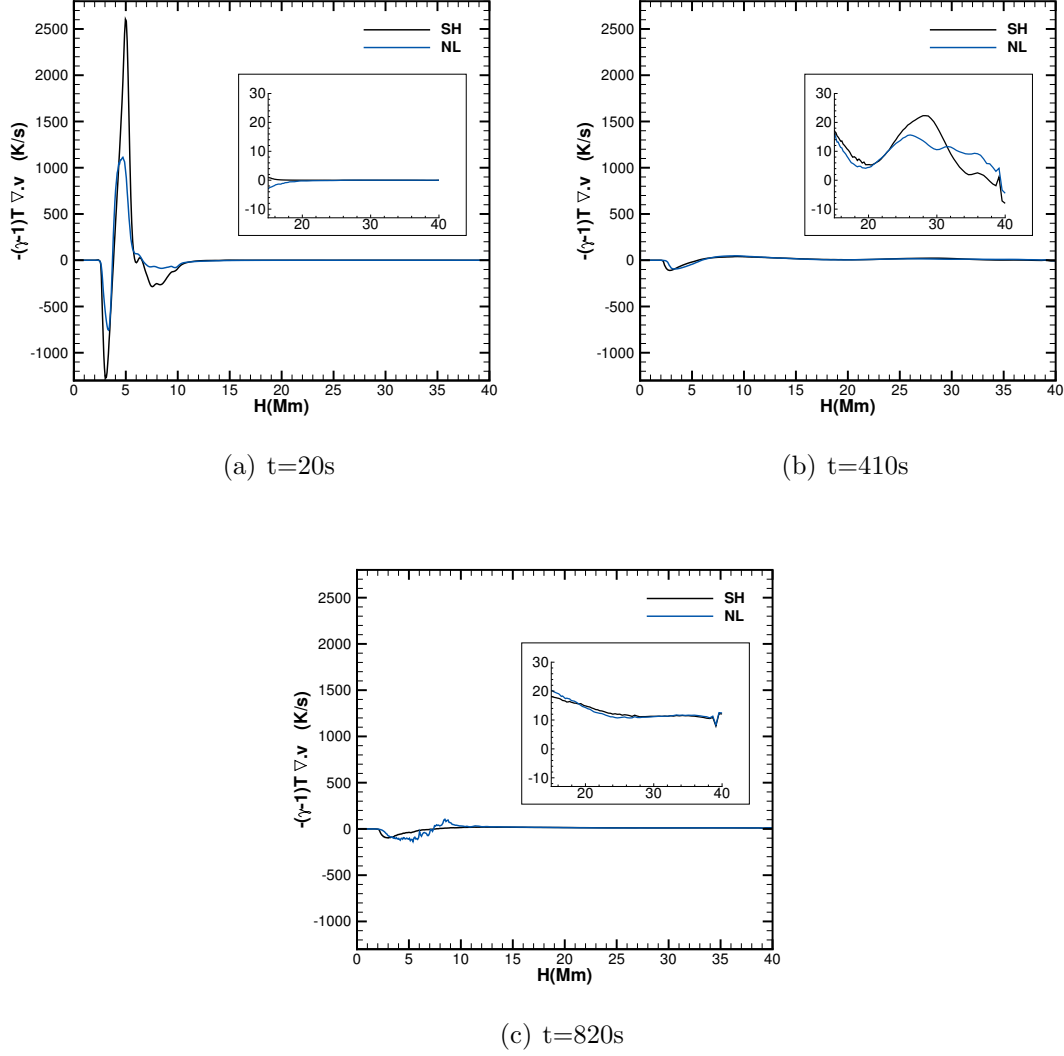
Figure 5.7 displays the average temperature gain/loss by plasma contraction/expansion. We see that initially, Fig. 5.7(a), there is an expansion of the plasma in upper chromosphere and lower transition region. In the upper part of TR and in the base of the corona, the plasma is getting colder because of energy transport from there by heat flux. As the plasma gets colder, the pressure in that region decreases and the external pressure compresses that plasma. The compression of plasma contributes to temperature gain. The compression in the base of the corona leads to a plasma expansion that makes the corona in the height range of  $7\text{Mm} \leq H \leq 11\text{Mm}$  to lose energy. The curves in later times, Figs. 5.7(b) and Fig. 5.7(c), indicate smaller plasma expansion and compression.

Just like as for the contributions from heat flux, the peaks for each model are displaced relative to each other going from an initial difference of 300 km to 400 km by the end of simulation. Initially, SH model predicts a plasma compression in chromosphere, around 2.3Mm, that gives temperature gain values that are a 100% higher than the gains by compression of plasma in NL model as indicated in Fig. 5.7(a). For TR and coronal plasma,  $3\text{Mm} \leq H \leq 5\text{Mm}$ , the models predict quite different values for temperature loss/gain by convection with the NL model obtaining values that are 10% to 79% smaller than SH values. Figures 5.7(b) and 5.7(c) shows a tendency for NL model to predict higher values for plasma compression/expansion in the base and lower corona ( $5\text{Mm} < H < 20\text{Mm}$ ).

The contribution coming from radiative cooling and ohmic heating terms are displayed in Figs. 5.8 and 5.9 respectively. The curves in Figs. 5.8 show the average temperature decreasing due thermal emissions for the region  $H \leq 10\text{Mm}$ . Again, we see a similar behavior for both models. There are basically no differences except for the curves displayed in Fig. 5.8(b) where we can see that SH model predicts a higher temperature loss. There are no differences in the temperature decrease due radiation when comparing the prediction by both heat flux models in the upper part of the simulation box,  $H \geq 10\text{Mm}$ .

The average contribution of current dissipation to plasma heating as a function of height is displayed in Fig. 5.9. We see that the higher values for current dissipation contributions are found in the region comprising the upper chromosphere, TR and lower corona:  $H \leq 10\text{Mm}$ . The current dissipation starts stronger for SH, as shown in Fig. 5.9(a). That tendency persists over time as it can be seen in Figs. 5.9(b) and 5.9(c), but the differences between the models get smaller. Towards the end, the nonlocal model predicts a broader region for contributions coming from current

Figure 5.7 - Averages contributions from plasma compression/expansion to temperature evolution,  $-(\gamma - 1)\nabla T \cdot \mathbf{u}$ , as a function of height for SH (black lines) and NL (blue lines).



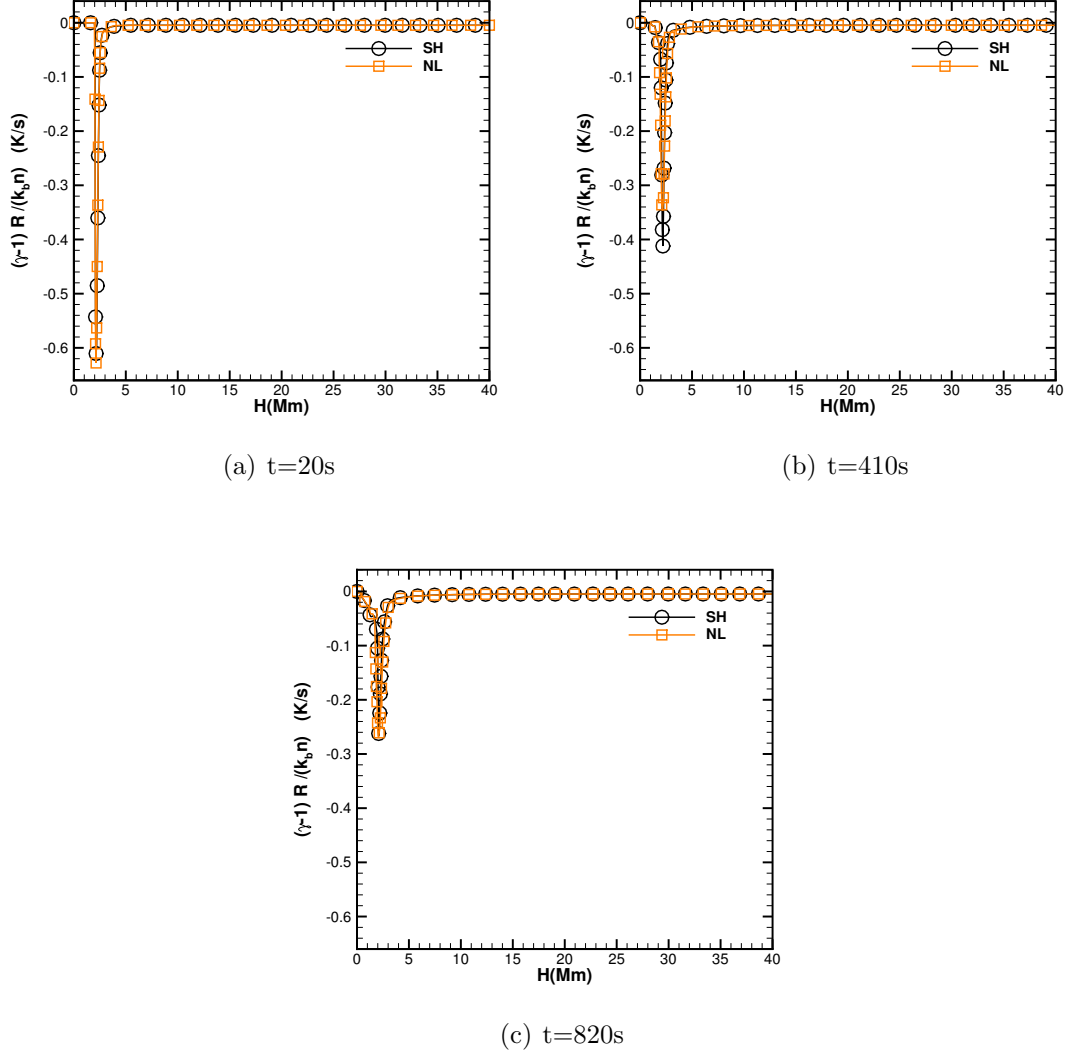
Source: Produced by the author.

dissipation, which gives a higher temperature rise due to dissipation in the corona for the height range  $5\text{Mm} \leq H \leq 10\text{Mm}$ . As for the rest of the corona, the SH formulation predicts 5% – 10% higher dissipation.

As the energy is being transported by heat flux in different quantities and to different loci depending on the heat flux formulation, the plasma responds differently to the energy input/output in each model. We can see that reflecting on the average temperature gain/loss by compression/expansion of plasma, current dissipation and



Figure 5.8 - Averages contributions from radiative losses to temperature evolution,  $-(\gamma - 1)R/(k_b\rho)$ , as a function of height for SH (black lines) and NL (orange lines).

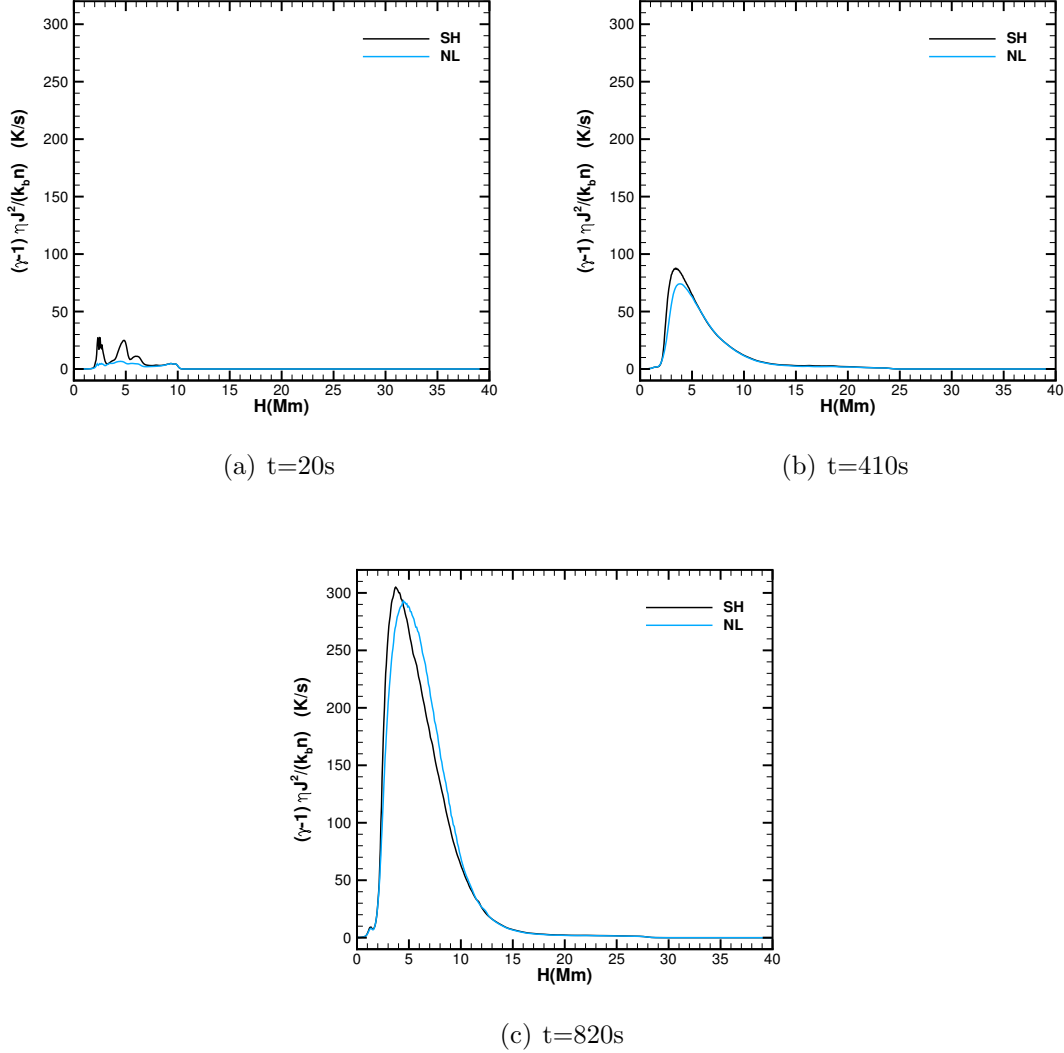


Source: Produced by the author

thermal emission. For example, we can see that part of the energy brought by heat flux to the region around 4.5Mm in Fig. 5.7(a) leads plasma expansion and therefore the energy is transported outwards and there is negative contribution to the temperature. In the NL model, since the energy input by heat flux is smaller, the plasma expansion is lower and thus less energy is loss due to that expansion as it can be seen in Fig. 5.8(a). Those compressions and expansions of the plasma together with the differences found in the heat flux affect the temperature evolution.

For the Chromosphere, we have seen that NL heat flux manage to transport more

Figure 5.9 - Averages contributions from current dissipation to temperature evolution,  $-(\gamma-1)\eta J^2/(k_b\rho)$ , as a function of height for SH (black lines) and NL (orange lines).



Source: Produced by the author.

energy to the lower part of the simulation box and also less energy is lost by plasma expansion there, which leads to temperatures 16% higher for the chromosphere in the nonlocal formulation around  $1.5 \text{ Mm} < H < 2.0 \text{ Mm}$ . The upper TR,  $2.0 \text{ Mm} < H < 3.0 \text{ Mm}$  presents considerable higher temperatures for SH due to the higher input of energy by heat flux when compared to NL model and also higher current dissipation for the same region.

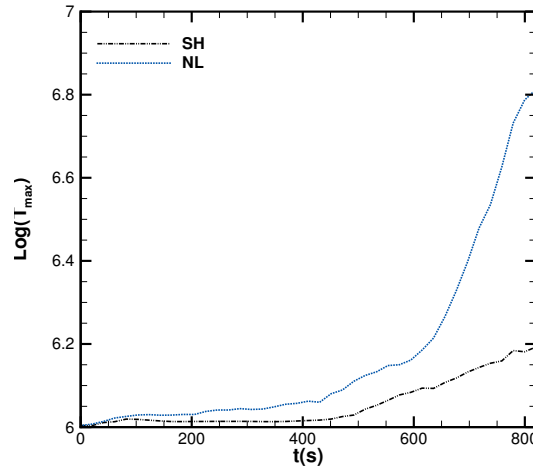
As a result from the differences found in the contribution coming from the terms in

energy loss function, the temporal evolution of temperature is affected as presented in Fig. 5.1. The broader and not so high peaks in the curves of Fig 5.6(a) together with the shift in peak loci for the NL model (compared to classical formulation), Figs. 5.6(b) and 5.6(c), mean that the energy is being distributed more evenly which leads to a smoother TR. In the coronal plasma, the NL scenario gain more energy by compression of the plasma and loses less energy by heat flux and therefore the SH provides slightly lower averaged temperatures within that height range.

### 5.3 Heating dynamics along magnetic field line

The dynamic set by the vortex led to currents that dissipate creating sources of heating for the plasma. We have investigated the response along a field line to the heating dynamics set by all the terms on the right side of Eq. (5.1) together. In order to select the field line, we have first computed the maximum temperature in the domain as a function of time which is displayed in Figure 5.10. The curve in light blue describes the behavior for temperature growth as predicted by NL and the black curve by SH formulation. We can see that the NL model presents almost

Figure 5.10 - Evolution of the maximum temperature found in corona as a function of time.



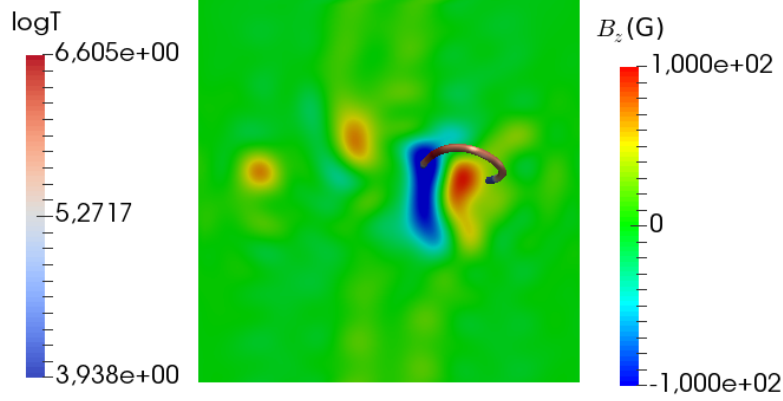
Source: Produced by the author.

from the beginning the highest temperatures and also presents a considerable faster growing for the temperature at times greater then 400 seconds.

Among the regions where the temperature presented considerable growth, we have selected one region that had the greatest difference in temperature for the two models

to trace a magnetic field line which is shown in Fig. 5.11.

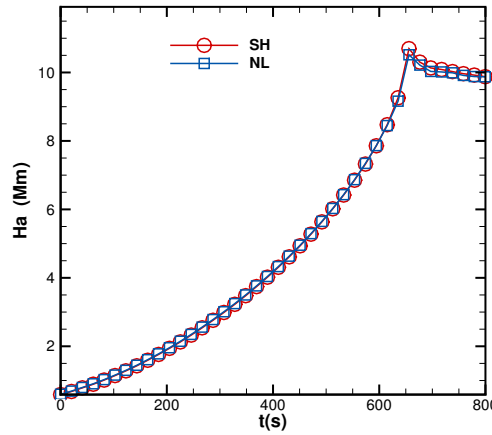
Figure 5.11 - View for x-y plane of simulation box with the selected field line colored by the log of the temperature and the slice colored by the z-component of magnetic field.



Source: Produced by the author.

The slice is colored by the z-component of the magnetic field and the field line by the log of the temperature. We see that the line is located in the region where the magnetic field is stronger as one would expect to find the highest temperatures. The evolution of the height of the loop apex,  $H_a$ , as a function of time is displayed in Fig. 5.12. Therefore the loop apex started at chromospheric heights and evolved reaching the corona after  $t=500s$ . There is practically no difference between the models for the evolution of the height of the apex of the field line.

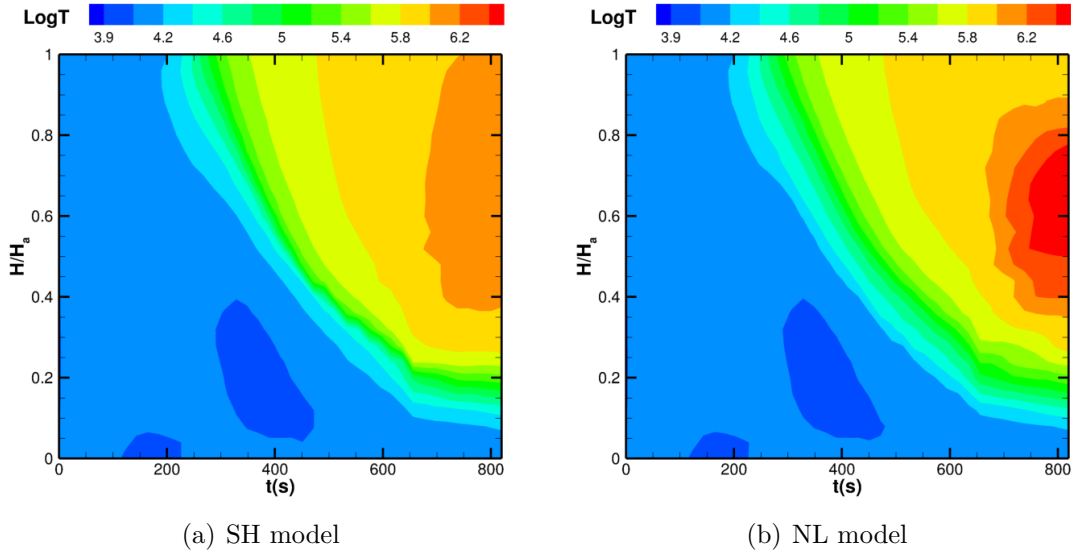
Figure 5.12 - Height of the loop apex,  $H_a$  as a function of time.



Source: Produced by the author.

Figure 5.13 illustrates the time evolution for the log of the temperature according to SH, Fig. 5.13(a), and to NL formulation, Fig. 5.13(b). The y-axis depicts the normalized height where we used the height of the loop apex as a normalization parameter. The loop starts in the chromosphere and is heated as it moves upward in the solar atmosphere. We see again the tendency of smoother and broader TR for NL model. The temperature increases in the corona starts around the same time,  $t \geq 600s$ , but it grows to considerable higher values in NL case. The classical heat flux formulation predicts a smoother temperature distribution along the coronal part of the loop whereas the NL gives a higher temperature in the middle of the coronal part of the loop.

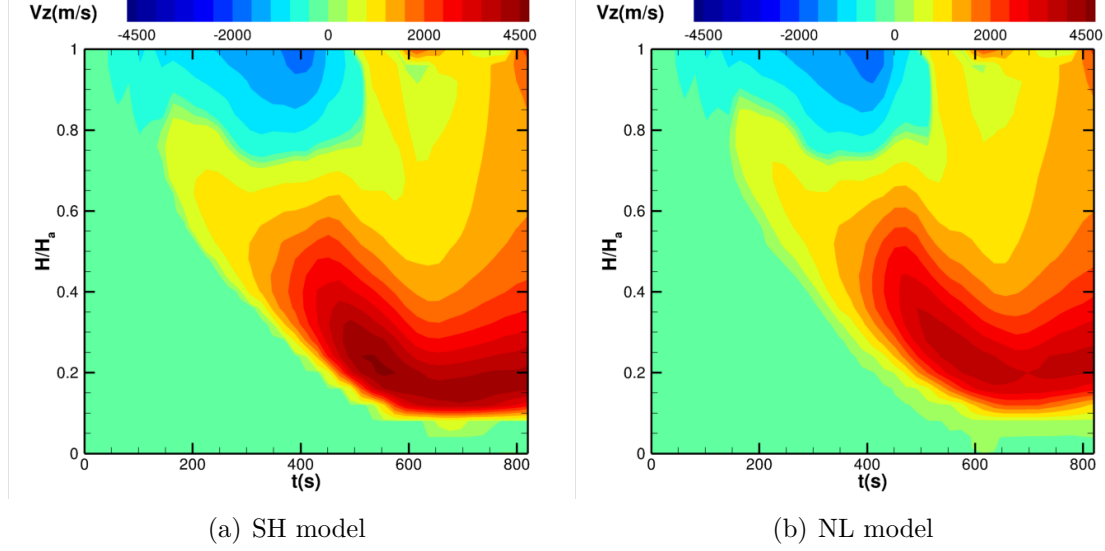
Figure 5.13 - The log of temperature as a function of time in seconds (horizontal axis) and the height of the loop normalized by the maximum height at time  $t$  (vertical axis).



Source: Produced by the author.

As the field line is heated and rises up, pressure gradients followed and they lead to upwards and downwards flows whose values are displayed in Fig. 5.14 as a function of loop height and time. The classical model is displayed in Fig. 5.14(a) and the results for nonlocal heat flux in Fig. 5.14(b). The vertical velocity along the loop presents a general similar behavior along the field line with few differences. As the SH model predicts higher heating at the base of coronal loops, the plasma there receives more energy and thus have greater upflow velocities. The nonlocal case predicts an earlier chromospheric evaporation and also upflows from the base of chromosphere around  $t=600s$ . As for the classical heat flux, the evaporation velocity is considerable higher

Figure 5.14 - The upwards and downwards flows along the field line in meters per second as a function of time in seconds (vertical axis) and the height of the loop normalized by the maximum height at time  $t$  (horizontal axis).



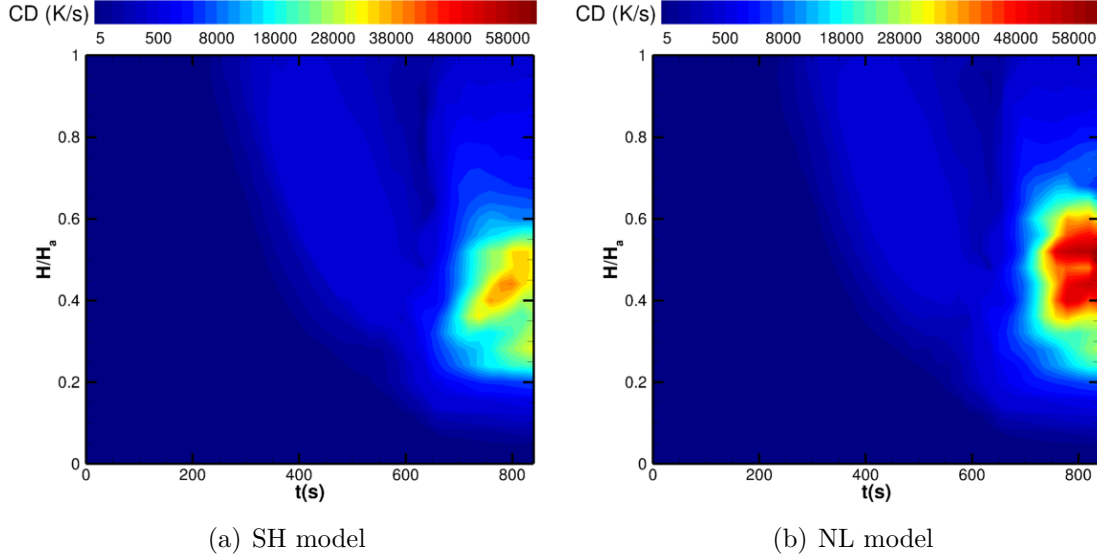
Source: Produced by the author.

and coming from a thinner region compared to the nonlocal transport.

The panels shown in Fig. 5.15 are colored by the contribution coming from the current dissipation,  $CD = -(\gamma - 1)\nabla\eta j^2/(k_b n)$ , to heat the plasma along the field line. The currents created by the footpoint motions start to have significant contribution for  $t > 400$ s. As the line goes up, the current dissipation begin to be more significant in the lower parts of the loop. After  $t = 600$ s, the temperature rise due to current dissipation is stronger in the part the loop within the TR and corona having higher values in the middle of the loop, which is at coronal heights,  $0.4 < H/H_a < 0.6$ . We see that while the values predicted by classical heat flux are slightly higher in the upper TR and base of the corona, the NL model, Fig. 5.15(b), gives values twice higher for contributions from current dissipation in the middle of the loop.

Figure 5.16 displays two panels colored by the contribution from heat flux to temperature,  $HF = -(\gamma - 1)\nabla \cdot \mathbf{q}/(k_b n)$ , along the line. The first panel, Fig. 5.16(a), is colored by SH model results and the second, Fig. 5.16(b), by values predicted by nonlocal formulation. We see basically no differences between the models for instants of time in  $t < 400$ s when the line has no significant energy input coming from currents dissipation. In the following times, as the temperature is rising due to the current dissipation, the heat flux starts to present quite different values in the TR and coronal part of the loop. As in the averaged results in Fig. 5.16??, the NL model predicts

Figure 5.15 - Contribution from current dissipation to temperature evolution as a function of time in seconds (vertical axis) and the height of the loop normalized by the maximum height at time  $t$  (horizontal axis).



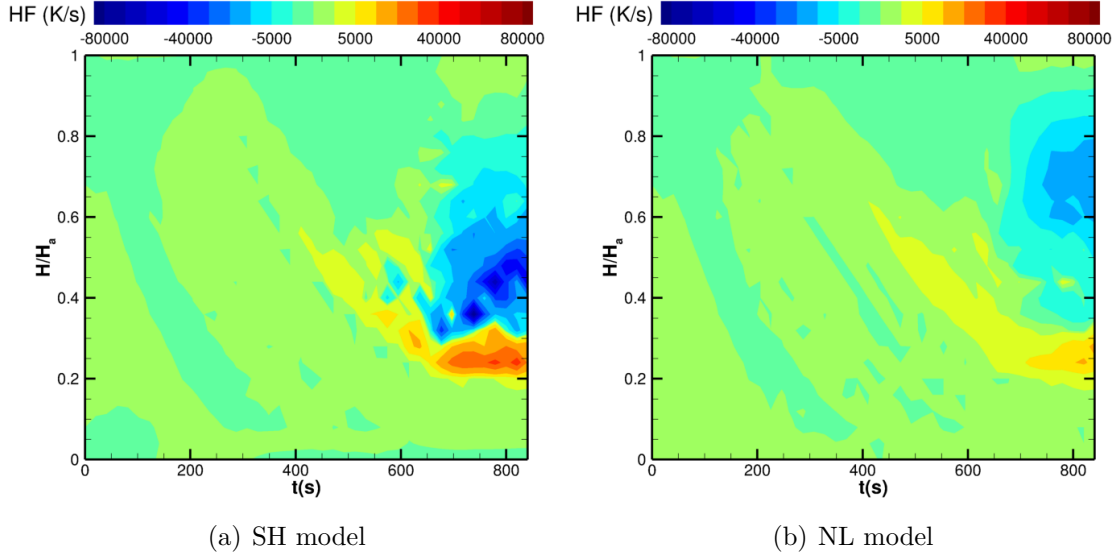
Source: Produced by the author.

lower values and wider regions for input/output of energy despite the energy input coming from the dissipation of the currents was greater for the nonlocal case. That is an effect coming from the delocalization kernel that bottle up the energy despite the existing temperature gradients. We see from Fig. 5.16(a) that the classical heat flux manage to distribute the exceeding energy from  $0.4 < H/H_a < 0.6$  to lower regions.

The contribution from current dissipation in the middle of the loop,  $0.3 < H/H_a < 0.6$ , leads to a plasma expansion as it can be seen in the panels in Fig. 5.17. The panels are colored by the contribution of compression/expansion of plasma to the temperature,  $CE = -(\gamma - 1)\nabla T \cdot \mathbf{u}$ . As that region expands, it compresses the coronal plasma close to the top of the loop,  $0.6 < H/H_a < 0.9$ , and it heats up that region. Again we see the tendency observed during the average results of higher compressional heating and cooling by expansion in the corona for the nonlocal formulation.

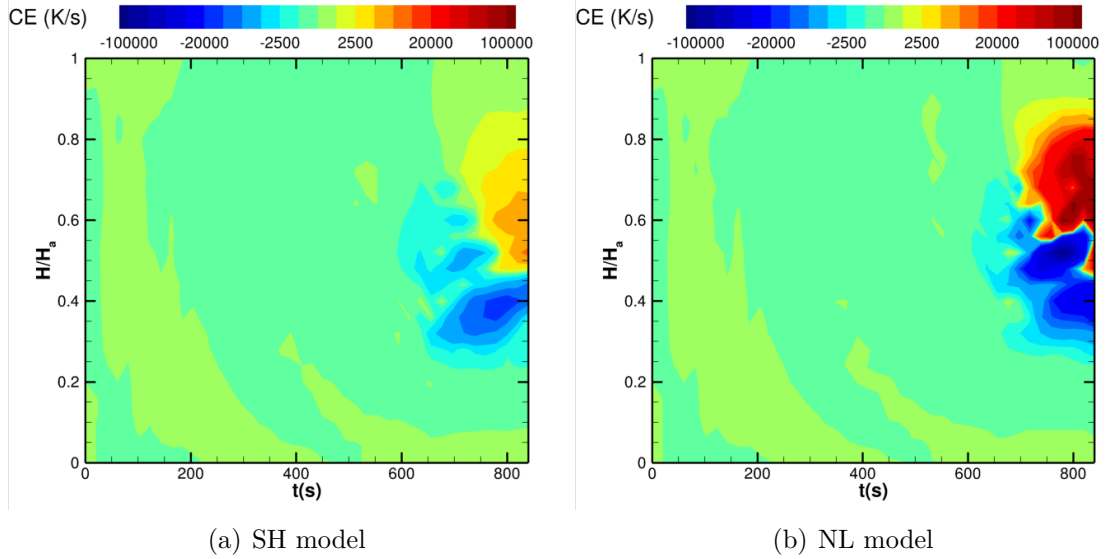
A comparison between the panels in Fig 5.15 and in Fig. 5.17 shows a quite different results for classical and nonlocal heat flux when it comes to the main heating mechanism in corona. While the SH model predicts that the contributions coming from current dissipation are the main source of plasma heating, the nonlocal heat flux

Figure 5.16 - Contribution from heat flux to temperature evolution as a function of time in seconds (vertical axis) and the height of the loop normalized by the maximum height at time  $t$  (horizontal axis).



Source: Produced by the author.

Figure 5.17 - Contribution from plasma compression/expansion to temperature evolution as a function of time in seconds (vertical axis) and the height of the loop normalized by the maximum height at time  $t$  (horizontal axis).



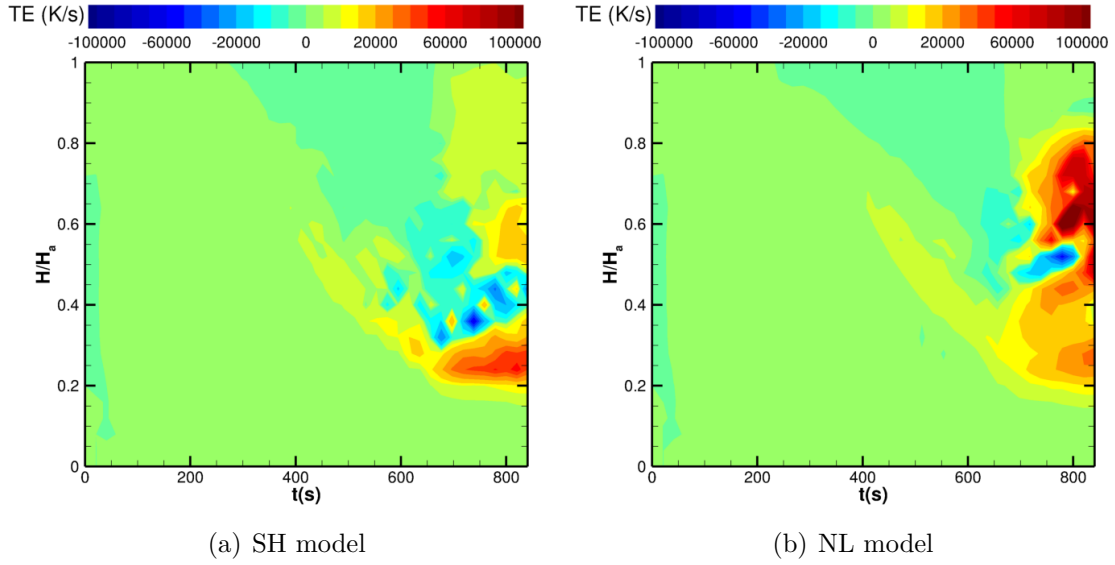
Source: Produced by the author.

predicts a different scenario where compressional heating is actually more efficient than the current dissipation for the coronal part of the loop.



We have computed the total contribution from transport and sources terms, TE, along the loop to the temperature evolution and the results are displayed in the panels in Fig. 5.18. The first panel in Fig. 5.18(a) shows the predictions for SH and the second panel, Fig. 5.18(b) , the results obtained using the nonlocal formulation.

Figure 5.18 - The total contribution from transport and sources terms to temperature evolution as a function of time in seconds (vertical axis) and the height of the loop normalized by the maximum height at time  $t$  (horizontal axis).



Source: Produced by the author.

We see that both models predicts quite different behaviors for temperature increase coming from transports and source/sinks of energy in plasma. The classical SH formulation expects stronger heating at coronal footpoints whereas the nonlocal model predicts heating spread across a far more widening range in the coronal part of the loop. Also, the temperature increase in NL case is greater then the one predicted by classical formulation. In the top of the loop,  $H/H_a > 0.85$ , the SH model gives higher temperature increments. Another interesting feature in nonlocal heat flux is that its corona is cooling considerable less than the classical formulation.



## 6 CONCLUSIONS AND FUTURE WORK

The results for average temperature and up/down velocities profiles were able to replicate the main features of the previous results obtained by [Karpen and DeVore \(1987\)](#) despite the fact that we have considered a broader initial transition region and that our simulations were performed assuming similar conditions of an active region and not a flare as in ([KARPEN; DEVORE, 1987](#)) . In our simulations, both models presented same general evolution with the main differences found around the TR and upper chromosphere. The nonlocal predicts an earlier heating of lower atmosphere compared to classical heat flux, which leads to smoothing of transition region. There was also an earlier upflow in chromosphere as a response to the preceding heating by nonlocal. The average vertical velocities also agree with the results presented in [Karpen and DeVore \(1987\)](#) for the post flare phase described there. The nonlocal has higher upflows velocities in the coronal region and with upflows prevailing in both models for corona. Finally, our simulation results also indicate that the nonlocal formulation predicts the highest temperature in corona. Our results differs from [Karpen and DeVore \(1987\)](#) regarding the location of the maximum temperature. While in their case the top of coronal loop had the highest temperatures, in our case the maximum temperature was found a little bit lower height along the loop. That is due to our different approach to describe the heating sources in plasma; they have considered a volumetric heating and we have modeled our heating source as coming from current dissipation with an anomalous plasma resistivity. Therefore, the agreements between our results and [Karpen and DeVore \(1987\)](#) show that our 3D model approximations are valid and could capture well the evolution of our model for a solar atmosphere.

The results hereby presented suggest that the nonlocal heat flux is more efficient to transport energy to the lower parts of the atmosphere. That is expected since the curves for the divergence of heat flux show broader peaks in NL model, indicating a better distribution of energy. The narrow peaks in the classical model favor higher temperature gradients and consequently more heat for the base of TR over time. Thus, there is a shift in TR height when comparing the heat flux formulations. The delocalization kernel also leads to less energy loss in corona as it could be seen in the results along the magnetic field line. The results along the field line suggest that a different heat flux not only changes the way heat is transported, but also influences the main heating mechanism in the coronal part of the loop. The classical heat flux predicts that the leading mechanism comes from current dissipation whereas the nonlocal presents the compressional heating as the main heating process in the

upper part of the loop.

Our numerical experiment indicates that there are differences for classical and non-local formulation for simulated plasma having parameters similar to the ones found in active regions. We cannot extrapolate our results to actual active regions due to some facts. First, our simulation box is actually small when compared to typical size area of active regions in the Sun, that limits the length of our loop. The transition region in our model was broader than predicted by standard solar atmosphere models. We also have not taken into account that the plasma is no longer fully ionized in lower atmosphere, therefore the results might be affected because part of the energy transported there might be lost to excitation and ionization process as it was emphasized by [Karpen and DeVore \(1987\)](#). For last, the nonlocal formulation used here was constructed for a plasma with features found in fusion plasmas presenting a high gradient temperature and long mean free paths ([BRANTOV; BYCHENKOV, 2013](#)). But still, our results suggest that an atmosphere consisting of a plasma with similar parameters found in corona and with high temperature gradients presents a temperature profile quite sensitive to the choice of heat flux. Furthermore, the heating of plasma presents a dependency on the heat flux formulation used. As the sources and transport terms are influenced by the choice of the heat flux, the importance of current dissipation as the main heating mechanism in corona is put into question as the NL model predicts the compressional heating having a major role as a heating process. Therefore, the heat flux role might not be limited to transport of energy, but it may also influence results regarding other process in the thermal evolution of the system.

It would be interesting to study if those different heat flux formulations would considerable impact the magnetic field evolution. The induction equation suggests that it might be the case since we have observed differences in the velocity divergence which rules the evolution of magnetic field strength. Such investigation demands longer simulation times because the field time scale is around one hour whereas our simulations would only describe the evolution of the system for thirteen minutes. Another necessary improvement to study the magnetic field evolution would be to have a proper description of the active region size. That can be achieved by implementing a stretched grid in x-y direction that is refined in the center of the simulation box where one find stronger magnetic field. Such modifications would also allow to investigate the importance of the heat flux formulation depending on the strength of magnetic flux of different active regions. In summary, there are still a lot of investigation to be pursued within the topic of the heat flux formulation

for weakly collisional plasma. And actually, the results of this thesis suggest that finding a correct description for heat flux might be crucial to understanding other aspects of the thermal evolution of the solar atmosphere.



## REFERENCES

- ABBETT, W. P.; HAWLEY, S. L. Dynamic models of optical emission in impulsive solar flares. **The Astrophysical Journal**, v. 521, p. 906–919, Aug 1999. [xv](#), [24](#)
- ADAMSON, E.; BÜCHNER, J.; OTTO, A. On the role of current dissipation in the energization of coronal bright points. **Astronomy & Astrophysics**, v. 557, n. 1-2, p. 109–110, 2013. [34](#)
- ASCHWANDEN, M. J. **Physics of the solar corona**. An introduction with problems and solutions (2. ed.). New York: Springer, 2005. 924 p. [7](#), [8](#), [9](#), [13](#), [20](#), [21](#), [42](#), [53](#)
- ASCHWANDEN, M. J.; WINEBARGER, A.; TSIKLARI, D.; PETER, H. The Coronal Heating Paradox. **The Astrophysical Journal**, v. 659, p. 1673–1681, apr. 2007. [14](#)
- BINGERT, S.; PETER, H. Intermittent heating in the solar corona employing a 3d mhd model. **A & A**, v. 530, p. A112, 2011. Available from: <http://dx.doi.org/10.1051/0004-6361/201016019>. [22](#)
- BITTENCOURT, J. A. **Fundamentals of plasma physics**. [S.l.]: Springer Verlag, 2003. 700 p. [17](#), [21](#), [23](#)
- BOYD, T. J. M.; SANDERSON, J. J. **The physics of plasmas**. UK: Cambridge University Press, 2003. 532 p. [20](#)
- BRANTOV, A.; BYCHENKOV, V. Nonlocal transport in hot plasma. Part I. **Plasma Physics Reports**, Springer US, v. 39, n. 9, p. 698–744, 2013. ISSN 1063-780X. [24](#), [25](#), [76](#)
- BÜCHNER, J.; NIKUTOWSKI, B.; OTTO, A. Coronal heating by transition region reconnection. In: ESA, 2004, St. Andrews, Scotland, UK. **SOHO 15 Coronal Heating**. [S.l.]: Proceedings Paris: European Space Agency, 2004. p. 23. [34](#)
- \_\_\_\_\_. Plasma acceleration due to transition region reconnection. **Particle Acceleration in Astrophysical Plasmas: Geospace and Beyond**, American Geophysical Union, p. 161–170, 2005. [34](#)

CHARBONNEAU, P. Solar dynamo theory. **Annual Review of Astronomy and Astrophysics**, v. 52, n. 1, p. 251–290, 2014. Available from: <http://dx.doi.org/10.1146/annurev-astro-081913-040012>>. 3

CHORIN, A. J. A numerical method for solving incompressible viscous flow problems. **Journal of Computational Physics**, v. 2, n. 1, p. 12 – 26, 1967. ISSN 0021-9991. Available from: <http://www.sciencedirect.com/science/article/pii/002199916790037X>>. 39

CIARAVELLA, A.; PERES, G.; SERIO, S. Non-local heat transport in static solar coronal loops. **Solar Physics Journal**, v. 132, p. 279–291, apr. 1991. 15, 31

COOK, J. W.; CHENG, C. C.; JACOBS, V. L.; ANTIOCHOS, S. K. Effect of coronal elemental abundances on the radiative loss function. **The Astrophysical Journal**, v. 338, p. 1176–1183, Mar 1989. 8, 20, 53

EMMANOUILIDI, C. **Solar corona image from eclipse over Queensland, Australia**. 2012. Available from: <http://epod.usra.edu/blog/2013/03/title-solar-corona-image-of-the-november-2012-eclipse-over-queensland-australia.html>>. Access in: Sept. 2016. 6

FREEDMAN, R.; GELLER, R.; KAUFMANN, W. **Universe: stars and galaxies**. W. H. Freeman, 2013. ISBN 9781464135279. Available from: <https://books.google.com.br/books?id=NejVjwEACAAJ>>. 4

GARBER, S. **Observing the sun: solar physics**. NASA Goddard Space Flight Center: [s.n.], 2013. Available from: <http://history.nasa.gov/NP-119/ch4.htm>>. Access in: Jan. 2013. 7

GIZON, L.; BIRCH, A. C.; SPRUIT, H. C. Local helioseismology: Three-dimensional imaging of the solar interior. **Annual Review of Astronomy and Astrophysics**, v. 48, n. 1, p. 289–338, 2010. Available from: <http://dx.doi.org/10.1146/annurev-astro-082708-101722>>. 2

GOEDBLOED, H.; POEDTS, S. **Principles of magnetohydrodynamics** with applications to laboratory and astrophysical plasmas. United Kingdom: Cambridge University Press, 2004. 21

GOMBOSI, T. I.; POWELL, K. G.; ZEEUW, D. L. D.; CLAUER, C. R.; HANSEN, K. C.; MANCHESTER, W. B.; RIDLEY, A. J.; R., I. I.; SOKOLOV, I. V.; STOUT, Q. F.; TóTH, G. Solution-adaptive magnetohydrodynamics for



space plasmas: Sun-to-earth simulations. **Computing in Science & Engineering**, v. 6, n. 2, p. 14–35, 2004. Available from: <<http://scitation.aip.org/content/aip/journal/cise/6/2/10.1109/MCISE.2004.1267603>>. 1, 33

GRAY, D. R.; KILKENNY, J. D. The measurement of ion acoustic turbulence and reduced thermal conductivity caused by a large temperature gradient in a laser heated plasma. **Plasma Physics**, v. 22, n. 2, p. 81, 1980. Available from: <<http://stacks.iop.org/0032-1028/22/i=2/a=001>>. 24

GUDIENSEN, B. V.; NORDLUND. Bulk heating and slender magnetic loops in the solar corona. **The Astrophysical Journal**, v. 572, p. L113–L116, jun. 2002. 22

\_\_\_\_\_. An ab initio approach to the solar coronal heating problem. **The Astrophysical Journal**, v. 618, p. 1020–1030, jan. 2005. 22

HELANDER, P.; SIGMAR, D. J. **Collisional transport in magnetized plasmas**. USA: Cambridge University Press, 2002. 292 p. 21, 24

HINODE. **NASA missions- HINODE**. 2016. Available from: <[http://www.nasa.gov/mission\\_pages/hinode/images.html](http://www.nasa.gov/mission_pages/hinode/images.html)>. Access in: Sept. 2016. 5

JAVADI, S.; BÜCHNER, J.; OTTO, A.; SANTOS, J. C. About the relative importance of compressional heating and current dissipation for the formation of coronal x-ray bright points. **A & A**, v. 529, p. A114, 2011. Available from: <<http://dx.doi.org/10.1051/0004-6361/201015614>>. 34

JUDGE, P. G.; CARLSSON, M. On the solar chromosphere observed at the limb with hinode. **The Astrophysical Journal**, v. 719, n. 1, p. 469, 2010. Available from: <<http://stacks.iop.org/0004-637X/719/i=1/a=469>>. 5

KARPEN, J. T.; CHENG, C.-C.; DOSCHEK, G. A.; DEVORE, C. R. Nonlocal thermal transport in solar flares. II - Spectroscopic diagnostics. **The Astrophysical Journal**, v. 338, p. 1184–1192, mar. 1989. 15, 29, 30

KARPEN, J. T.; DEVORE, C. R. Nonlocal thermal transport in solar flares. **The Astrophysical Journal**, v. 320, p. 904–912, sep. 1987. 15, 29, 30, 31, 55, 60, 75, 76

KELVINSONG. **The solar interior**. Wikimedia: [s.n.], 2013. Available from: <[http://commons.wikimedia.org/wiki/File:The\\_solar\\_interior.svg](http://commons.wikimedia.org/wiki/File:The_solar_interior.svg)>. Access in: Mar. 2014. 2

LUCIANI, J. F.; MORA, P.; VIRMONT, J. Nonlocal heat transport due to steep temperature gradients. **Phys. Rev. Lett.**, American Physical Society, v. 51, p. 1664–1667, Oct 1983. Available from:

<<http://link.aps.org/doi/10.1103/PhysRevLett.51.1664>>. 25, 26

MACKAY, D. H.; YEATES, A. R. The sun's global photospheric and coronal magnetic fields: Observations and models. **Living Reviews in Solar Physics**, v. 9, n. 1, p. 6, 2012. Available from:

<<http://dx.doi.org/10.12942/lrsp-2012-6>>. 11, 12

MITALAS, R.; SILLS, K. R. On the photon diffusion time scale for the sun. **The Astrophysical Journal**, v. 401, p. 759, dec. 1992. 3

OTTO, A.; BÜCHNER, J.; NIKUTOWSKI, B. Force-free magnetic field extrapolation for mhd boundary conditions in simulations of the solar atmosphere. **Astronomy and Astrophysics**, v. 468, p. 313–321, jun 2007. 42, 45

PARNELL, C. E.; MOORTELE, I. D. A contemporary view of coronal heating. **Philosophical Transactions of the Royal Society of London A: Mathematical, Physical and Engineering Sciences**, The Royal Society, v. 370, n. 1970, p. 3217–3240, 2012. ISSN 1364-503X. Available from: <<http://rsta.royalsocietypublishing.org/content/370/1970/3217>>. 1

PETER, H.; GUDIENSEN, B. V.; NORDLUND. Coronal heating through braiding of magnetic field lines. **The Astrophysical Journal**, v. 617, p. L85–L88, dec. 2004. 22

\_\_\_\_\_. Forward Modeling of the Corona of the Sun and Solar-like Stars: From a Three-dimensional Magnetohydrodynamic Model to Synthetic Extreme-Ultraviolet Spectra. **The Astrophysical Journal**, v. 638, p. 1086–1100, feb. 2006. 22

PRIEST, E. **Magnetohydrodynamics of the Sun**. Cambridge: Cambridge University Press, 2014. ISBN 9781139020732. Available from: <<https://www.cambridge.org/core/books/magnetohydrodynamics-of-the-sun/D49C6A190F3291C176BBBB4F2E433553>>. 2, 4, 14, 22, 33, 41

PRIEST, E. R. **Solar Magneto-hydrodynamic**. Holland: D. Reidel Publishing company, 1992. 469 p. 5, 7

SANTOS, J. C.; BÜCHNER, J.; OTTO, A. Development of electric currents in a magnetic field configuration containing a magnetic null point. **Astronomy & Astrophysics**, EDP Sciences, v. 525, p. A3, 2011. 34

SANTOS, J. C.; BÜCHNER, J.; ZHANG, H. Inferring plasma flow velocities from photospheric vector magnetic field observations for the investigation of flare onsets. **Advances in Space Research**, Elsevier, v. 42, n. 5, p. 812–821, 2008. 34

SCHARMER, G.; LANGHANS, K. **Small regular spot**. 2003. Available from: <<http://www.isf.astro.su.se/gallery/images/2003/>>. Access in: Sept. 2016. 10

SCHRIJVER, C. J.; SISCOE, G. L.; BOGDAN, T. J.; REMPEL, M.; LONGCOPE, D. W.; FORBES, T. G.; MOLDWIN, M. B.; SMITH, C. W.; HANSTEEN, V. H.; VASYLIÁNAS, V. M.; TOFFOLETTO, F. R.; FULLER-ROWELL, T.; BAGENAL, F. **Heliophysics: Plasma Physics of the Local Cosmos**. Cambridge, UK: Cambridge University Press, 2011. Available from: <<http://www.cambridge.org/us/academic/subjects/earth-and-environmental-science/atmospheric-science-and-meteorology/heliophysics-plasma-physics-local-cosmos>>. 1, 14

SCHWENN, R. Space weather: The solar perspective. **Living Reviews in Solar Physics**, v. 3, n. 1, p. 2, 2006. ISSN 1614-4961. Available from: <<http://dx.doi.org/10.12942/lrsp-2006-2>>. 1

SDO. **New light shed on explosive solar activity**. 2012. Available from: <<http://www.sciencedaily.com/releases/2012/07/120702134748.htm>>. Access in: Nov. 2013. 11, 13, 42, 45

\_\_\_\_\_. **NASA's SDO shows images of significant solar flare**. NASA Goddard Space Flight Center: [s.n.], 2014. Available from: <[http://www.nasa.gov/content/goddard/nasas-sdo-shows-images-of-significant-solar-flare/#.U5DG9\\_ldX1Y](http://www.nasa.gov/content/goddard/nasas-sdo-shows-images-of-significant-solar-flare/#.U5DG9_ldX1Y)>. Access in: Mar. 2014. 14

SHIBATA, K.; MAGARA, T. Solar flares: Magnetohydrodynamic processes. **Living Reviews in Solar Physics**, v. 8, n. 6, 2011. Available from: <<http://www.livingreviews.org/lrsp-2011-6>>. 13

SKÁLA, J.; BARUFFA, F.; BÜCHNER, J.; RAMPP, M. The 3d mhd code goemhd3 for astrophysical plasmas with large reynolds numbers. **A& A**, v. 580,

p. A48, 2015. Available from:

<<http://dx.doi.org/10.1051/0004-6361/201425274>>. 34

SOHO. NASA missions- SOHO. 2016. Available from:

<[http://www.nasa.gov/mission\\_pages/SOHO/images.html](http://www.nasa.gov/mission_pages/SOHO/images.html)>. Access in: Sept. 2016. 6

SPITZER, L. **Physics of fully ionized gases**. [S.l.: s.n.], 1956. 21, 22

SPITZER, L.; HÄRM, R. Transport phenomena in a completely ionized gas.

**Phys. Rev.**, American Physical Society, v. 89, p. 977–981, Mar 1953. Available from: <<http://link.aps.org/doi/10.1103/PhysRev.89.977>>. 23

STEREO. **Welcome to STEREO learning center**. NASA Goddard Space Flight Center: [s.n.], 2012. Available from:

<<http://stereo.gsfc.nasa.gov/classroom/EUVsun.shtml>>. Access in: Nov. 2012. 10

TESTA, P.; PONTIEU, B. D.; ALLRED, J.; CARLSSON, M.; REALE, F.; DAW, A.; HANSTEEN, V.; MARTINEZ-SYKORA, J.; LIU, W.; DELUCA, E. E.; GOLUB, L.; MCKILLOP, S.; REEVES, K.; SAAR, S.; TIAN, H.; LEMEN, J.; TITLE, A.; BOERNER, P.; HURLBURT, N.; TARBELL, T. D.; WUELSE, J. P.; KLEINT, L.; KANKELBORG, C.; JAEGGLI, S. Evidence of nonthermal particles in coronal loops heated impulsively by nanoflares. **Science**, v. 346, n. 6207, 2014. ISSN 0036-8075. Available from:

<<http://science.sciencemag.org/content/346/6207/1255724>>. 14

VANCANNEYT, S.; et. al. **The classification of solar flares**. Belgium: [s.n.], 2014. Available from: <<http://www.spaceweatherlive.com/en/help/the-classification-of-solar-flares>>. Access in: Mar. 2014. 41

VERNAZZA, J. E.; AVRETT, E. H.; LOESER, R. Structure of the solar chromosphere. III - Models of the EUV brightness components of the quiet-sun. **The Astrophysical Journal**, v. 45, p. 635–725, apr. 1981. 5

WEINBERG, D. H. **Radiative cooling and heating**. Ohio State University: [s.n.], 2013. Available from:

<<http://www.astronomy.ohio-state.edu/~dhw/A825/notes8.pdf>>. Access in: Apr. 2013. 19, 21

WIDMER, F.; BÜCHNER, J.; YOKOI, N. Sub-grid-scale description of turbulent magnetic reconnection in magnetohydrodynamics. **Physics of Plasmas**, v. 23,

n. 4, 2016. Available from: <<http://scitation.aip.org/content/aip/journal/pop/23/4/10.1063/1.4947211>>. 34

WIEGELMANN, T.; THALMANN, J. K.; SOLANKI, S. K. The magnetic field in the solar atmosphere. **The Astronomy and Astrophysics Review**, v. 22, n. 1, p. 78, 2014. ISSN 1432-0754. Available from: <<http://dx.doi.org/10.1007/s00159-014-0078-7>>. 41, 42

YANG, S.; BÜCHNER, J.; SANTOS, J. C.; ZHANG, H. Evolution of relative magnetic helicity: method of computation and its application to a simulated solar corona above an active region. **Solar Physics**, Springer Netherlands, v. 283, n. 2, p. 369–382, 2013. 34

ZANNA, G. D.; DERE, K. P.; YOUNG, P. R.; LANDI, E.; MASON, H. E. Chianti - an atomic database for emission lines. version 8. **A & A**, v. 582, p. A56, 2015. Available from: <<http://dx.doi.org/10.1051/0004-6361/201526827>>. 53, 54



## **PUBLICAÇÕES TÉCNICO-CIENTÍFICAS EDITADAS PELO INPE**

### **Teses e Dissertações (TDI)**

Teses e Dissertações apresentadas nos Cursos de Pós-Graduação do INPE.

### **Manuais Técnicos (MAN)**

São publicações de caráter técnico que incluem normas, procedimentos, instruções e orientações.

### **Notas Técnico-Científicas (NTC)**

Incluem resultados preliminares de pesquisa, descrição de equipamentos, descrição e ou documentação de programas de computador, descrição de sistemas e experimentos, apresentação de testes, dados, atlas, e documentação de projetos de engenharia.

### **Relatórios de Pesquisa (RPQ)**

Reportam resultados ou progressos de pesquisas tanto de natureza técnica quanto científica, cujo nível seja compatível com o de uma publicação em periódico nacional ou internacional.

### **Propostas e Relatórios de Projetos (PRP)**

São propostas de projetos técnico-científicos e relatórios de acompanhamento de projetos, atividades e convênios.

### **Publicações Didáticas (PUD)**

Incluem apostilas, notas de aula e manuais didáticos.

### **Publicações Seriadas**

São os seriados técnico-científicos: boletins, periódicos, anuários e anais de eventos (simpósios e congressos). Constam destas publicações o Internacional Standard Serial Number (ISSN), que é um código único e definitivo para identificação de títulos de seriados.

### **Programas de Computador (PDC)**

São a seqüência de instruções ou códigos, expressos em uma linguagem de programação compilada ou interpretada, a ser executada por um computador para alcançar um determinado objetivo. Aceitam-se tanto programas fonte quanto os executáveis.

### **Pré-publicações (PRE)**

Todos os artigos publicados em periódicos, anais e como capítulos de livros.